

# Resonant two-photon ionization studies of non covalent interactions in halo aromatic clusters and spin-orbit coupling modeling in mono-halocarbenes

Silver Nyambo  
*Marquette University*

---

## Recommended Citation

Nyambo, Silver, "Resonant two-photon ionization studies of non covalent interactions in halo aromatic clusters and spin-orbit coupling modeling in mono-halocarbenes" (2014). *Dissertations (2009 -)*. Paper 427.  
[http://epublications.marquette.edu/dissertations\\_mu/427](http://epublications.marquette.edu/dissertations_mu/427)

RESONANT TWO-PHOTON IONIZATION STUDIES OF NON COVALENT  
INTERACTIONS IN HALO AROMATIC CLUSTERS AND SPIN-ORBIT COUPLING  
MODELING IN MONO-HALOCARBENES

by

SILVER NYAMBO, BSc Applied Physics

A dissertation submitted to the Faculty of the Graduate School,  
Marquette University,  
in partial fulfillment of the requirements for  
the Degree of Doctor of Philosophy

Milwaukee, Wisconsin, USA

December 2014

## ABSTRACT

### RESONANT TWO-PHOTON IONIZATION STUDIES OF NON COVALENT INTERACTIONS IN HALO AROMATIC CLUSTERS AND SPIN-ORBIT COUPLING MODELING IN MONO-HALOCARBENES

Silver Nyambo, BSc Applied Physics

Marquette University, 2014

Non-covalent interactions in halobenzenes (PhX) (X=F, Cl, Br) and phenylamine (C<sub>6</sub>H<sub>5</sub>NH<sub>2</sub>) have been studied here using resonance two-photon ionization (R2PI) spectroscopy combined with a linear TOF-mass spectrometer. Their interaction with polar molecules in form of ammonia (NH<sub>3</sub>) and trifluorohalomethanes (CF<sub>3</sub>X) has also been studied. DFT and TD-DFT calculations using M06-2X functionals were carried out on different cluster conformations to compliment experimental results. A general trend of broadness in homogenous dimers (PhX)<sub>2</sub>, has been attributed to mainly the presence of multiple cluster isomers and Frank-Condon activity in the low frequency intermolecular vibrational modes. The van der Waals interactions between PhX and ammonia were all assigned to an in-plane  $\sigma$ -type geometry as compared to an out of plane  $\pi$ -type conformation. Stable halogen bonded dimer structures in the C<sub>6</sub>H<sub>5</sub>NH<sub>2</sub>⋯CF<sub>3</sub>X system were also optimized. In the second part of this dissertation, a global analysis of spin-orbit coupling in the mono-halocarbenes, CH(D)X, where X = Cl, Br, I is presented. Mono-halocarbenes are model systems for examining carbene singlet-triplet energy gaps and spin-orbit coupling. Experiments probing the ground vibrational levels in these carbenes have clearly demonstrated the presence of perturbations involving a low-lying triplet. To model these interactions more globally, a diabatic treatment of the spin-orbit coupling is adopted, where matrix elements are written in terms of a purely electronic spin-orbit matrix element which is independent of nuclear coordinates, and an integral representing the overlap of the singlet and triplet vibrational wavefunctions. In this way, the structures, harmonic frequencies, and normal mode displacements from *ab initio* and DFT calculations were used to calculate the vibrational overlaps of the singlet and triplet state levels, incorporating the full effects of Duschinsky mixing. These results were then incorporated with the electronic spin-orbit matrix element into a matrix diagonalization routine that calculated the term energies of the mixed singlet-triplet levels, which were iteratively fit to the extensive experimental results from SVL emission and SEP spectroscopy for the halocarbenes. These calculations have allowed many new assignments to be made, particularly for CHI, and provided spin-orbit coupling matrix elements and improved values for the singlet-triplet gaps.

## ACKNOWLEDGEMENTS

No one walks the journey of life alone and be successful, hence, this is where I get to thank all those who helped me along the way. I would like to thank my supervisor Dr. Scott Reid for the valuable guidance, advice and tremendous financial support throughout my time at Marquette University. I also want to express my deepest gratitude to my committee members, Dr. Mark Steinmetz and Dr. Qadir Timerghazin for their guidance and support. I also wish to express my love and gratitude to my wife, Tracy Liboma, and all my family members for walking by my side throughout this long journey.

## TABLE OF CONTENTS

CHAPTER 1: RESONANT TWO-PHOTON IONIZATION STUDIES OF NON COVALENT INTERACTIONS.....	1
1.1 INTRODUCTION TO NON-COVALENT INTERACTIONS.....	1
1.1.1 HALOGEN BONDING .....	2
1.1.2 II-II INTERACTIONS .....	3
1.1.3 CH/ $\pi$ INTERACTIONS .....	5
1.1.3 TYPE OF TRANSITIONS IN HALOBENZENES.....	6
1.1.4 SPECTRAL SHIFTS IN HALOBENZENES .....	7
1.2 EXPERIMENTAL METHODS.....	8
1.2.1 THE PRINCIPLE OF R2PI-TOF TECHNIQUE .....	8
1.2.2 TIME OF FLIGHT MASS SEPARATION .....	9
1.2.3 FORMATION OF MOLECULAR CLUSTERS- SUPERSONIC JET METHOD .....	11
1.3 COMPUTATIONAL METHODS .....	13
1.3.1 DENSITY FUNCTIONAL THEORY (DFT) METHODS.....	13
1.3.2 TIME-DEPENDENT DENSITY FUNCTIONAL THEORY (TD-DFT) METHODS.....	14
1.3.3 COUNTERPOISE CORRECTION AND BASIS SET SUPERPOSITION ERROR (BSSE).....	15
CHAPTER 2: BROMOBENZENE CLUSTERS .....	17
2.1 INTRODUCTION TO BROMOBENZENE CLUSTERS .....	17
2.2 PHOTO-DISSOCIATION OF BROMOBENZENE .....	20
2.3 EXPERIMENTAL SETUP.....	22
2.4 COMPUTATIONAL DETAILS FOR BROMOBENZENE CLUSTERS .....	26
2.5 BROMOBENZENE DIMER CONFORMATIONS.....	27
2.6 R2PI SPECTRA OF BROMOBENZENE DIMER .....	29
2.7 TD-DFT CALCULATIONS.....	36
2.8 MIXED DIMERS: R2PI SPECTRA OF BROMOBENZENE-BENZENE DIMER .....	40
2.9 BROMOBENZENE TRIMER CONFORMATIONS .....	43
2.10 VALIDATION OF TDDFT CALCULATIONS .....	49
2.10.1 CHLOROBENZENE – AMMONIA VAN DER WAALS DIMER.....	49

SUMMARY .....	52
CHAPTER 3. PhBr-NH <sub>3</sub> VAN DER WAALS DIMER .....	55
3.1 INTRODUCTION TO PhX-NH <sub>3</sub> VAN DER WAALS COMPLEXES .....	55
3.2 EXPERIMENTAL AND COMPUTATIONAL DETAILS .....	59
3.3 RESULTS AND ANALYSIS .....	60
3.3.1 GEOMETRY OPTIMIZATIONS .....	60
3.3.2 R2PI SPECTRA AND REACTION PATHWAYS .....	62
3.4 TDDFT CALCULATIONS .....	70
3.4.1 MULTIDIMENSIONAL FRANK-CONDON FACTOR SIMULATION .....	72
SUMMARY ON PhBr-NH <sub>3</sub> DIMER .....	74
SUMMARIZATION ON THE PhX-NH <sub>3</sub> VAN DER WAALS DIMERS .....	75
CHAPTER 4. ANILINE-CF <sub>3</sub> X VAN DER WAALS COMPLEXES .....	78
4.1 INTRODUCTION TO ANILINE-CF <sub>3</sub> X VAN DER WAALS .....	78
4.2 EXPERIMENTAL AND COMPUTATIONAL DETAILS .....	79
4.3 RESULTS AND ANALYSIS .....	80
SUMMARY .....	89
CHAPTER 5. MODELING SPIN-ORBIT COUPLING IN MONOHALOCARBENES .....	90
5.1 INTRODUCTION TO MONOHALOCARBENES .....	90
5.2 ELECTRONIC STRUCTURE OF MONOHALOCARBENES .....	92
5.3 SPIN-ORBIT COUPLING .....	94
5.5 LITERATURE SURVEY .....	102
5.5.1 SINGLE VIBRONIC LEVEL EMISSION (SVL) SPECTROSCOPY .....	102
5.5.2 THE SINGLET-TRIPLET GAP IN MONO HALOCARBENES .....	103
5.6.1 THEORETICAL DETERMINATION OF $\Delta E_{ST}$ .....	103
5.6.2 EXPERIMENTAL DETERMINATION OF $\Delta E_{ST}$ .....	106
5.7 SPIN-ORBIT COUPLING (SOC) AND PERTURBATION OF STATES .....	109
5.7.1 SOC IN CHF AND CDF .....	109
5.7.2 SOC IN CHCl AND CDCl .....	110
5.7.3 SOC IN CHBr AND CDBr .....	111
5.7.4 SOC IN CHI AND CDI .....	112
5.8 POTENTIAL ENERGY SURFACES .....	112
5.9 METHODOLOGY .....	113
5.9.1 COMPUTATIONAL METHODS .....	113
5.9.2 EQUILIBRIUM GEOMETRIES .....	115

5.9.3 VIBRATIONAL OVERLAPS .....	117
5.9.4 FRANK CONDON FACTORS (FCF).....	118
5.9.5 MATRIX ELEMENTS: THE APPROXIMATION.....	122
5.9.6 DUSCHISNKY EFFECT .....	125
5.9.7 ANHARMONIC OSCILLATOR MODEL FIT.....	128
5.9.8 SETTING UP THE HAMILTONIAN MATRIX .....	129
CHAPTER 6. CHI AND CDI.....	130
6.1 CHI SVL EMISSION SPECTRUM .....	130
6.2 CHI VIBRATIONAL ENERGY LEVEL ASSIGNMENTS.....	130
6.3 FIT PARAMETERS .....	131
6.4 ENERGY LEVEL DIAGRAM.....	134
6.5 CDI VIBRATIONAL ENERGY LEVEL ASSIGNMENTS.....	135
6.6 FIT PARAMETERS .....	138
6.7 ENERGY LEVEL DIAGRAM FOR CDI .....	139
CHAPTER 7. CHBr AND CDBr.....	141
7.1 CHBR VIBRATIONAL LEVEL ASSIGNMENTS.....	141
7.2 FIT PARAMETERS .....	142
7.3 ENERGY LEVEL DIAGRAM FOR CHBr.....	145
7.4 CDBr VIBRATIONAL ENERGY LEVEL ASSIGNMENTS.....	148
7.5 FIT PARAMETERS .....	150
7.6 ENERGY LEVEL DIAGRAM FOR CDBr.....	152
CHAPTER 8. CH <sup>35</sup> Cl AND CD <sup>35</sup> Cl.....	154
8.1 CH <sup>35</sup> Cl VIBRATIONAL ENERGY LEVEL ASSIGNMENTS.....	154
8.2 FIT PARAMETERS .....	157
8.3 ENERGY LEVEL DIAGRAM.....	158
8.4 CD <sup>35</sup> Cl SINGLE VIBRONIC LEVEL EMISSION.....	160
8.5 FIT PARAMETERS .....	163
8.6 RESULTS ANALYSIS.....	164
8.6.1 SINGLET-TRIPLET ENERGY GAPS.....	164
8.6.2 COMPARISON OF DERIVED SPIN-ORBIT COUPLING CONSTANTS.....	166
SUMMARY .....	168
REFERENCES .....	170

## LIST OF TABLES

<b>Table 1:</b> Summary of PhX-NH <sub>3</sub> van der Waals dimer complexes. The energies are in wavenumbers. ....	76
<b>Table 2:</b> Optimized CHX geometries at the B3LYP/aug-cc-pVTZ level. ....	116
<b>Table 3:</b> The optimized geometries of deuterated monohalocarbenes at the B3LYP/aug-cc-pVTZ level. ....	116
<b>Table 4:</b> Assignments of the calculated and mixed SVL emission spectra energy levels for CHI. Energies are in cm <sup>-1</sup> . ....	132
<b>Table 5:</b> Vibrational frequencies in cm <sup>-1</sup> . ....	133
<b>Table 6:</b> Shows the fit parameters obtained during the fitting of the energy levels to the experimental values. ....	133
<b>Table 7:</b> Vibrational level assignments for CDI. Energies are in cm <sup>-1</sup> . ....	137
<b>Table 8:</b> Vibrational frequencies in cm <sup>-1</sup> . ....	138
<b>Table 9:</b> Shows the fit parameters obtained during the fitting of the energy levels to the experimental values for CDI. ....	139
<b>Table 10:</b> Vibrational levels assignments for CHBr. Energies are in cm <sup>-1</sup> . ....	143
<b>Table 11:</b> CHBr vibrational frequencies in cm <sup>-1</sup> . ....	144
<b>Table 12:</b> Fit parameters for CHBr. ....	145
<b>Table 13:</b> Vibrational levels assignments for CDBr. Energies are in cm <sup>-1</sup> . ....	149
<b>Table 14:</b> CDBr vibrational frequencies, in cm <sup>-1</sup> . ....	151
<b>Table 15:</b> Shows the fit parameters obtained during the fitting of the energy levels to the experimental values for CDBr. ....	152
<b>Table 16:</b> Vibrational levels assignments for CH <sup>35</sup> Cl. Energies are in cm <sup>-1</sup> . ....	155
<b>Table 17:</b> CH <sup>35</sup> Cl vibrational frequencies /cm <sup>-1</sup> . ....	157
<b>Table 18:</b> Fit parameters for CH <sup>35</sup> Cl. The parenthesis encloses the standard deviation in the average parameter value. ....	158



<b>Table 19:</b> Vibrational level assignments for CD <sup>35</sup> Cl. Energies are in cm <sup>-1</sup> . .....	161
<b>Table 20:</b> Fitted vibrational frequencies against the <i>ab initio</i> calculations using B3LYP/aug-cc-pVTZ level of theory for CD <sup>35</sup> Cl. Vibrational frequencies are in cm <sup>-1</sup> . .....	163
<b>Table 21:</b> Shows the fit parameters obtained during the fitting of the calculated energy levels to the experimental values for CD <sup>35</sup> Cl. The parenthesis encloses the standard deviation in the average parameter value.....	164
<b>Table 22:</b> Summarization of the singlet-triplet energy gap results in mono halocarbenes/cm <sup>-1</sup> . .....	165
<b>Table 23:</b> Comparison of atomic versus carbene spin-orbit coupling constants / cm <sup>-1</sup> . .....	167

## TABLE OF FIGURES

<b>Figure 1:</b> Two ways by which halogen bonding can be achieved between bromobenzene monomers. The blue region represents the most electropositive region and the red region is most electronegative.....	3
<b>Figure 2:</b> Types of non-covalent aromatic interactions in a benzene dimer. ....	5
<b>Figure 3:</b> Schematic electronic energy level diagram showing possible transitions in organic compounds. ....	7
<b>Figure 4:</b> One-color R2PI technique. A neutral molecule M in ground state absorbs one photon, reaches an intermediate level M*, and then absorbs another photon of same energy to reach an excited ionized state M <sup>+</sup> . ....	9
<b>Figure 5:</b> CASPT2 diabatic potential- energy curves along the C <sub>6</sub> H <sub>5</sub> -Br bond distance of 5 states in bromobenzene taken from Liu paper. <sup>101</sup> .....	21
<b>Figure 6:</b> (a) Experimental setup showing the laser beam path into the vacuum chamber. (b) Schematic experimental setup used for REMPI the experiments. ....	25
<b>Figure 7:</b> Bromobenzene dimer conformations and their respective binding energies calculated at M06-2X/aug-cc-pVDZ. ....	28
<b>Figure 8:</b> R2PI mass spectrum of bromobenzene. The two different Br isotope monomer units are well resolved as well as their dimer combinations.....	30
<b>Figure 9:</b> R2PI spectra of mass selected bromobenzene monomer. The origin band is at 37008 cm <sup>-1</sup> . Vibrational mode assignments taken from reference. <sup>78</sup> .....	31
<b>Figure 10:</b> Resonant two-photon ionization (R2PI) spectra of mass selected bromobenzene dimer in the region of the origin band of the S <sub>0</sub> -S <sub>1</sub> (π-π) transition of the monomer. ....	33
<b>Figure 11:</b> R2PI spectra of mass selected chlorobenzene monomer (n=1) and clusters (Chlbz) <sub>n</sub> where n=2-5. The general trend of broadness was observed, a sign of possible presence of multiple isomers. ....	34
<b>Figure 12:</b> The R2PI spectra of bromobenzene dimer. Spectrum (1) recorded under optimum conditions for the dimer formation as well as any other higher order cluster. Spectrum (2) was taken under experimental conditions that were free from higher order clusters. ....	35

<b>Figure 13:</b> Representative calculated TDDFT (TDCAM-B3LYP/aug-cc- pVDZ) spectra of the bromobenzene dimers D1–D6. The calculated energy has been scaled and referenced to the observed position of the origin band of the monomer. ....	37
<b>Figure 14:</b> Calculated TDDFT (TDCAM-B3LYP)/aug-cc-pVDZ) spectra of the bromobenzene dimers. The calculated energy has been scaled and referenced to the observed position of the origin band of the monomer. ....	38
<b>Figure 15:</b> Optimized structures of dimers D3, D4 and D6 in the $S_0$ and $S_1$ states, obtained from TDM06-2X/aug-cc-pVDZ calculations. ....	39
<b>Figure 16:</b> R2PI spectra of mass-selected (a) bromobenzene monomer and (b) mixed bromobenzene–benzene dimer and (c) trimer in the monomer $S_0$ – $S_1$ transition region of the monomer. ....	41
<b>Figure 17:</b> Optimized structures (MD1–MD4) and binding energy for the mixed bromobenzene–benzene dimer, calculated at the M06-2X/ aug-cc-pVDZ level of theory. The binding energies are counterpoise and ZPE corrected. ....	42
<b>Figure 18:</b> Calculated TDDFT (TDCAM-B3LYP/aug-cc-pVDZ) spectra of the mixed bromobenzene–benzene dimers. The calculated energy has been scaled and referenced to the observed position of the origin band of the monomer. ....	43
<b>Figure 19:</b> Optimized bromobenzene trimer structures (T1–T6) and mixed bromobenzene-benzene trimmers and their corresponding binding energies(kJ/mol), calculated at the M06-2X/ aug-cc-pVDZ level of theory. The binding energies are counterpoise and ZPE corrected. ....	46
<b>Figure 20:</b> Resonant R2PI spectra of mass-selected bromobenzene monomer, trimer and mixed bromobenzene–benzene trimer in the region of the origin band of the $S_0$ – $S_1$ ( $\pi\pi^*$ ) transition of the monomer. ....	47
<b>Figure 21:</b> Calculated TDDFT (TDM06-2x/aug-cc-pVDZ) spectra of the .....	48
<b>Figure 22:</b> Optimized structures and binding energies (in parenthesis) of four minimum energy PhCl-NH <sub>3</sub> dimers structures (D1-D4) at M06-2X/aug-cc-pVDZ level. ....	50
<b>Figure 23:</b> R2PI spectra of PhCl monomer and PhCl—NH <sub>3</sub> complex (measured in the protonated aniline mass channel due to the fast intracluster reaction upon ionization). ..	51
<b>Figure 24:</b> Predicted positions of the electronic origins of the PhCl monomer and two $\sigma$ -type structures of the PhCl—NH <sub>3</sub> complex obtained from TDM06-2X/aug-cc-pVTZ calculations. The calculated transition energies have been scaled to match the experimental origin of the monomer. ....	52

<b>Figure 25:</b> Ground state optimized geometries and binding energies (kJ/mol) for the PhBr-NH <sub>3</sub> 1:1 dimer. ....	61
<b>Figure 26:</b> R2PI TOF mass spectrum for PhBr-NH <sub>3</sub> system. An=aniline, AnH=protonated aniline. ....	63
<b>Figure 27:</b> R2PI spectra of PhBr collected from the phenyl cation mass channel (top spectrum) and from the PhBr mass channel (bottom spectrum). The two spectra are identical, signifying a common source. ....	64
<b>Figure 28:</b> Schematic representation of process occurring after the photoionization of PhBr and PhBr-NH <sub>3</sub> complex. Two competing reaction pathways leading to the elimination of Br atom and HBr are shown. ....	66
<b>Figure 29:</b> R2PI spectrum of PhBr-NH <sub>3</sub> van der Waals cluster obtained by scanning the protonated aniline mass channel. ....	68
<b>Figure 30:</b> TDDFT calculations of the transition energy of the PhBr monomer (M) and five minimum energy structures. The energies were scaled (0.86 scaling factor) with reference to the experimental PhBr monomer absorption. ....	71
<b>Figure 31:</b> The experimental R2PI spectra for PhBr-NH <sub>3</sub> complex collected over the phenyl cation mass channel. The simulation is shown for the most stable $\sigma$ -type (D2) isomer. The stick spectrum is convoluted with a Lorentzian linewidth of 3 cm <sup>-1</sup> . ....	73
<b>Figure 32:</b> The experimental R2PI spectra for PhBr-NH <sub>3</sub> complex was collected over the phenyl cation mass channel. The simulation is shown for the most stable $\pi$ -type (D4) isomer. The stick spectrum is convoluted with the Lorentzian linewidth of 3 cm <sup>-1</sup> . ....	74
<b>Figure 33:</b> One-color R2PI spectra of mono substituted halobenzenes, PhX (black) and corresponding van der Waals dimer complex with NH <sub>3</sub> (red). All dimers are blue shifted with respect to the PhX monomer origin. ....	77
<b>Figure 34:</b> R2PI spectrum of aniline. The assignments of the vibrational modes is obtained from reference. <sup>93</sup> ....	82
<b>Figure 35:</b> Aniline-CF <sub>3</sub> Cl van der Waals dimer system calculated at M06-2X/aug-cc-pVDZ level of theory. The binding energies are corrected for basis set superposition error and zero point energy. ....	83
<b>Figure 36:</b> Aniline-CF <sub>3</sub> Br van der Waals dimer system calculated at M06-2X/aug-cc-pVDZ level of theory. The binding energies are corrected for basis set superposition error and zero point energy. ....	84

- Figure 37:** Aniline-CF<sub>3</sub>I van der Waals dimer system calculated at M06-2X/aug-cc-pVDZ-PP level of theory. The binding energies are corrected for basis set superposition error and zero point energy. .... 85
- Figure 38:** Relative excitation energies calculated for D1 and D2 conformers of the An-CF<sub>3</sub>I system. The energies are scaled using the experimental aniline monomer (M) origin transition. .... 86
- Figure 39:** IR stretching N-H frequencies of An-CF<sub>3</sub>I dimers D1, D2 and that of the monomer (free aniline molecule). .... 88
- Figure 40:** Electronic structure of mono-halocarbenes, CHX (X=I, Br, Cl, F). The bond angle is approximately 100° for the singlet states and about 130° for triplet excited states. S<sub>0</sub> is the singlet ground state, S<sub>1</sub> and S<sub>2</sub> are excited singlet states, T<sub>1</sub> is the first excited triplet state. .... 94
- Figure 41:** Energy level diagram for monohalocarbenes, showing how the singlet-triplet energy gap varies with the atomic size of the halogen atom on the molecule. S<sub>1</sub> and S<sub>2</sub> energies taken from literature.<sup>174</sup> .... 108
- Figure 42:** A potential energy surfaces for CHI in the lowest triplet state and two lowest singlet states interpolated from *ab initio* DFT calculations at B3LYP/sadlej-pVTZ level of theory. .... 113
- Figure 43:** Frank-Condon factors for selected levels in CHI and CDI simulations. As expected, the largest FCF are between the interaction of the triplet origin with bending singlet levels (red bars). The blue bars represent combination levels involving C-I stretch ( $\nu_1 = 1$ ) and a bending mode ( $\nu_1=1,2\dots$ ). The black bars represent C-H stretch and some combination vibrational levels involving the C-I and C-H stretching modes. .... 119
- Figure 44:** shows Frank-Condon factors for selected levels in CHBr and CDBr simulations. The tall red drop lines represent FCF between the triplet origin overlap with bending singlet levels. The blue drop lines represent combination levels involving C-I stretch ( $\nu_1 = 1$ ) and a bending mode ( $\nu_1=1,2\dots$ ). The black drop lines represent C-H stretch and some combination vibrational levels involving the C-I and C-H stretching modes. .... 120
- Figure 45:** Frank-Condon factors for selected levels in CHCl and CDCl simulations. The largest FCF were predicted for the overlap between the triplet origin with bending singlet levels (red drop lines). The blue drop lines represent combination levels involving C-I stretch ( $\nu_1 = 1$ ) and a bending mode ( $\nu_1=1,2\dots$ ). The black drop lines represent C-H stretch and some combination vibrational levels involving the C-I and C-H stretching modes. .... 121

**Figure 46:** Schematic diabatic one dimensional picture of spin-orbit coupling in halocarbenes. The spin-orbit coupling is factorized into a purely electronic part and a nuclear part reflecting the vibrational overlap of the singlet and the triplet wavefunctions. .... 125

**Figure 47:** Shows an XY-plane Duschinsky transformation in CDI molecule. The dotted lines joins matching atoms or motions..... 127

**Figure 48:** Setting up of the Hamiltonian matrix. The initial singlet and triplet eigenvalues are approximated by the Dunham Expansion. The matrix elements are obtained by simulation from Pgopher and multiplying by a spin-orbit coupling fitting parameter..... 129

**Figure 49:** Shows the stick energy diagram of the calculated and observed term energies for CHI system. The first black column displays some calculated singlet levels without spin orbit coupling. The second green column shows some fitted singlet levels, and fitted triplet levels are in the last blue column. The third red column displays mixed observed levels from reference<sup>166, 167</sup> ..... 135

**Figure 50:** The stick energy diagram of the calculated and observed term energies for the CDI system. The first black column displays some calculated singlet levels without spin orbit coupling. The second green column shows some fitted singlet levels, and fitted triplet levels are in the last blue column. The third red column displays mixed observed levels from reference<sup>167</sup> ..... 140

**Figure 51:** CHBr term energy diagram which compares the predicted singlet and triplet level positions to the experimental mixed levels. The first black column displays calculated singlet energy levels without spin orbit coupling. The second and last column shows some fitted singlet and triplet energy levels that incorporated spin orbit coupling respectively. The third column displays mixed observed levels from reference<sup>141</sup> ..... 147

**Figure 52:** A zoom-in CHBr term energy diagram on upper lying levels in Figure 51. The region is where perturbations are most intense..... 148

**Figure 53:** Term energy diagram for CDBr which compares the predicted singlet and triplet level positions. The first black column displays calculated singlet energy levels without spin orbit coupling. The second and last column shows some fitted singlet and triplet energy levels that incorporated spin orbit coupling respectively. The third column displays mixed observed levels from reference<sup>165</sup> ..... 153

**Figure 54:** Stick energy diagram for CH<sup>35</sup>Cl. The fitted S<sub>0</sub> and T<sub>1</sub> term energies (with spin orbit coupling) are shown in the second and last column. The calculated singlet energies (without spin orbit coupling) are shown in the first black column. The observed term energies shown in the third column were taken from references<sup>168, 170</sup> ..... 159

**Figure 55:** Comparison of derived spin-orbit coupling constants with those of the bare halogen atoms using data in Table 23. The black symbols represent CHX and the red points CDX. The blue diamond is the fluorine atomic spin orbit coupling constant from reference <sup>206</sup> ..... 168

## CHAPTER 1: RESONANT TWO-PHOTON IONIZATION STUDIES OF NON COVALENT INTERACTIONS

### 1.1 INTRODUCTION TO NON-COVALENT INTERACTIONS

Non-covalent interactions are attractive forces that are not covalent in nature; these include Van der Waals forces, halogen bonding, hydrogen bonding,  $\pi$ - $\pi$  stacking and CH- $\pi$  interactions. These interactions are important in a wide field of biochemical processes, influencing reactivity, molecular structure, molecular recognition and binding.<sup>1-5</sup> They are mainly found in macro biological molecules such as proteins and nucleic acids where they are involved in chemical reactions and have a big influence on their chemical and physical properties.<sup>6-9</sup> A good example is the double helix of DNA strand, the structure of the helix is well known to be sustained by non-covalent interactions. Enzyme substrate binding antibody antigen association is all known to be influenced by some non-covalent interactions. The interactions are also known to co-exist in competition with each other and also to partner each other to achieve a particular goal involving maintaining molecular structures and chemical reactions. The study of non-covalent interactions have received a fair share of attention in recent years, the majority of the researchers have opted to use benzene and its derivative.<sup>5, 7-17</sup>



### 1.1.1 HALOGEN BONDING

The electron density that surrounds a covalently bonded halogen nucleus is generally anisotropic, meaning it possesses different physical properties along different axes of measurement. It is because of this anisotropy that halogen atoms are involved in a wide variety of intermolecular interactions. Halogen bonding can be defined as any non-covalent interaction involving a halogen atom as electron acceptor.<sup>18, 19</sup> This can be represented by a general scheme  $R-X\cdots Y$  where X can be Cl, Br, I and Y is a negative site such as the  $\pi$ -cloud electron system of aromatic molecules.<sup>20, 21, 22, 23</sup> The positive electrostatic region found on a halogen atom that is covalently bonded to an electron withdrawing residue is known as the “ $\sigma$ -hole”. Through the  $\sigma$ -hole, the halogen can interact attractively with a negative site of Lewis base and this type of interaction is highly directional. Figure 1 helps to illustrate this using two bromobenzene monomer units. The strength of halogen bonding depends on a number of factors such as the ability of polarization of electronic charge around the halogen atom and the electron withdrawing power of the remainder of the molecule.<sup>24</sup> For a given electron withdrawing residue, the  $\sigma$ -hole potential on the halogen becomes more positive as its polarizability increases, that is,  $Cl < Br < I$ .<sup>20, 21, 24</sup> Halogen bonds are of particular interest in biochemistry and medicinal chemistry because they are involved in protein-ligand interactions and in the design of novel ligands that interacts with proteins in a very specific manner. One type of halogen bond that is of great interest in biochemistry is one that involves the interaction between a halogen and the oxygen in a carbonyl group.<sup>24-31</sup>

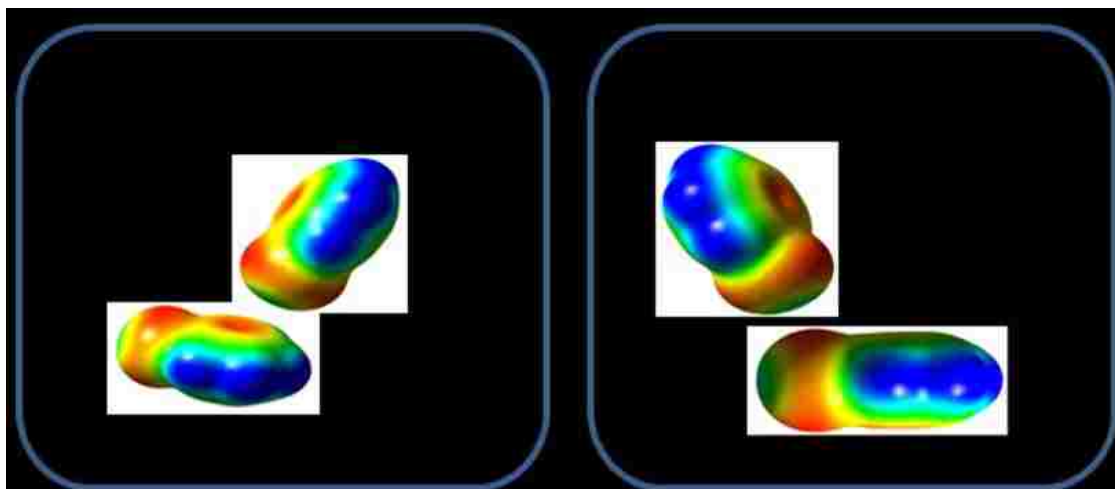


**Figure 1:** Two ways by which halogen bonding can be achieved between bromobenzene monomers. The blue region represents the most electropositive region and the red region is most electronegative.

### 1.1.2 $\pi$ - $\pi$ INTERACTIONS

Attractive non-bonded interactions between aromatic rings, known as  $\pi$ - $\pi$  interactions are seen in many areas of biochemistry, controlling structural organization and recognition processes in biomolecules.<sup>32, 33</sup> Interactions between aromatic rings are largely responsible for DNA base-pair stacking,<sup>34-37</sup> host-guest complexation<sup>12, 38</sup> and the tertiary structure of proteins.<sup>39</sup> In biologically related areas of chemistry, aromatic-aromatic interactions are crucially involved in protein-deoxynucleic acid (DNA) complexes where interactions between aromatic residues and base pairs are seen in x-ray crystal structures.<sup>40</sup> Certain drugs rely on  $\pi$ - $\pi$  interactions for intercalation into DNA.<sup>41</sup>

The forces experienced between the two  $\pi$  systems are very weak Van der Waals forces; London-Dispersion and electrostatic attractions.<sup>42, 43</sup> Since  $\pi$ - $\pi$  interactions are so prevalent across chemistry and biochemistry, a large body of experimental and theoretical work has focused on determining the gas phase structure of the prototypes, benzene dimer and toluene dimer.<sup>5, 6, 8, 14, 17, 44</sup> For the benzene dimer, the parallel displaced and T-shaped structures are the most commonly cited orientations. The frequently discussed benzene dimer conformations are the three shown in Figure 2. The sandwich conformer has both rings on top of each other whilst the T-shaped configuration, also called CH/ $\pi$ , has one benzene ring pointing into the center of the other ring. The parallel displaced configuration comes from the sandwich configuration that has gone under a parallel shift of one of its rings away from the other ring. Regardless of maximum overlap that maximizes dispersion interactions, the sandwich structure is rarely observed in systems containing phenyl rings. The other two conformers are often seen in crystal structures<sup>45</sup> or in pairs of interacting aromatic side chains in proteins.<sup>39, 45</sup> Experimental and large scale *ab initio* electronic structure theory suggests that the parallel displaced and T-shaped structures are nearly iso-energetic.<sup>6, 17, 46, 47</sup>

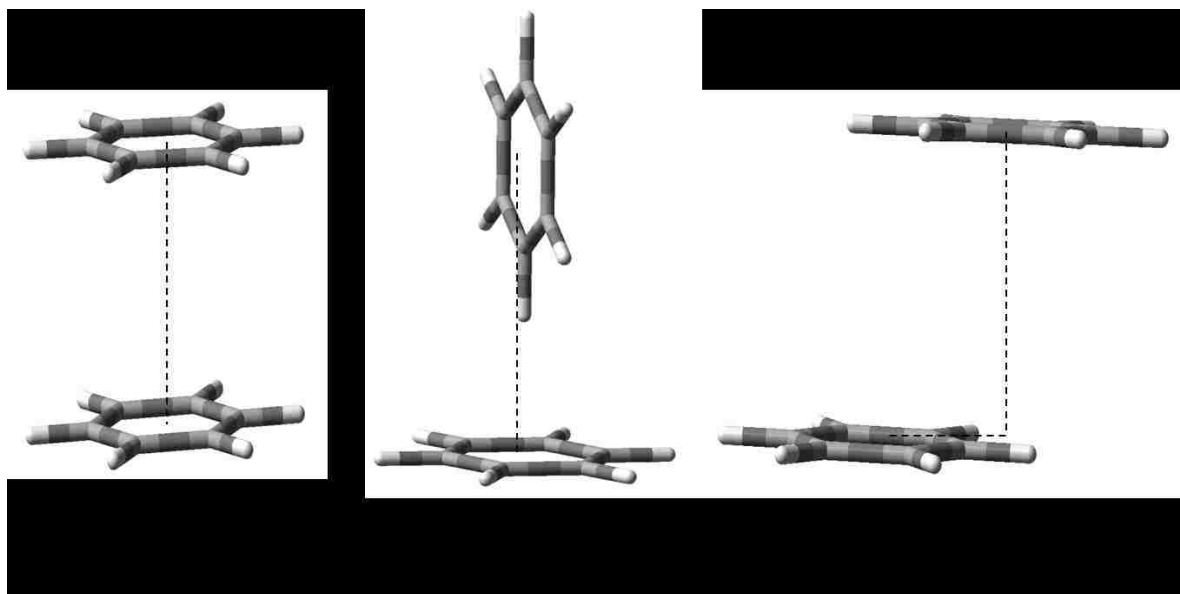


**Figure 2:** Types of non-covalent aromatic interactions in a benzene dimer.

### 1.1.3 CH/ $\pi$ INTERACTIONS

Ab initio calculations have been used to characterize the nature of interactions in a variety of CH/ $\pi$  bound systems, they are noted as mainly attractive electrostatic, dispersion and charge transfer interactions.<sup>5, 48-54</sup> The hydrogen atom of a C–H bond has a partial positive charge, whilst the  $\pi$ -cloud is has a negative electrostatic potential.<sup>18, 48</sup> There exist an attractive electrostatic interaction between the hydrogen atom of the C–H bond and the  $\pi$ -electron cloud in which the C–H bond points toward the aromatic ring. The ability of aromatic molecules to be polarized and the existence of short carbon-carbon distances in the CH/  $\pi$  clusters are the cause of the existence of dispersion interactions.

The charge-transfer interaction may also coexist in some CH/  $\pi$  bound systems. The electrostatic interaction is highly orientation dependent interaction, while the orientation dependence of the dispersion interaction is weak.<sup>55,56</sup> A wide number of CH/ $\pi$  interactions in proteins have been involved in a wide variety of functions such as secondary structure stabilization<sup>57</sup>, drug recognition<sup>58</sup>, DNA recognition<sup>59</sup> and enzyme action<sup>60</sup>. In this study, CH/ $\pi$  interactions are studied in the halobenzene cluster systems using R2PI technique and DFT calculations.

### 1.1.3 TYPE OF TRANSITIONS IN HALOBENZENES.

The lowest electronic absorptions of organic compounds is based on transitions of  $n$  or  $\pi$  electrons to the  $\pi^*$  excited state. Figure 3 illustrates these transitions. The excitation ( $S_0 \rightarrow S_1$ ) of a halogenated benzene molecule (PhX) where (X=F, Cl, Br, I) is based on  $\pi \rightarrow \pi^*$  transition, and the ionization from the  $S_1$  state corresponds to a removal of a  $\pi$  electron from the neutral molecule.<sup>61,62</sup> An electron in a bonding  $\sigma$ -orbital can be excited to a corresponding antibonding orbital ( $\sigma \rightarrow \sigma^*$ ) but this requires a lot of energy. A good example is in methane which has only C-H bonds, and can only undergo  $\sigma \rightarrow \sigma^*$  transitions and shows an absorbance maximum at 125 nm. The wavelengths of this type of electronic transition are too low to be observed in a typical UV-Vis spectra.<sup>63</sup> Another type of an electronic transition is the excitation of a non-bonding electron in a  $n \rightarrow \sigma^*$  type of transition. This is very common in saturated compounds with lone pairs of electrons. Unlike the  $\sigma \rightarrow \sigma^*$  transition, the  $n \rightarrow \sigma^*$  requires less energy (150-250nm).<sup>64</sup>

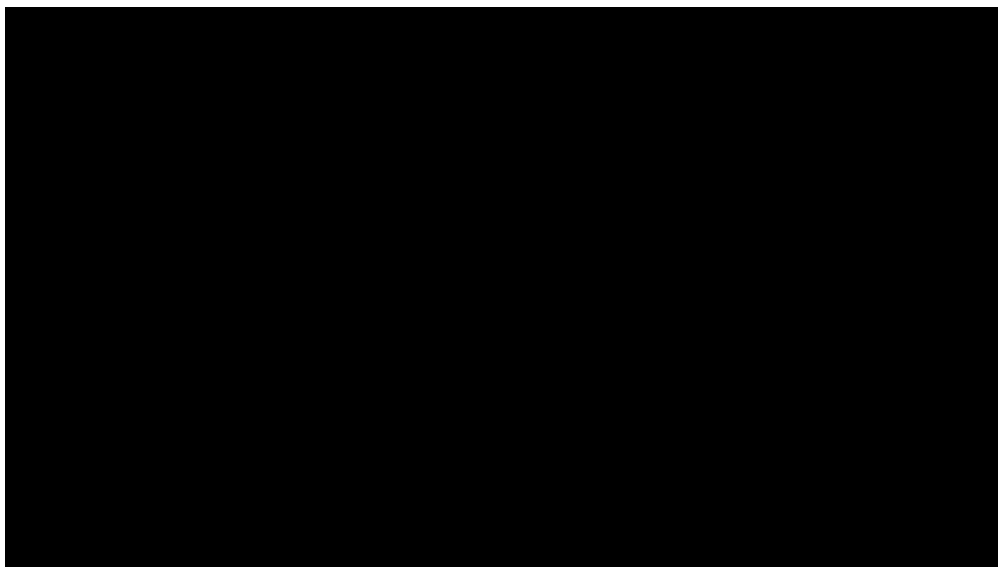


**Figure 3:** Schematic electronic energy level diagram showing possible transitions in organic compounds.

#### 1.1.4 SPECTRAL SHIFTS IN HALOBENZENES

Spectral shifts of  $\pi \rightarrow \pi^*$  transition of an aromatic chromophore such as halogenated benzenes can result in a spectral shift upon the electronic transition when they form non-covalent clusters. The shift can be either to the lower energy of the  $S_0-S_1$  transition energy of the monomer molecule, this is known as spectral red shift and results in the lowering of the transition energy between the ground and the excited state of a chromophore. If the spectral shift results in the increment of the transition energy, it is called blue shift. The interaction of the monomer molecules in forming clusters can stabilize or destabilize the electronic excited states relative to the ground state. Whether the interaction results in a stabilization rather than destabilization depends on the type of chromophore and the type of electronic transition taking place. In the halobenzene clusters under study here, both spectral red-shift and blue-shift was observed.

## 1.2 EXPERIMENTAL METHODS

### 1.2.1 THE PRINCIPLE OF R2PI-TOF TECHNIQUE

A molecule can be induced to absorb two photons simultaneously into its excited ionized state as long as the intensity of the light is at least of the threshold limit.

Resonant-two photon ionization (R2PI) uses a stepwise resonant excitation of a molecule via stable intermediate energy levels as illustrated in Figure 4. A molecule (M) in its ground state absorbs monochromatic laser light of high energy flux density ( $\lambda_1$ ) and is electronically excited to an intermediate state ( $M^*$ ). The excited molecule absorbs a second photon of the same wavelength leading to ionization. This is also known as one-color R2PI. The advantage of it is that, it allows us to study high lying electronic excited states providing more spectroscopic information that can be unavailable to single photon spectroscopic methods.

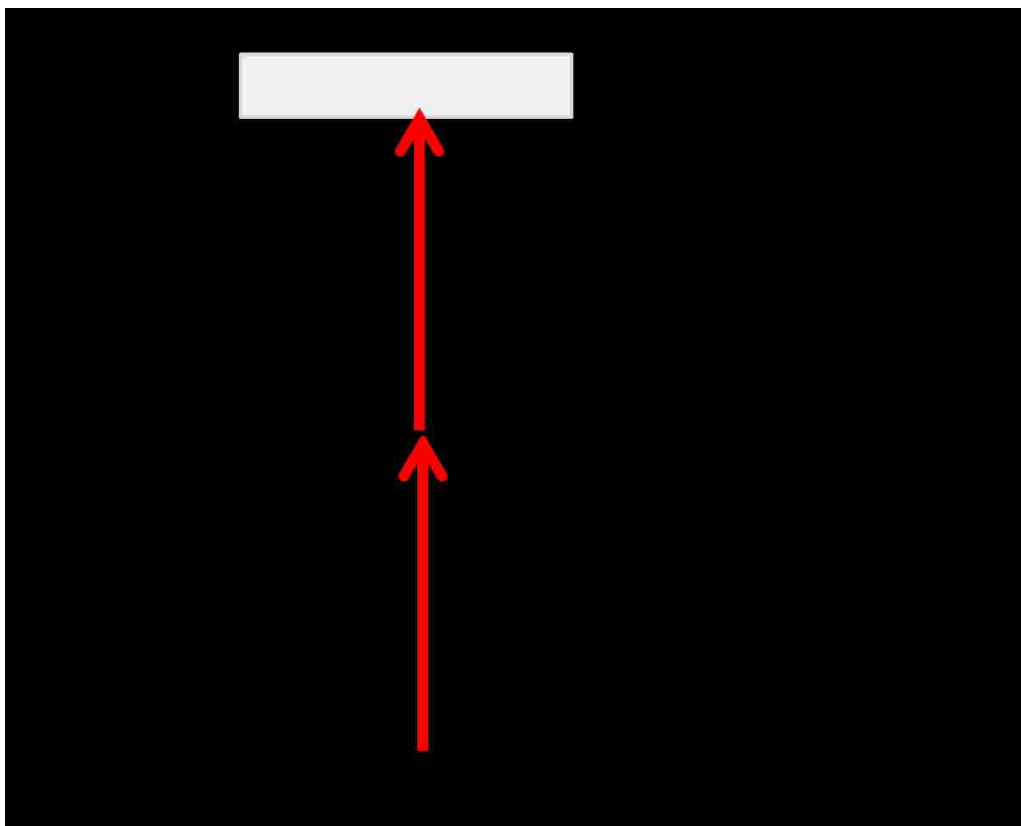


**Figure 4:** One-color R2PI technique. A neutral molecule  $M$  in ground state absorbs one photon, reaches an intermediate level  $M^*$ , and then absorbs another photon of same energy to reach an excited ionized state  $M^+$ .

### 1.2.2 TIME OF FLIGHT MASS SEPARATION

A charged particle  $m$ , in an electric field  $V_{ext}$  possesses potential energy  $E_p$ . When the charged particle is accelerated into time-of-flight tube by the voltage  $V_{ext}$ , its potential energy is converted to kinetic energy, hence:

$$E_p = qV_{ext} = \frac{1}{2}mv_z^2$$



Where  $m$  is the mass of the fragment,  $q$  is the charge of the ion,  $V_{ext}$  is the electric field in the extraction region. This equation when simplified leads to:

$$\frac{m}{q} = 2 \frac{V_{ext}}{d^2} t^2 = kt^2$$

Where  $d$  is the distance travelled by the ions before hitting the detector (length of flight tube),  $t$  is the time taken to reach that detector, and  $k$  is a constant if  $V_{ext}$  is fixed. One can therefore predict the exact position of an ion species of a particular mass per charge in a mass spectrum quite easily by applying this relationship. From the extraction region, ions are accelerated and gains kinetic energy, ions of the same charge gains equal kinetic energy. The velocity gained by the ions along the linear flight tube depends on mass-to-charge ratio, and the flight time for the ion fragment to reach the detector placed at a known distance can be measured. From this time and the known experimental parameters one can find the mass-to-charge ratio of the ion. The mass spectrum can have a small spread in arrival time of ions of the same mass to charge ratio due to temporal, spatial and kinetic energy distribution. Temporal spread between two identical ions is due to differences in formation time within the same laser pulse whilst spatial spread is due to the fact that ions are formed in from different locations within the ion source chamber, with respect to the extraction plate. Those ions formed close to the extractor plate will feel more positive potential and are accelerated faster than ions formed away from the extractor plate. To improve separation and resolution of the ionic species reaching the detector on the spectrum, a reflectron can be employed in a non-linear TOF tube.

A reflectron uses a constant electrostatic field to reflect the ion beam toward the detector. From the law of inertia, lighter ions will make a wider curvature taking slightly more time than heavier ions possessing same kinetic energy or mass per charge. Here no reflectron is employed since enough separation and resolution of the ion fragments was achieved. A dual micro-channel plate is usually used as the detector of the ionic species. It is placed a distance away where ions hit its surface and are counted with respect to the onset of the extraction pulse in the ion source chamber.

### 1.2.3 FORMATION OF MOLECULAR CLUSTERS- SUPERSONIC JET METHOD

Non covalent molecular clusters are usually produced in continuous or pulsed supersonic beams. If the precursor is solid at room temperature, there is need to heat the sample to create enough vapor pressure. To obtain both an efficient cooling rate and formation of vdW clusters, the seeded beam technique is applied. Usually the mixing ratio of the sample gases to the seeding gas (He, Ne, Ar, etc) ranges between 1 – 5%. Solid samples are evaporated in heated nozzle sources, thus allowing the seed gas to pick up their vapor. The heating needs to be done very close to the nozzle inside the vacuum chamber to prevent condensation inside the delivery tubes. A liquid sample requires a bubbler where the seed gas is bubbled through and picks up the sample vapor. The bubbler could be placed in a bath if further control of the vapor pressures is required. This gas mixture is expanded at high pressure through a tiny nozzle, with a typical diameter of 1mm or less, into high vacuum.

A supersonic free jet is formed from the nozzle when the gas pulse expands upon moving from a region of high pressure to a region of low pressure background through a small circular aperture.<sup>65</sup> The constriction on the nozzle, according to fluid mechanics principles, should create a pressure difference that in turn accelerates the stagnation gas. Depending on the orifice size, the gas flow will either exit the nozzle at supersonic, sonic or subsonic speeds.<sup>66</sup>

The supersonic expansion has a cooling effect on the molecular beam. Relatively large concentrations of molecular clusters can be formed in the process.<sup>67</sup> This could be an advantage or a disadvantage to the investigators depending on what they are after. In this case, it is used as an advantage to study weakly bound molecular clusters in halo aromatic complexes. A clean spectrum is expected when rotational temperature is low since it is associated with depopulation of excited internal energy states that leads to a reduction in spectral congestion. Low background pressure requires large diffusion pumps and large chambers. The cooling process of the seeded molecular species is a binary body collision process with the seeding gas molecules, while the formation of a cluster like a dimer requires a three-body collision process.<sup>66</sup> First the two cooled monomer units need to interact in the presence of an inert seeding gas particle to carry away the excess energy generated. Within the expanding gas pulse, monomers and smaller clusters appear at the beginning and at the end of the pulse while larger complexes show up in its center.<sup>66</sup>

The observed cluster size distribution may be controlled within certain limits by varying experimental parameters such as (1) the valve pulse duration, (2) the mixing ratios of the gases and the stagnation pressure of the gas mixture, and (3) the part of the gas pulse sampled with the cluster detection method. A very sensitive and mass-selective detection method widely used nowadays to study clusters is resonant two-photon ionization (R2PI).

Challenges associated with the generation and subsequent detection of these molecular clusters have been known to be, (1) stabilization of the clusters long enough to allow probing, this can only be done at very low temperatures (2) difficult to control complexation, many undesired cluster combinations are formed in competition with the desired cluster size, (3) clusters easily fragment upon excitation or ionization.<sup>68</sup> The approach used here combines supersonic jet methods with mass spectrometry and resonant multi-photon ionization technique.

## 1.3 COMPUTATIONAL METHODS

### 1.3.1 DENSITY FUNCTIONAL THEORY (DFT) METHODS

DFT describes an interacting system of atoms, nuclei, protons or electrons via its particle density and not via its many-body wave function. It can predict molecular properties such as molecular geometries, vibrational frequencies, ionization energies, etc. As compared to Hartree Fock (HF) and post-HF methods, DFT saves a lot on computational costs as it takes less computational time.

The wave function  $\phi$  of an N-electron system includes  $3N$  variables, while the density,  $\rho$  no matter how large the system is, has only three variables  $x$ ,  $y$ , and  $z$ . As compared to HF method, DFT methods are a major improvement as they provide approximations for the exchange-correlation potential. DFT exchange-correlation energy functionals can be either pure or hybridized. The common pure methods consist of BLYP,<sup>69</sup> PW91 and SVWN5. Similarly, the hybrid DFT method consists of B3PW91, B3LYP, M06, M06-2X and CAM-B3LYP. The CAM-B3LYP functional comprises of 0.19 Hartree–Fock (HF) plus 0.81 Becke 1988 (B88) exchange interaction at short-range, and 0.65 HF plus 0.35 B88 at long-range.<sup>70</sup> Zhao and coworkers developed hybrid M06-2X functional and recommended its use for non-covalent interactions as they found it performs well in describing non covalent interaction energies.<sup>71</sup> This functional was then benchmarked by Sherrill and co-workers who did some extensive computational work on related non covalent clusters employing different DFT methods and they found out M06-2X was the most cost effective method.<sup>9</sup>

### 1.3.2 TIME-DEPENDENT DENSITY FUNCTIONAL THEORY (TD-DFT) METHODS

TDDFT maps the excited state properties by using time evolving electronic density. Since DFT alone (without the time dependent part) is applied on a non-interacting system in its ground state; however, in TDDFT, an external field is turned on (electric, magnetic or electromagnetic) upon an interacting system and obtain all its excited state properties contained in its electron density by merely analyzing its time evolving electron density.

The effect of such fields on molecules can be studied to extract properties like excitation energies, Frank-Condon factors, vibrational frequencies and photo-absorption spectra. TDDFT calculations are based on the fact that the linear response function – that is, how the electron density changes when the external field changes – has poles at the exact excitation energies of a system.<sup>72</sup> The most popular application of TDDFT is in the calculation of the energies of excited states of isolated systems.

### 1.3.3 COUNTERPOISE CORRECTION AND BASIS SET SUPERPOSITION ERROR (BSSE)

It was noticed that in studying transition states, reactions and non-covalent interactions or simply any weak interaction in molecular clusters, for example  $\pi$ -stacked halobenzene dimers, that there may exist an artificial shortening of intermolecular distances.<sup>73, 74 43</sup> This shortening then leads to an artificial stabilization of the cluster system. This may mislead researchers studying such systems in thinking the cluster is stable when it's not.<sup>75</sup> This effect was found to be more significant for smaller basis sets. A counterpoise correction is then a theoretical method to limit an error that results when studying an intermolecular interactions or reactions using an incomplete basis set. Take for instance in the case of chlorobenzene-ammonia dimer; the PhCl can utilize the extra basis functions from NH<sub>3</sub> to describe its electron distribution, leading to the overestimated binding strength of the dimer.

$\text{NH}_3$  can also do the same by utilizing basis functions of the PhCl as the two monomer units come into close proximity when forming a molecular cluster. Using more basis set functions or diffused functions to describe the electron distribution that is far away from the atomic nucleus can improve a calculation but comes at computational cost. To go around this, the basis set localized on one monomer can be diffused enough to be accessed by the electrons from the other monomer. If one uses a sufficiently accurate description of the atomic orbitals far away from the atomic centers, it wouldn't make any difference if the additional functions occupy that same long range centers. The added basis functions from the other reactant are unnecessary and won't improve the quality of the calculation.<sup>76</sup> As said before, it's not always that one has an option of utilizing larger basis sets, however, one can do a quicker and simpler counterpoise correction calculation, and the calculation approximates the extra stabilization energy. The counterpoise correction takes into consideration the calculated equilibrium structures of the monomers/cluster or reactants in doing the calculation.<sup>77</sup> Monomer units far apart or too close from one another will produce insignificant correction energy because in those two scenarios, either the basis functions are too far to be accessed or too close to be useful to the diffused electron density.

## CHAPTER 2: BROMOBENZENE CLUSTERS

### 2.1 INTRODUCTION TO BROMOBENZENE CLUSTERS

In halobenzenes, halogen bonding, hydrogen bonding, CH- $\pi$ , may all co-exist in competition or cooperation. Thus, many researchers use phenyl halides as good prototypical systems of studying the competition of these forces.<sup>5, 11, 13, 15, 78-86</sup> In this study, bromobenzene is used in mass selected resonance two-photon ionization (R2PI) spectroscopy experiments and ab initio calculations to investigate the strength and the mere existence of each force. A lot of related experimental work on non-covalent interactions in aromatic clusters, have employed the resonance enhanced multi-photon ionization (REMPI) technique.<sup>2, 5, 13-15, 44, 81, 82, 84, 85, 87, 88</sup> The possible conformations of certain aromatic clusters have also seen different views emerging, especially the competition of T-shaped and  $\pi$ -stacked conformations in benzene and halogenated benzenes.<sup>8, 12, 17, 44, 71, 87, 89-92</sup> A lot of researchers have also tried understanding the role of these non-covalent interactions by using computational methods.<sup>6, 8, 9, 17</sup> Aromatic clusters have long been model systems for understanding  $\pi$ - $\pi$  stacking and CH/ $\pi$  interactions.<sup>6</sup> Bernstein and co-workers conducted seminal studies of the R2PI spectra of toluene dimer through the  $S_1$  state, which showed two features that were significantly broadened with respect to the monomer absorption.<sup>46, 47, 85</sup>



These two features were attributed to different isomers, and this was confirmed using UV-UV hole-burning spectroscopy.<sup>44</sup> The broadness pattern is also observed in fluorobenzene<sup>15, 85</sup>, chlorobenzene<sup>13, 87</sup>, phenol and aniline<sup>93-95</sup> higher order clusters. The broadness in the higher order cluster spectra has been explained different ways by authors. However, they do agree that the formation of many isomers in the molecular beam absorbing at slightly different wavelengths is a main factor contributing to the broadness. Lu and coworkers<sup>87</sup> studied chlorobenzene and chlorobenzene-benzene complexes by 1+1 R2PI. The clusters were broad and shifted either way about the monomer position. The chlorobenzene dimer spectrum had a blue-shifted feature and a red-shifted feature. They assigned the red-shifted peak to the perpendicular T-shaped dimer structure and the blue-shifted peak was assigned to the parallel-displaced  $\pi$ -stacked structure. We recently examined noncovalent interactions in clusters of chlorobenzene (PhCl) using resonant two-photon ionization (R2PI) spectroscopy in the origin region of the  $S_0 \rightarrow S_1$  ( $\pi\pi^*$ ) state of the monomer.<sup>88</sup> The R2PI spectra of PhCl clusters exhibited a broadened spectrum whose center was red-shifted from the monomer absorption, and was similar for all cluster sizes examined (up to the tetramer). For the dimer, electronic structure calculations at the M06-2X/aug-cc-pVDZ level found five minimum energy structures, four  $\pi$ -stacked structures and one T-shaped structure bound through CH/ $\pi$  interaction; no minima corresponding to halogen bonded structures were identified. The calculated Time Dependent Density Functional Theory (TDDFT) spectra revealed that these isomers absorb over a broad range, and the calculated absorptions were red-shifted with respect to the monomer transition.

Additional spectral broadening was found to arise from Franck–Condon activity as a result of the significant geometry change in the two electronic states, where electronic excitation induces a transition from a parallel displaced to sandwich structure with a reduced separation of the two monomers.<sup>88</sup>

Musgrave and coworkers examined larger toluene clusters using R2PI methods, and found that the spectra were very similar to that of the dimer, leading them to propose a model in which the favored ( $\pi$ -stacked) binding motif of the dimer formed the core of larger clusters.<sup>14</sup> The toluene dimer spectra they obtained was very broad with two distinct red and blue shifted peaks about the monomer position.<sup>14</sup> The bromobenzene monomer has been previously studied by the REMPI technique by Dietz and coworkers three decades ago.<sup>78</sup> They observed a sharp origin peak at  $36991.5\text{cm}^{-1}$ . The origin and the ring breathing mode  $6b(b_2)$  were dominant peaks in the spectrum. Their spectrum also showed other combination bands of mode  $6b$  with other totally symmetric vibrations  $12$ ,  $18a$ , and  $9a$ . Other monomer studies using resonance enhanced multiphoton ionization techniques were done by Koplitz and coworkers and are in good agreement with previous findings.<sup>80, 81</sup> Enough information is known about the bromobenzene monomer, however there seems to be no REMPI spectra published yet for the bromobenzene higher order clusters. The clusters were more elusive to obtain using this technique than those of chlorobenzene or fluorobenzene probably due to a shortened excited state lifetime.

## 2.2 PHOTO-DISSOCIATION OF BROMOBENZENE

The  $S_0$ – $S_1$  spectroscopy and dissociation dynamics of halobenzenes have been extensively studied<sup>80, 81, 96-98</sup> and it is well appreciated that the  $S_1$  state is predissociative, being crossed by repulsive states that correlate with ground state products. In their early studies, Smalley and co-workers found that chloro- and bromobenzene could be detected using ns-scale R2PI methods through the  $S_1$  state – however, iodobenzene dissociated too rapidly to be detected. The measured lifetime of the  $S_1$  state of PhCl is  $\sim 1$  ns,<sup>99</sup> while that of PhBr is  $\sim 30$  ps.<sup>82</sup> A significantly smaller bromobenzene signal was observed as compared to chlorobenzene and fluorobenzene, this is attributed to the short lifetime of bromobenzene in the excited state. The short lived species undergo photodissociation upon excitation to the  $S_1$  state. The photodissociation process is more complicated due to the mixing of the phenyl ring excitation and the C–Br localized  $\sigma^* \leftarrow n$  transition. The  $\sigma^* \leftarrow n$  transition leads to a repulsive state, which results in a direct dissociation with halogen atom released immediately. A repulsive state has no minimum on its potential energy curve. Its potential energy smoothly decreases with increasing interatomic distance such that any molecular species excited to that state will spontaneously dissociate. The excitation of the phenyl electrons results in a delocalized  $(\pi, \pi^*)$  state, which present a predissociation character resulting from the coupling between  $(\pi, \pi^*)$  and  $(n, \sigma^*)$  states. Consequently, it brings on an indirect dissociation process.<sup>100</sup> These dissociations are due to intersystem crossings between the initially excited bound  $(\pi, \pi^*)$  singlet state ( $S_1$ -B<sub>2</sub>) and a repulsive  $(n, \sigma^*)$  triplet excited state ( $T_4$ -B<sub>1</sub>).<sup>82, 101</sup>

For bromobenzene, strong spin-orbit coupling occurs between the bound ( $S_1$ - $B_2$ ) state and the repulsive ( $T_4$ - $B_1$ ) state as shown in Figure 6. The time constants for the decay of the initially bound excited ( $\pi,\pi^*$ ) states are 700 fs for PhI, 28 ps for PhBr, 1 ns for PhCl,<sup>101</sup> and fluorobenzene (1.2  $\mu$ s),<sup>102</sup> Obviously, the dissociation times increase with decreasing atomic number of the halogen, because the spin-orbit coupling between the singlet ( $\pi,\pi^*$ ) state and the triplet repulsive ( $n,\sigma^*$ ) state is strongly enhanced by the presence of heavy substituents. Besides the coupling strength, the predissociation rate from ( $\pi,\pi^*$ ) state to the ( $n,\sigma^*$ ) state also depends on the excitation wavelength and the relative position of the potential energy curves and their crossings. Figure 5 shows the CASPT2 diabatic potential energy curves along the  $C_6H_5$ -Br bond distance for bromobenzene.

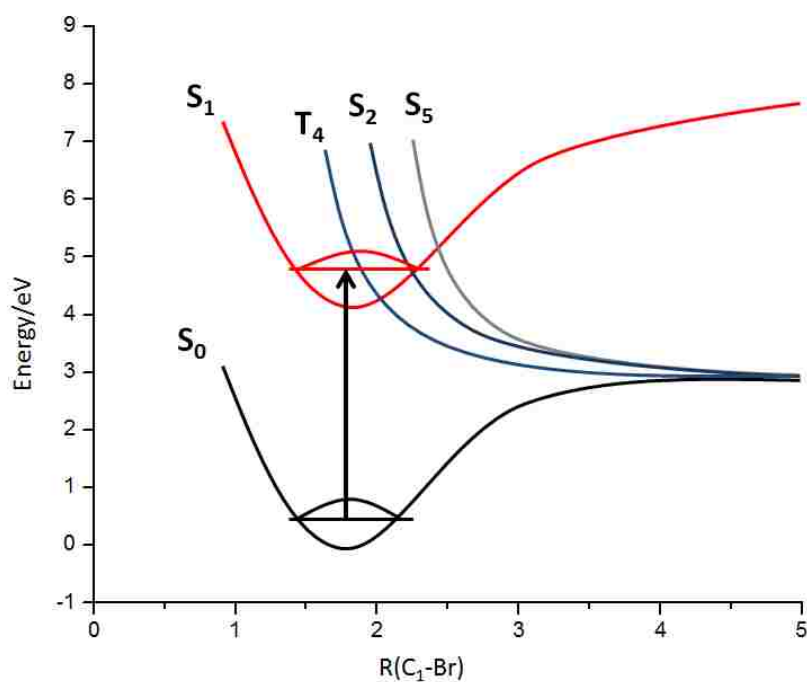


**Figure 5:** CASPT2 diabatic potential- energy curves along the  $C_6H_5$ -Br bond distance of 5 states in bromobenzene taken from Liu paper.<sup>101</sup>

## 2.3 EXPERIMENTAL SETUP

The molecular beam was formed by bubbling high purity He gas at pressures ranging between 20 to 40 psi through liquid bromobenzene (Aldrich, 99%) contained in a stainless steel bubbler at room temperature. Argon carrier gas was also tried at various backing pressures (5-120 psi) but a lot of Ar containing clusters were observed which suppressed the production of clusters of interest. Figure 6 shows the main parts of the experimental setup. The flight tube was evacuated by a 250 L/s turbo-molecular pump, with a gate valve used to isolate the detector, which was kept under vacuum at all times. The main chamber was evacuated with a water-baffled diffusion pump (Varian VHS-4). The typical pressures obtained with the nozzle in operation (working pressure) were  $\sim 6 \times 10^{-5}$  mbar in the main chamber and approximately  $2 \times 10^{-6}$  mbar in the flight tube. The background pressure in the flight tube could be lowered further by liquid nitrogen cooling of the vacuum shroud. Shrouding the flight tube with liquid nitrogen reduces background noise due to back-streaming of condensable vapors like the oil vapor. However the time of flight mass spectrometer was operated without the need of liquid nitrogen. The molecular beam is delivered into the first differentially pumped expansion chamber via flexible gas tube and a stainless steel pipe. A 0.5 mm radius pulsed nozzle that uses solenoid activation (from General Valve) is attached at the end of the sample delivery steel pipe. A General Valve pulse generator was used to control the pulse repetition or frequency (10Hz) and the pulse width ( $\sim 300 \mu\text{s}$ ).

An external trigger from a digital delay generator (Stanford Research Systems DG535) generator was used to control the pulse delay with respect to the laser pulse. The first expansion chamber is connected to the second and main expansion chamber by a 0.5 mm radius stainless steel skimmer. The skimmer was critically aligned to the 0.5 mm radius nozzle orifice. The set up allowed the mechanical movement of the nozzle back and forth, there by varying the optimum nozzle-skimmer distance. In the main chamber, a pulsed laser beam crosses the molecular beam at a right angle, this happens between the repeller and the extractor ion plate. A conventional three-plate stack was employed, with the repeller plate typically held at +2100 V, the extractor plate at +1950 V, and the third plate at ground potential. The ions produced leave the ionization region and enters the acceleration region and they quickly reach the field-free drift region. The distance between the point of formation of ions and detection by the micro-channel plates (MCPs) is 1.0 m. The molecular beam, laser beam and the detector (MCPs) are mutually orthogonal. The laser system consisted of an etalon narrowed dye laser (Lambda Physik Scanmate 2E) which was pumped by a third harmonic of a Nd:YAG laser (Continuum NY-61). Coumarin 540A was used for the dye laser, its lasing range is roughly 530-550 nm. The output of the dye laser was then frequency doubled by a incorporating a Beta Barium Borate (BBO-1) crystal, giving an output wavelength range of 265 to 285nm. The doubled laser beam of energy range 0.2 to 0.7mJ was guided into the main time of flight (TOF) mass spectrometer expansion chamber via a plano-convex focusing lens where it intersects the supersonic molecular beam in plane and at right angle. The bromobenzene monomer TOF mass spectrum could be obtained without the use of a focusing lens.

The incorporation of a focusing lens collimates the beam and boosts its energy density suitable for higher order cluster formation. Also the backing pressure was systematically varied in order to suppress the formation of particular higher order bromobenzene clusters. The MCP signal was amplified by a preamplifier (Stanford Research SRS445A) that amplified the signal by 25 times before it is processed and digitalized by a boxcar integrator (Stanford Research SRS250) that is in turn interfaced to a personal computer. A data acquisition program from National Instruments; LabVIEW, was used for controlled data acquisition and stepping of the laser wavelength. The programming was done in-house, crucial settings that could be altered for each scan are the wavelength step size (typically 0.01 nm for a low resolution and 0.002 nm for a high resolution spectrum) and number of laser shots that could be averaged per step (20 for strong ion signal and 30 for weak signals).

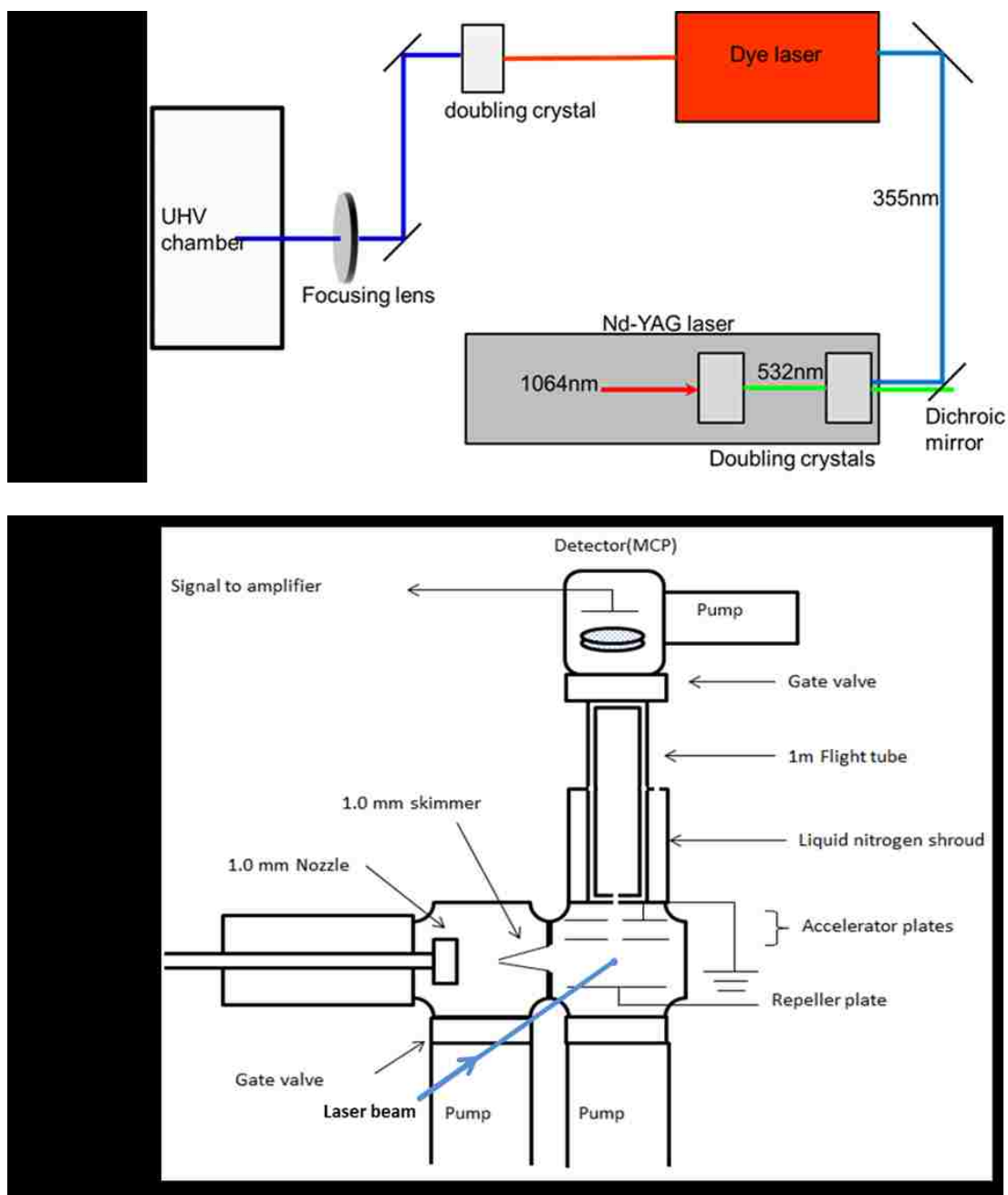


**Figure 6:** (a) Experimental setup showing the laser beam path into the vacuum chamber. (b) Schematic experimental setup used for REMPI the experiments.



## 2.4 COMPUTATIONAL DETAILS FOR BROMOBENZENE CLUSTERS

In this work, to investigate the existence of multiple conformations for each given cluster, *ab initio* calculations were carried out using Gaussian 09 package.<sup>103</sup> The full geometry optimization calculations were carried out from a variety of initial geometries which includes pi-stacked, C-H/pi, and halogen bonding using DFT method, M062x, with an aug-cc-pVDZ basis set. However, MP2 method was also used for comparison sake but M062x gave better results. All the geometry optimization calculations were done using the aug-cc-pVDZ basis set. Zhao and coworkers<sup>71</sup> demonstrated that M062x performs well in describing  $\pi$ -stacking systems and non-covalent interactions in general. Time depended-density functional theory (TD-DFT) calculations were carried out at TDM062x/aug-cc-pVTZ level in order to calculate the electronic spectra of the clusters and the optimized geometry of the  $S_1$  states. Methods employed included the range-separated hybrid functional  $\omega$ B97X-D,<sup>104</sup> the meta-GGA hybrid functionals M06 and M06-2X, and CAMB3LYP,<sup>71, 105</sup> all with an aug-cc-pVDZ basis set. A meta-GGA functional uses the Laplacian (second derivative) of the density or the kinetic energy density in addition to the density and the magnitude of the gradient of the density.<sup>106</sup> The performance of the  $\omega$ B97X-D and M06-2X methods for electronic excitations, including Rydberg and Charge Transfer excitations, have recently been benchmarked.<sup>70</sup> The calculated binding energies were corrected for zero point energy (ZPE), with the counterpoise method used to correct for basis set superposition error (BSSE).

## 2.5 BROMOBENZENE DIMER CONFORMATIONS

DFT calculations were carried out at the M06-2X/aug-cc-pVDZ level. The starting structures in the geometry optimizations were from random geometries that corresponded to  $\pi$ -stacked, C–H/ $\pi$ , and halogen–bonded structures. More than 10 dimer conformations were found and listed in Figure 7 are just seven representatives. The calculated binding energies are counterpoise and ZPE corrected. Dimers 1 through to dimer 3 are  $\pi$ -stacked dimers. The first dimer (Dimer 1) has an anti-parallel – displaced  $\pi$ - $\pi$  interaction between the aromatic rings. This geometry is more stable than a sandwich stacking configuration because it maximizes electrostatic attractions. Dimer 2 and dimer 3 are all stacked configurations that converged to minima with the second halogen atom at different positions relative to the other ring and its halogen atom. The planes of the two monomers are separated by  $\sim 3.3$  Å, and the two Br atoms are not in close van der Waals contact. The current results are consistent with similar studies that showed that  $\pi$ -stacked dimers are approximately isoenergetic.<sup>5, 12, 47, 87, 88</sup> Work on chlorobenzene has shown that the average binding energy in chlorobenzene stacked dimer is around 20kJ/mol. D4 is a T-shaped isomer reflecting interactions of the C–H groups of one monomer with the  $\pi$ -system and Br atom of the other, and this dimer has a calculated binding energy roughly one-half that of the  $\pi$ -stacked isomers. Structures like D1-D4 were found in chlorobenzene, and a key difference is the existence of the halogen bonded structures D5–D7. Here, D5 and D7 correspond to above-atom and above-bond structures, respectively, where the  $\sigma$ -hole of the Br atom of one monomer interacts with the  $\pi$ -system of the other. These exhibit binding energies similar to that of D4.

Finally, D6 corresponds to a side-on interaction of the 2 Br atoms, this dimer exhibits the weakest binding (4 kJ/mol). In prior studies of chlorobenzene dimers,<sup>88</sup> the M06-2X/aug-cc-pVDZ binding energies were overestimated with respect to high level single reference ab initio benchmarks, which in turn were in good agreement with available experimental data. A counterpoise corrected CCSD- (T)//M06-2X/aug-cc-pVDZ calculation of representative  $\pi$ -stacked (D3) and halogen bonded (D5) using ZPE corrections at the M06-2X/aug-cc-pVDZ level yielded a binding energy of 17 kJ/mol and 5.5 kJ/mol respectively, indicating that the M06-2X binding energies are too large by approximately 22%. To compare among different DFT methods, calculations on a representative dimer, D3, were carried out at the B97D and M05-2X levels of theory, which were previously benchmarked for similar systems.<sup>107</sup>

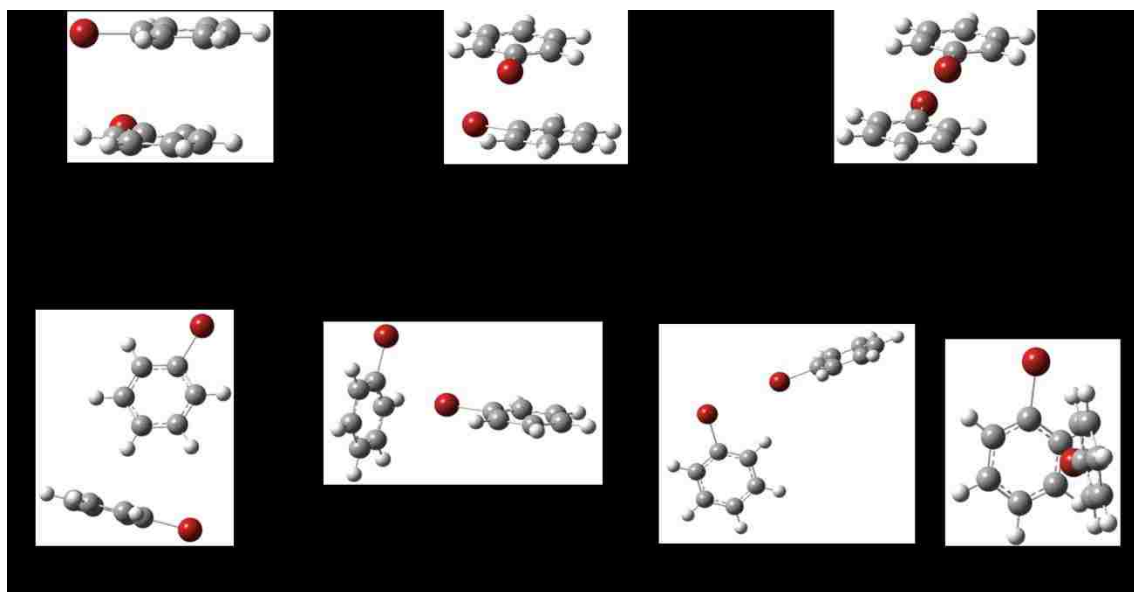


**Figure 7:** Bromobenzene dimer conformations and their respective binding energies calculated at M06-2X/aug-cc-pVDZ.

## 2.6 R2PI SPECTRA OF BROMOBENZENE DIMER

A linear time of flight mass spectrum for bromobenzene shown in Figure 8 was obtained under the experimental conditions described earlier. The natural isotopic abundance ratio of  $^{79}\text{Br}$  and  $^{81}\text{Br}$  is approximately 1:1, this is reflected in the integrated ion mass intensities as shown on Figure 8. The non-covalent dimer complexes formed in the supersonic molecular beam are also dominant in the mass spectrum which was taken at the dimer resonance. Figure 9 is the R2PI spectrum of bromobenzene, the origin band  $S_0-S_1$  ( $\pi \pi^*$ ) transition at  $37008 \text{ cm}^{-1}$  dominates the spectrum as well as the ring breathing mode  $6b(b_2)$ . Other vibronic bands are also prominent relative to the origin band. The spectroscopy of the bromobenzene monomer spectrum has been studied before,<sup>78, 80, 81</sup> hence it is not given much detailed discussion in this document. Figure 10 shows the mass selected resonant two photon ionization (R2PI) spectra of bromobenzene dimer complex. The dimer is clearly much broader and red shifted with respect to the monomer origin band  $S_0-S_1$  ( $\pi \pi^*$ ) transition, peaking around  $36953 \text{ cm}^{-1}$ , indicating a  $55 \text{ cm}^{-1}$  red shift. Another small shoulder is blue shifted by about  $36 \text{ cm}^{-1}$ . A closely related earlier study also observed this general broadness on chlorobenzene dimer and other higher order clusters up to the pentamer. Figure 11 displays these chlorobenzene clusters. This finding is similar to that observed for toluene and fluorobenzene.<sup>47, 85, 87</sup> Another obvious feature about the clusters is their similar profile and regions of absorption.

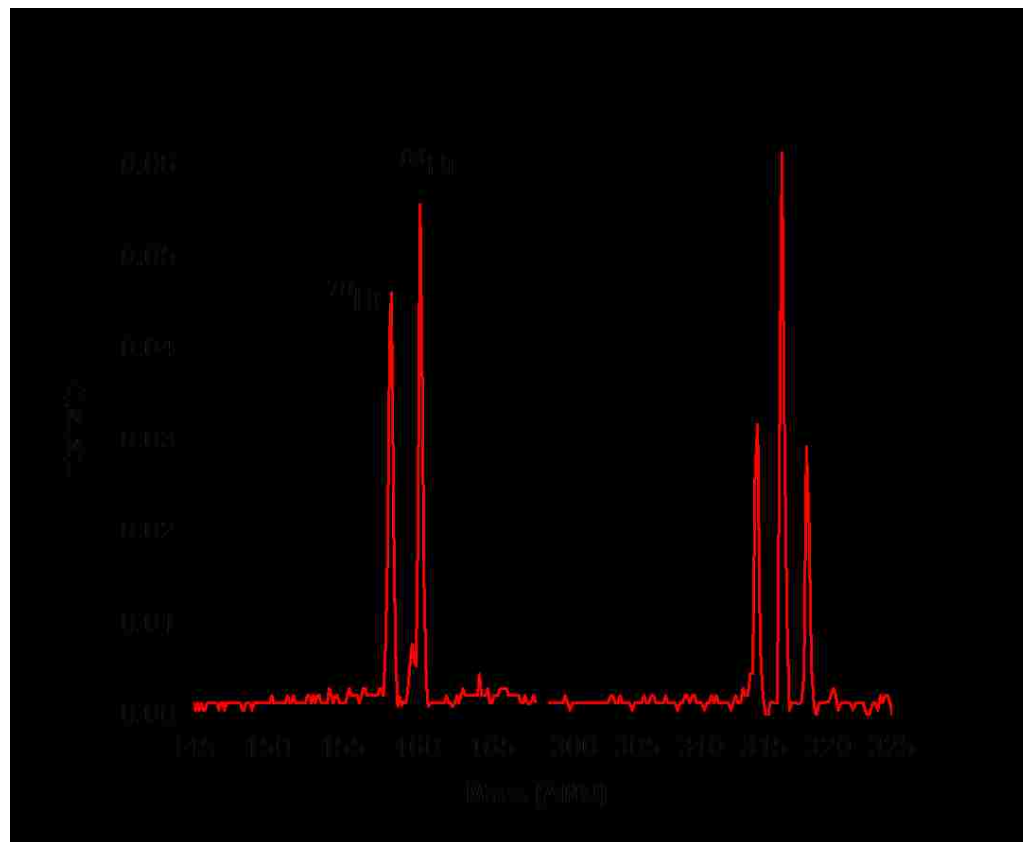


**Figure 8:** R2PI mass spectrum of bromobenzene. The two different Br isotope monomer units are well resolved as well as their dimer combinations.

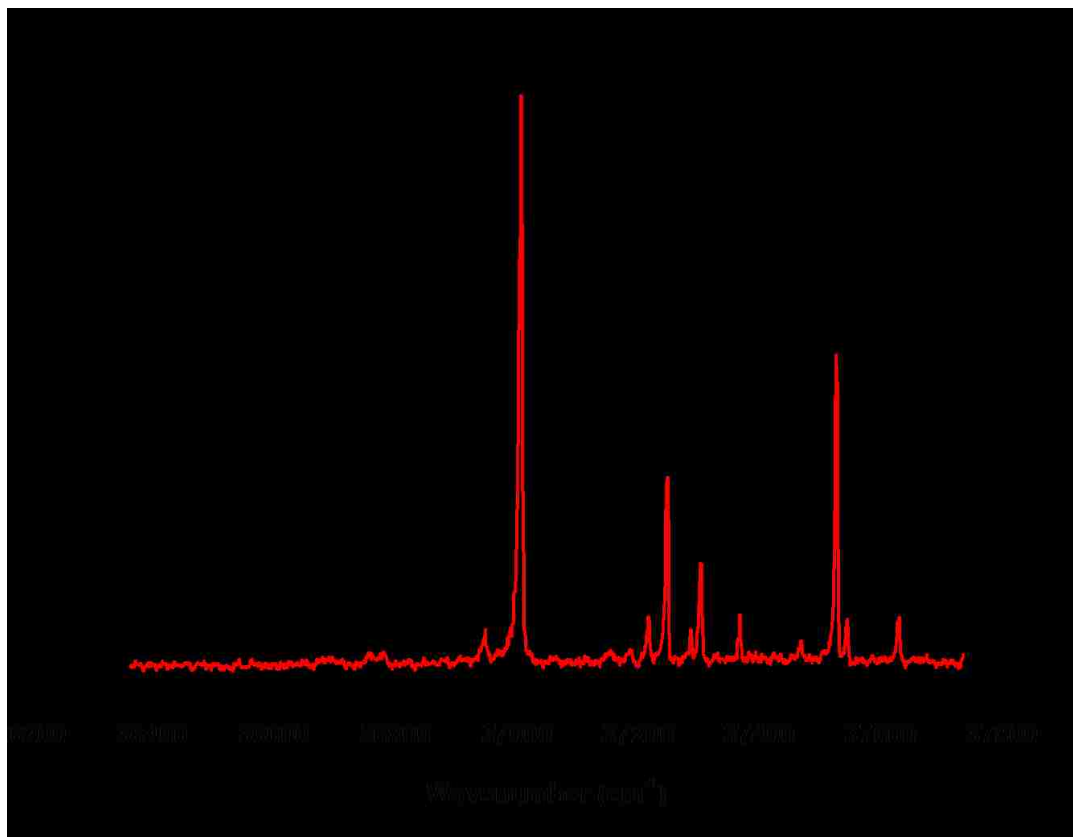


**Figure 9:** R2PI spectra of mass selected bromobenzene monomer. The origin band is at  $37008 \text{ cm}^{-1}$ . Vibrational mode assignments taken from reference.<sup>78</sup>

In bromobenzene clusters, there are a number of reasons to account for the broadness of these spectra. From ab initio calculations, it can be seen that there is more than one possible configuration for each cluster that are nearly iso-energetic. It is also highly possible that all these configurations are formed and detected from the molecular beam. Musgrave and coworkers proposed a similar hypothesis after doing some hole-burning experiments on toluene clusters, they observed that they were different conformations present.<sup>14</sup>

The broadness in the spectra for higher order clusters might also be due to unresolved vibrational structure in Franck–Condon active modes and transitions out of very low frequency torsional modes in the clusters, or “hot band” transitions. Other contributing factors should include the presence of multiple isotopomers ( $^{79}\text{Br}$ ,  $^{81}\text{Br}$ ). It can also be realized that the higher order clusters have a Gaussian line-shape that might be associated with inhomogeneous broadening. This inhomogeneous broadening can emanate from unresolved weak intermolecular vibronic bands and the presence of overlapping transitions of different isomers.<sup>14</sup> Cracking of larger clusters into other mass channels has been seen before to cause spectral broadening. To investigate this idea, the backing pressure was systematically varied, it was shown by Musgrave and coworkers<sup>14</sup> to be a critical factor in the formation of higher order clusters. This was done in a number of ways that includes operating at lower backing pressure, lower seeding ratios and bath temperature. After making sure all the higher order signals have been eliminated, a dimer scan was obtained that still resembles the broad absorption as shown in Figure 12. The conclusion drawn from this is that the broadness has nothing to do with contamination from the trimer or higher order clusters in general.

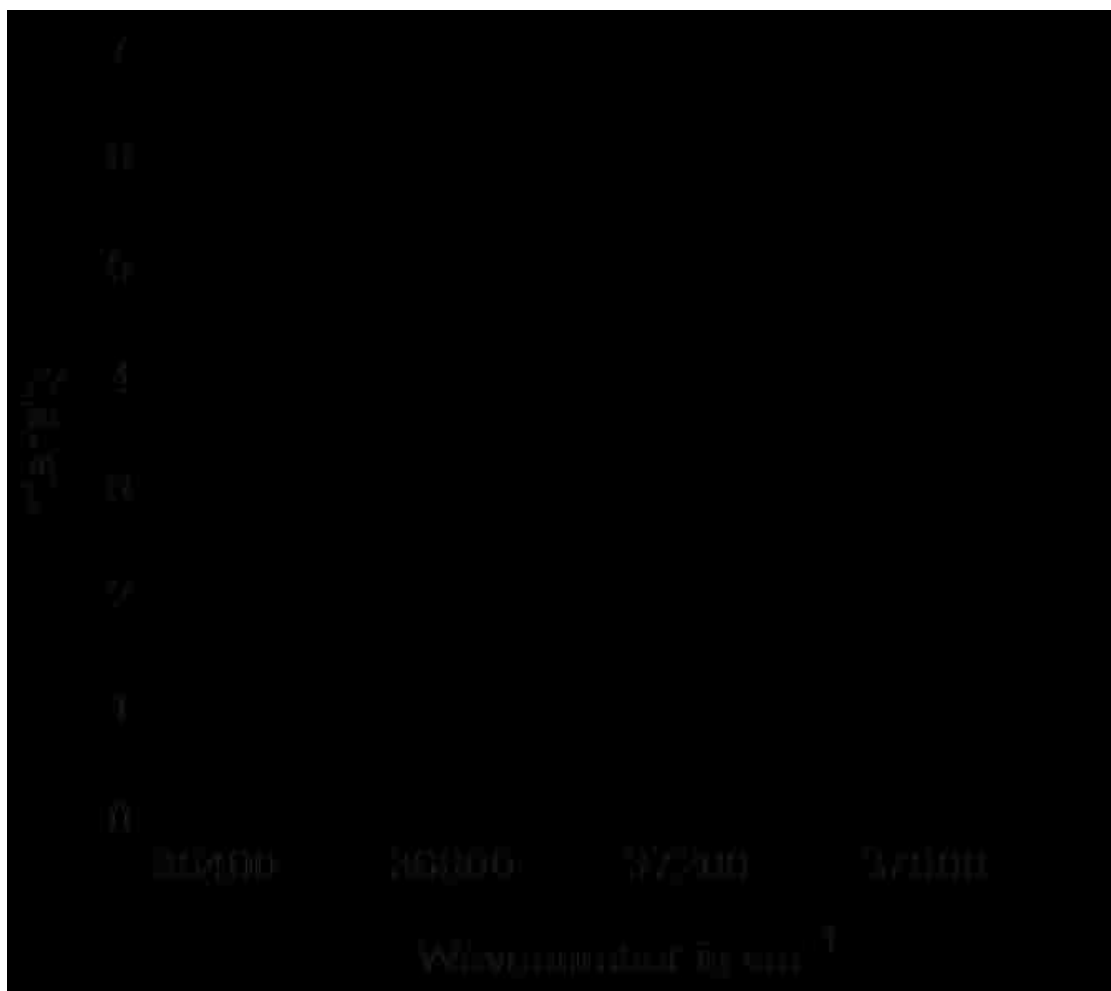


**Figure 10:** Resonant two-photon ionization (R2PI) spectra of mass selected bromobenzene dimer in the region of the origin band of the  $S_0$ - $S_1$  ( $\pi$ - $\pi$ ) transition of the monomer.



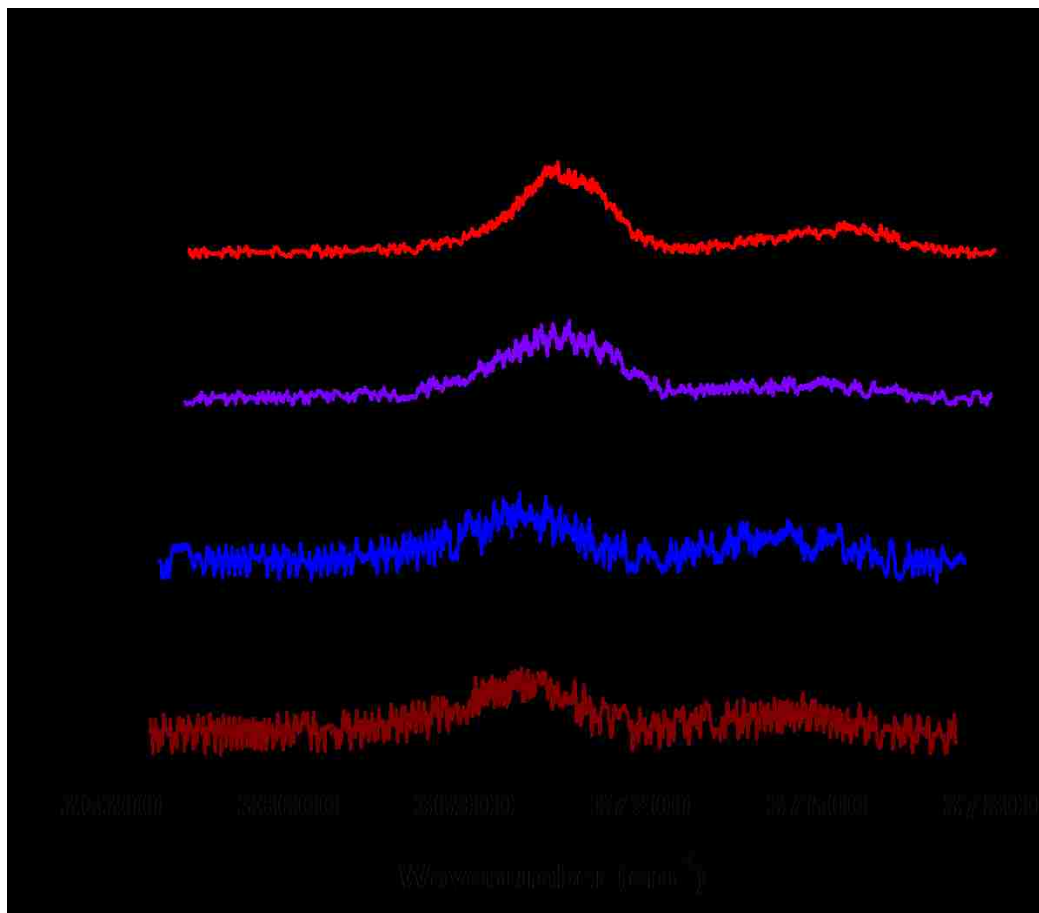


**Figure 11:** R2PI spectra of mass selected chlorobenzene monomer ( $n=1$ ) and clusters  $(\text{Chlbz})_n$  where  $n=2-5$ . The general trend of broadness was observed, a sign of possible presence of multiple isomers.

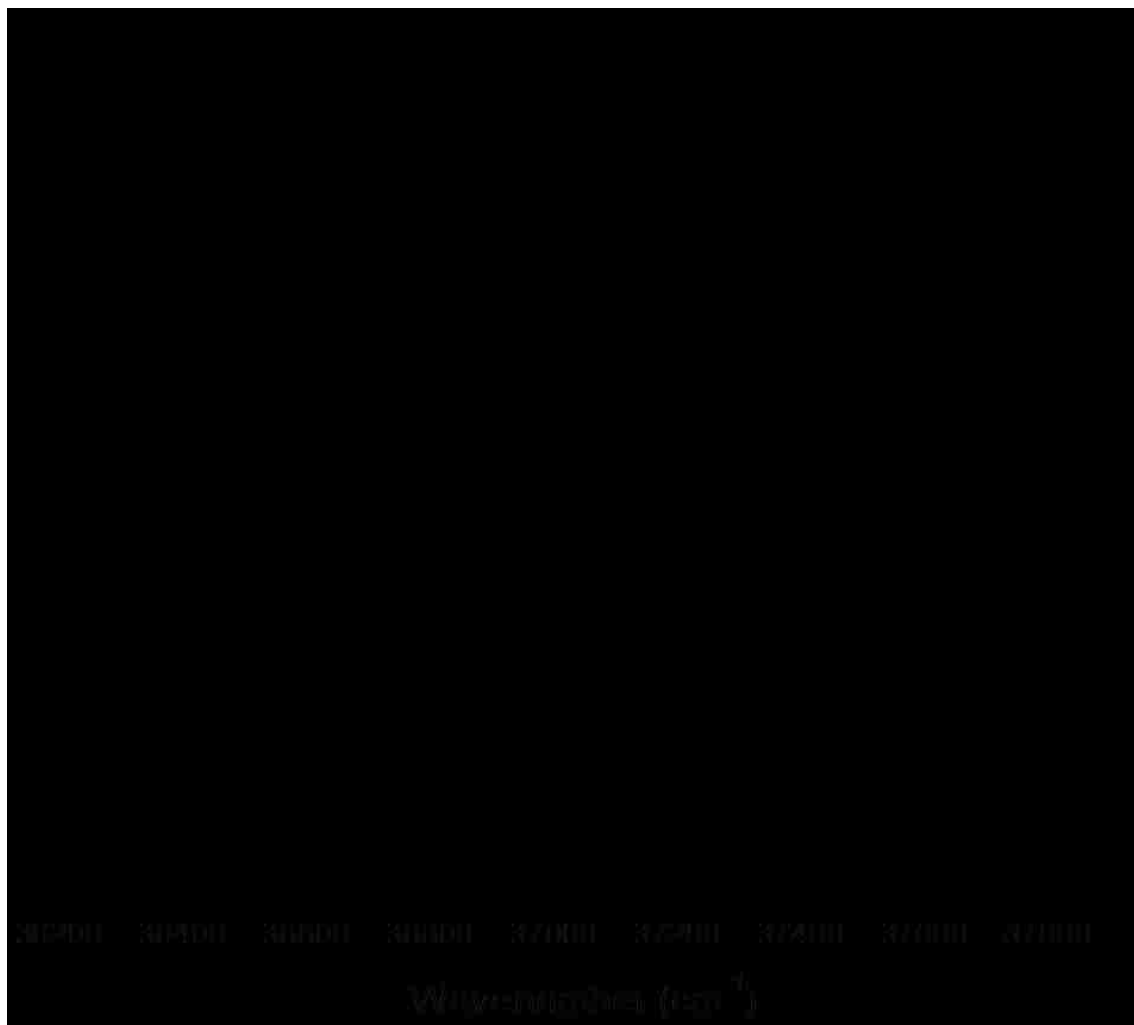


**Figure 12:** The R2PI spectra of bromobenzene dimer. Spectrum (1) recorded under optimum conditions for the dimer formation as well as any other higher order cluster. Spectrum (2) was taken under experimental conditions that were free from higher order clusters.

## 2.7 TD-DFT CALCULATIONS

Representative calculated TDDFT (TDCAM-B3LYP/aug-cc- pVDZ) spectra of the bromobenzene dimers D1–D6 and monomer are shown in Figure 13. The TDDFT spectra are shown as stick spectra, and the calculated energies have been scaled by 0.86 scaling factor in order to match the experimental energy of the  $S_0$ - $S_1$  transition energy of the monomer.

From the TDDFT calculations of the dimer spectra, two absorptions for each conformation can be seen; this is attributed to the presence of two chromophore monomer units. The size of the splitting (exciton) between the two absorptions heavily depends on the orientation of the monomer units in relation to another. In exciton splitting theory, if the two monomers are orthogonal, their transition dipoles do not interact and no splitting is observed. Any other orientation will result in addition or subtraction of the transition dipole moments. A small absorption and a bigger absorption band may result as in the case of D3, the para dimer. Taking this into account for all possible dimers in the molecular beam, it's not surprising to observe a broad spectrum over this region as the splitting is not well resolved. In all dimers except D6, the calculated electron transitions are predicted to lie to lower energy as compared to the monomer absorption. The calculated absorptions of various isomers occur over a range that, when scaled, is roughly similar to that observed experimentally as indicated in Figure 14.

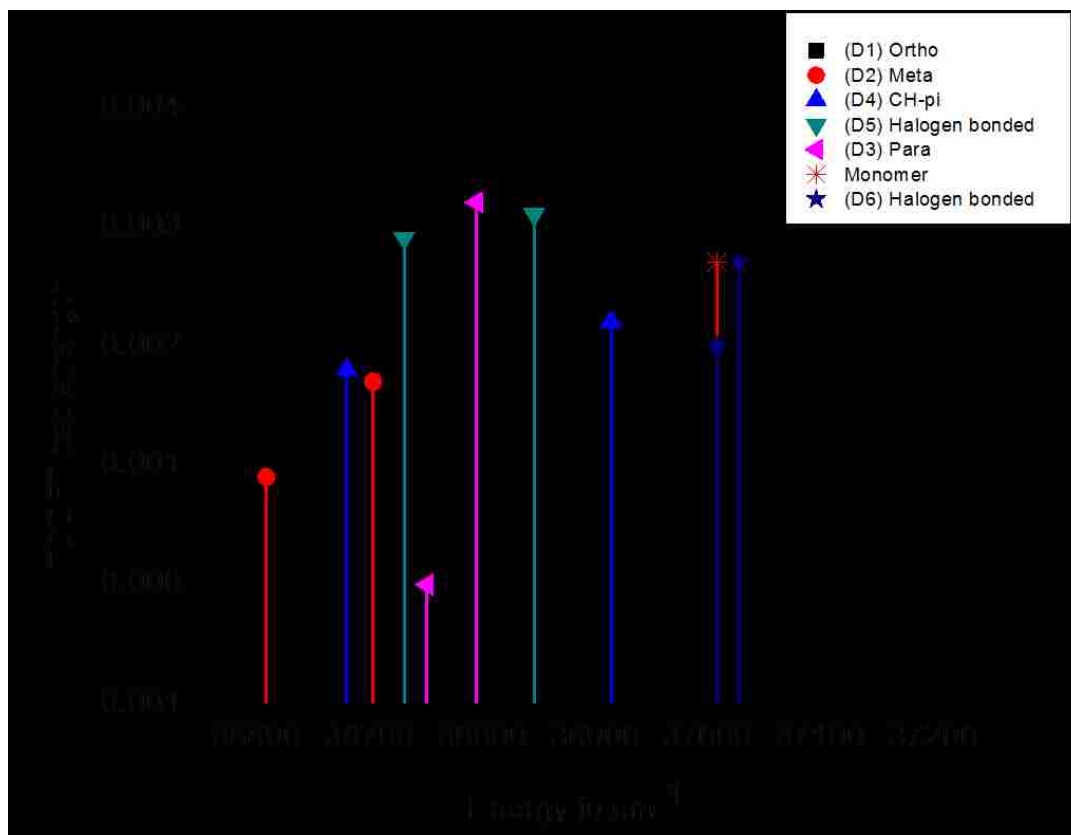


**Figure 13:** Representative calculated TDDFT (TDCAM-B3LYP/aug-cc- pVDZ) spectra of the bromobenzene dimers D1–D6. The calculated energy has been scaled and referenced to the observed position of the origin band of the monomer.

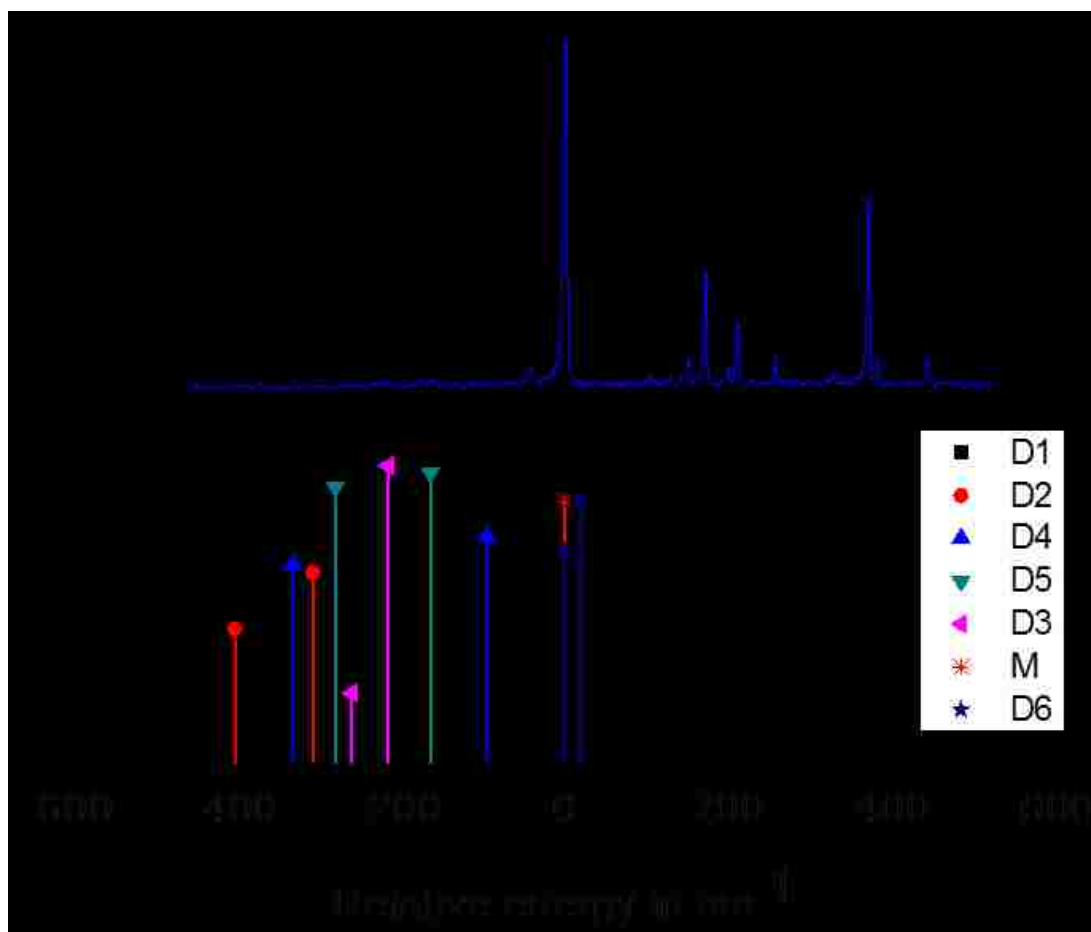


**Figure 14:** Calculated TDDFT (TDCAM-B3LYP)/aug-cc-pVDZ) spectra of the bromobenzene dimers. The calculated energy has been scaled and referenced to the observed position of the origin band of the monomer.

The broadened spectra could also be due to Franck–Condon (FC) activity in the low frequency intermolecular vibrational modes. FC activity is typically expected in these types of clusters, it was found to be playing a role in a similar system of chlorobenzene. If these low frequency modes are not resolved, it results in a broad feature that is difficult to characterize. The optimized structures of the lowest lying excited electronic state of dimers D3, D4 and D6 at the TDM06-2X/aug-ccpVDZ level are shown in Figure 15.

For dimer D3, as was seen for a similar in PhCl system, upon electronic transition to the  $\pi^*$  orbital, the isomer undergoes a change in geometry from a parallel slipped to a sandwich structure, in which the two monomers are directly on top of each other. The intermolecular separation also drops in the process to  $\sim 3.0$  Å. This is also noticed in similar systems involving homo aromatic dimer species.<sup>108, 109</sup> From Figure 15, D3 and D4 undergoes a big change in geometry whilst D6 undergoes a small change in geometry. The electronic transition has two different effects on the dimers, for D6, it actually weakens the halogen bond, hence it blue shifts whilst for D3 and D4 the transition stabilizes the excited state more, hence it red shifts.

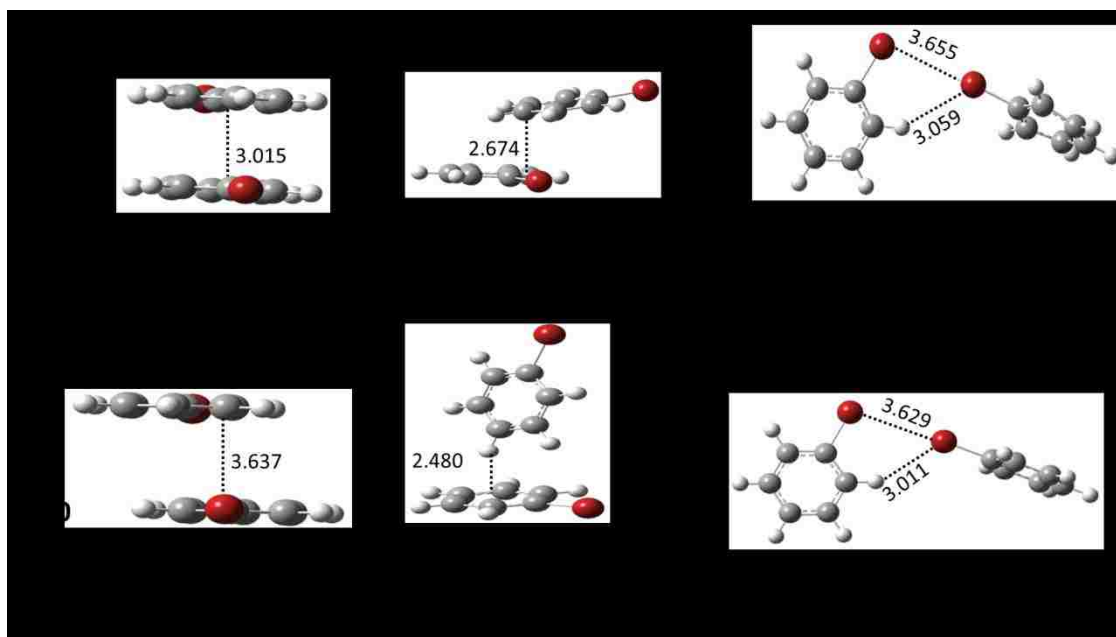


**Figure 15:** Optimized structures of dimers D3, D4 and D6 in the  $S_0$  and  $S_1$  states, obtained from TDM06-2X/aug-cc-pVDZ calculations.

## 2.8 MIXED DIMERS: R2PI SPECTRA OF BROMOBENZENE-BENZENE DIMER

The bromobenzene-benzene system was also studied here in order to see if the trend observed in bromobenzene remains the same. The experimental setup is similar to the one described before for bromobenzene experiment. In this experiment the bromobenzene and benzene precursor were mixed together in the bubbler in a 1:1 mixing ratio. The conditions for the formation of the mixed dimer did not vary much from those of the homo-dimer. The 1+1 R2PI spectrum of the mixed dimer and trimer,  $\text{PhBr}\cdots(\text{Bz})_2$  are shown in Figure 16. In comparison with the PhBr homodimer, the mixed bromobenzene–benzene ( $\text{PhBr}\cdots\text{Bz}$ ) dimer displays a broadened feature that is slightly blue-shifted with respect to the monomer origin band. A closer look at the spectrum, one can see some unresolved vibrational structure.



**Figure 16:** R2PI spectra of mass-selected (a) bromobenzene monomer and (b) mixed bromobenzene–benzene dimer and (c) trimer in the monomer  $S_0$ – $S_1$  transition region of the monomer.

Computationally, four minimum energy structures shown in Figure 17 were obtained. Figure 18 displays the calculated and scaled TDDFT spectra of these complexes at the TDCAMB3LYP/ aug-cc-pVDZ level. The most stable conformer in the mixed dimer system has been found to be the  $\pi$ -stacked (-16.7kJ/mol), with the CH/ $\pi$  and the C-Br/ $\pi$  having about half that binding energy. The noticeable difference between the homo dimer D3 and MD1 is in the binding energy, the binding energy of MD1 is decreased roughly 30% with respect to D3. This suggests that dipole–dipole coupling in these systems might be a significant factor in determining the preferred binding motif in halogenated halobenzene clusters. TDDFT vertical excitation energies shown were scaled with respect to the monomer origin band and as expected, the absorptions are red shifted as well.



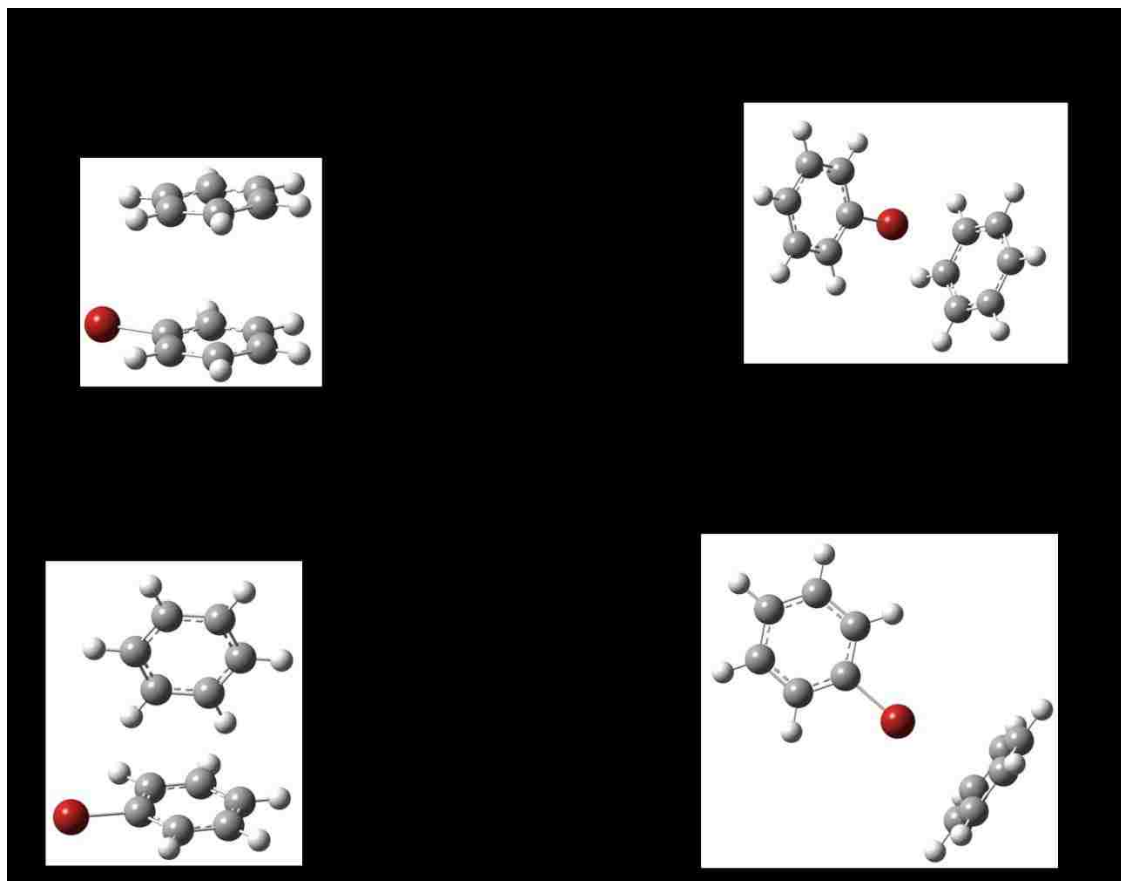


**Figure 17:** Optimized structures (MD1–MD4) and binding energy for the mixed bromobenzene–benzene dimer, calculated at the M06-2X/ aug-cc-pVDZ level of theory. The binding energies are counterpoise and ZPE corrected.

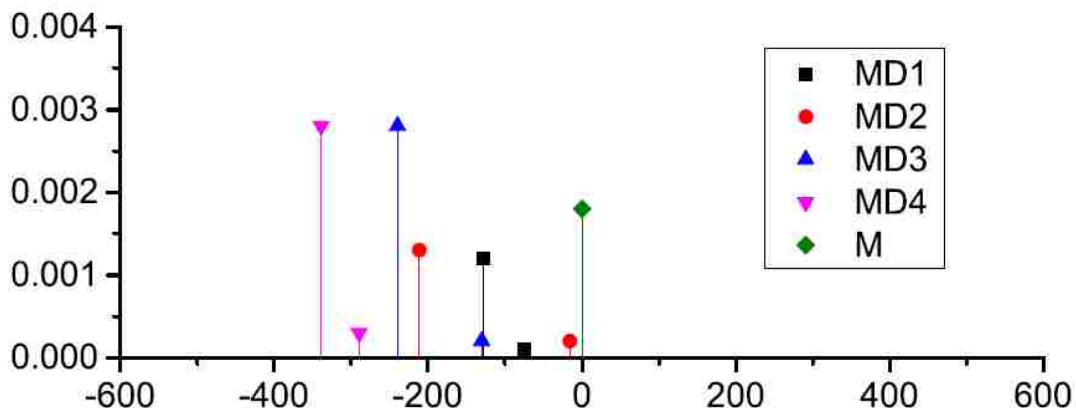


**Figure 18:** Calculated TDDFT (TDCAM-B3LYP/aug-cc-pVDZ) spectra of the mixed bromobenzene–benzene dimers. The calculated energy has been scaled and referenced to the observed position of the origin band of the monomer.

## 2.9 BROMOBENZENE TRIMER CONFORMATIONS

A total of 6 local minimum energy trimer structures were found at the M06-2x/aug-cc-pVTZ level and are shown in Figure 19. Again, these are the most probable trimer structures, there could be many more. The isomers presented here were obtained mainly by starting from a fully  $\pi$ -stacked structures with Cl atoms staggered. Trimer 2 (T2) and T6 are fully  $\pi$ -stacked. From the binding energies of chlorobenzene trimers, it was found that the fully  $\pi$ -stacked structures are most strongly bound ( $\sim 42.0$  kJ/mol). This binding energy roughly unchanged for bromobenzene  $\pi$ -stacked trimers, indicating that the nature of the halogen atom is not critical in the stabilization of the  $\pi$ -stacked conformations. The  $\pi$ -stacked trimer structure binding energy value is about twice the size of the binding energy of a stacked dimer ( $\sim 21.0$  kJ/mol).

Trimer configurations T1, T4 and T5 have a stacked dimer core, with the third monomer unit being flapped somewhere around this dimer core, in a T-shaped sort of attachment. The dimer core for T3 is a CH/  $\pi$  dimer. The energies of these trimers is about 2/3 that of  $\pi$ -stacked structures. Moving to the PhBr-(Bz)<sub>2</sub> mixed trimer, the R2PI spectrum shown in Figure 20 was obtained, and again, it is broad and red shifted compared to the monomer absorption, and similar to the spectrum of the dimer. For representative mixed trimers MT1 (29.5kJ/mol) and MT2 (24.0 kJ/mol) the binding energies relatively lower than the corresponding homogenous trimers. MT1 is the global minimum structure for the mixed trimers, its binding energy is reduced by  $\sim$ 30% relative to the corresponding global minimum PhBr trimer (T2) structure. This trend was also noticed between PhBr dimers and PhBr mixed dimers, the presence of a dipole-dipole coupling within the molecular cluster has got a stabilization effect. Their R2PI spectra is also as broad as the homogenous trimers but with visible vibrational structure and a better noise to signal ratio.

The TDDFT calculated spectra of the trimers show three absorptions split by an exciton splitting that is also isomer dependent in Figure 21. The intensity ratio of the splits is roughly 3:2:1, with the the smallest absorption having no meaningful oscillator strength. All the trimers have been predicted to be red shifted with respect to the bromobenzene monomer origin transition. The range over which these electronic transitions occur is similar to that observed for the dimers and the profile of the experimental spectra is also similar even though the noise to signal ratio of the trimers is higher.

This similarity of the dimer and trimer spectra can also be explained by the presence of multiple isomers, whose electronic spectra span a similar range as the dimers. Related studies on toluene observed a similar trend of broad spectra of higher order clusters about the monomer origin transition.<sup>14</sup> They proposed that the favored binding motif of the dimer -  $\pi$ -stacked structure, formed a core chromophore in higher order clusters, resulting in a  $\pi$ -stacked dimer core based absorption. It could be true that all the optimized trimer structures could be present in the molecular beam, including the non-stacked structures, 'hole burning' experiments may shade more light on which conformations are most important and their respective absorption regions.

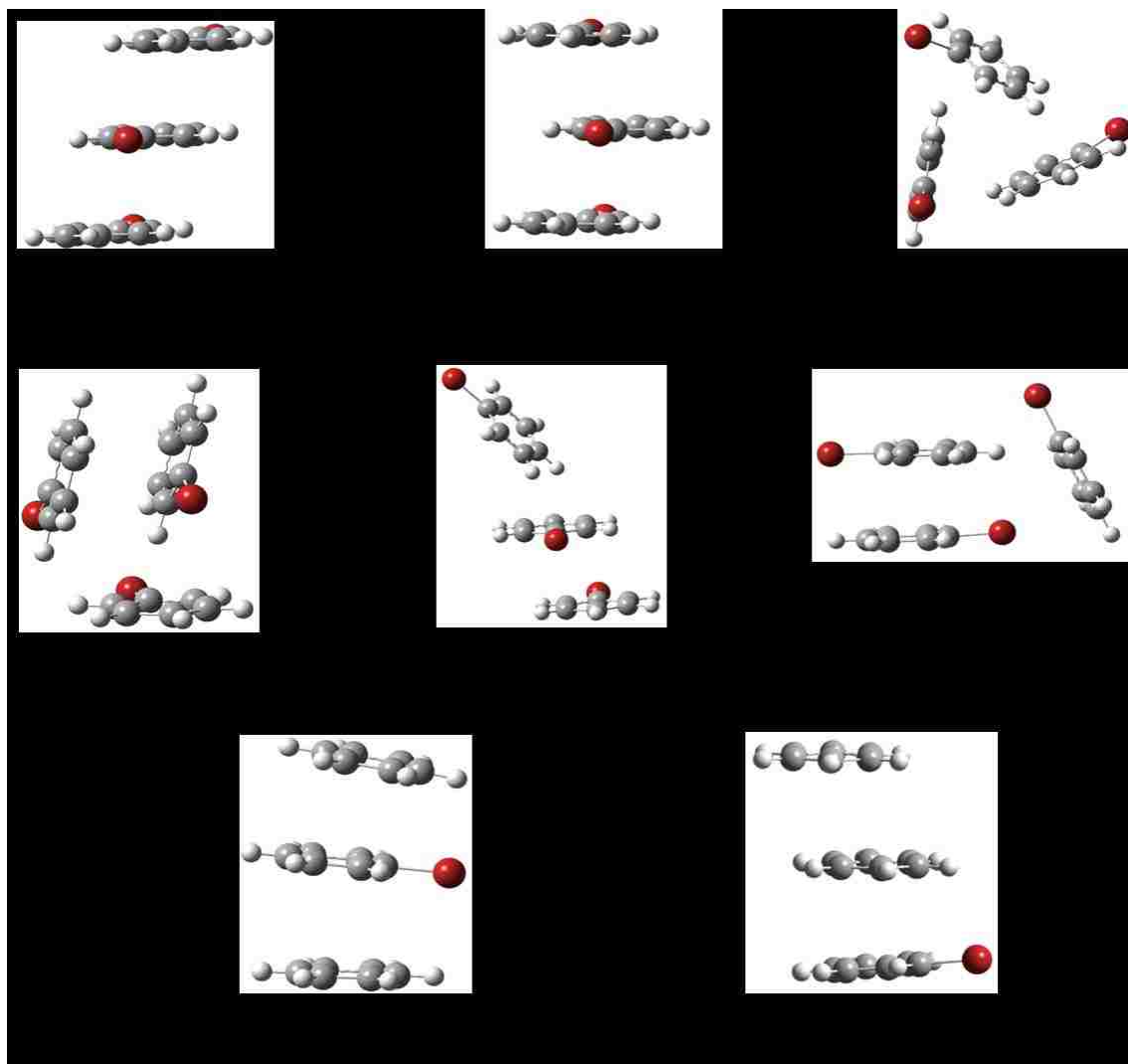


**Figure 19:** Optimized bromobenzene trimer structures (T1–T6) and mixed bromobenzene-benzene trimers and their corresponding binding energies(kJ/mol), calculated at the M06-2X/ aug-cc-pVDZ level of theory. The binding energies are counterpoise and ZPE corrected.

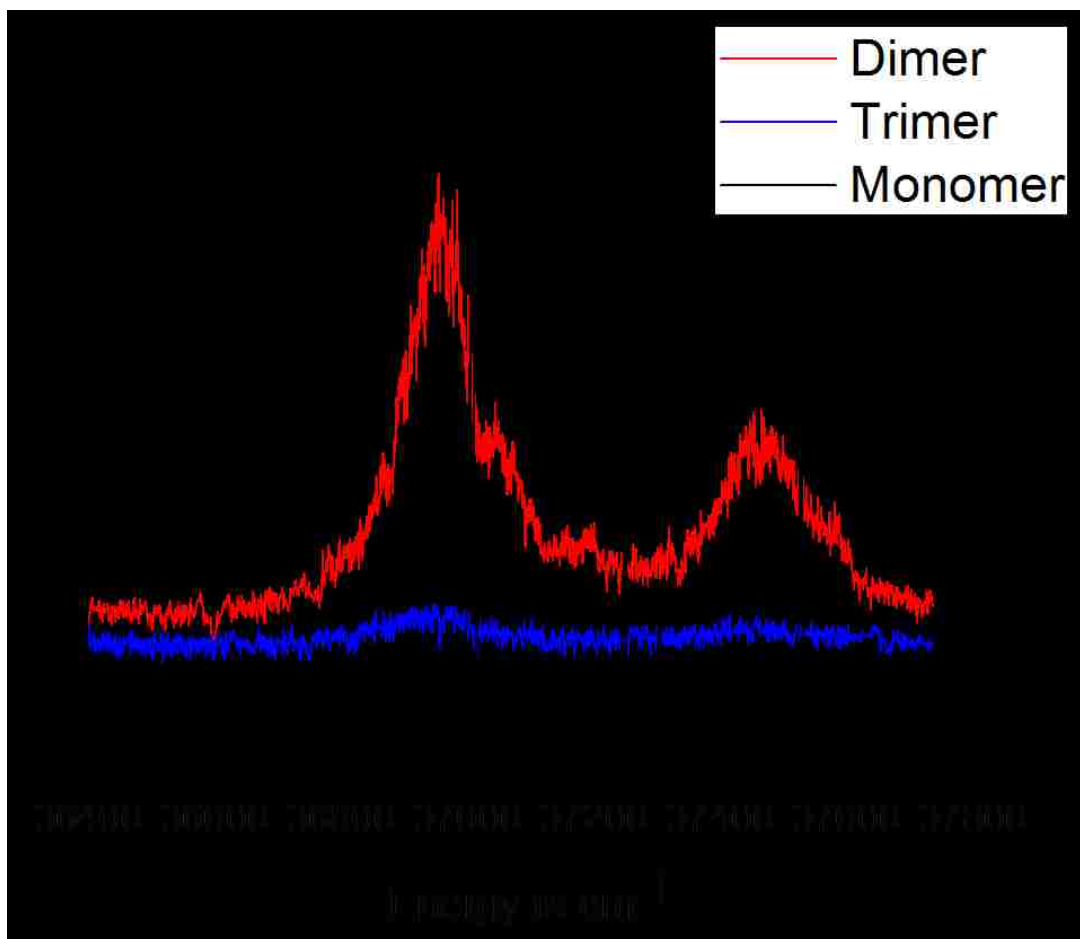


**Figure 20:** Resonant R2PI spectra of mass-selected bromobenzene monomer, trimer and mixed bromobenzene–benzene trimer in the region of the origin band of the  $S_0$ – $S_1$  ( $\pi\pi^*$ ) transition of the monomer.

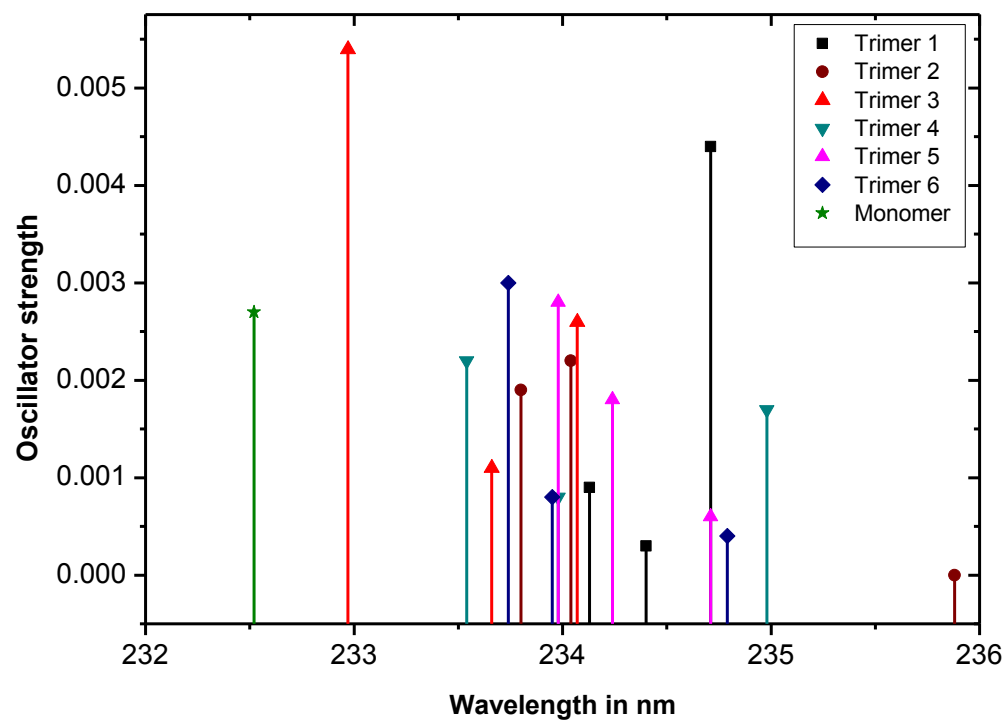


**Figure 21:** Calculated TDDFT (TDM06-2x/aug-cc-pVDZ) spectra of the bromobenzene trimers.

## 2.10 VALIDATION OF TDDFT CALCULATIONS

### 2.10.1 CHLOROBENZENE – AMMONIA VAN DER WAALS DIMER

As a way to show that the TDDFT calculations are within acceptable range of accuracy, a validation is being sort here using the work on chlorobenzene-ammonia non-covalent system,  $\text{PhCl}\cdots\text{NH}_3$ , this work is discussed in great detail in the publication.<sup>110</sup> From literature on the R2PI studies,  $\text{PhCl-NH}_3$  dimer complex is known to have a sharp origin band at  $37143\text{cm}^{-1}$ , and is blue shifted by  $76\text{ cm}^{-1}$  from the monomer origin.<sup>2, 111-</sup><sup>114</sup> In the study of the dimer complex, four minimum energy structures were found, of which two were out of plane  $\pi$ -type geometry and the other two were of in-plane  $\sigma$ -type geometry shown in Figure 22. TDDFT and multidimensional Frank-Condon simulations were used to assign the  $\sigma$ -type complexes (D3 and D4) as the ones responsible for the observed R2PI spectrum shown in Figure 23. The R2PI spectrum is dominated by the  $S_0$ - $S_1$  origin band and is blue shifted by about  $76\text{cm}^{-1}$ , in good agreement with literature. Scaled TDM06-2X calculations of the two possible  $\sigma$ -type complexes (D3 and D4), which cannot be distinguished on the basis of electronic spectroscopy, reproduce this blue shift to within  $10\text{ cm}^{-1}$ , as shown in Figure 24. This saves as a validation to the TDDFT calculations at the same level theory applied to the bromobenzene cluster system.



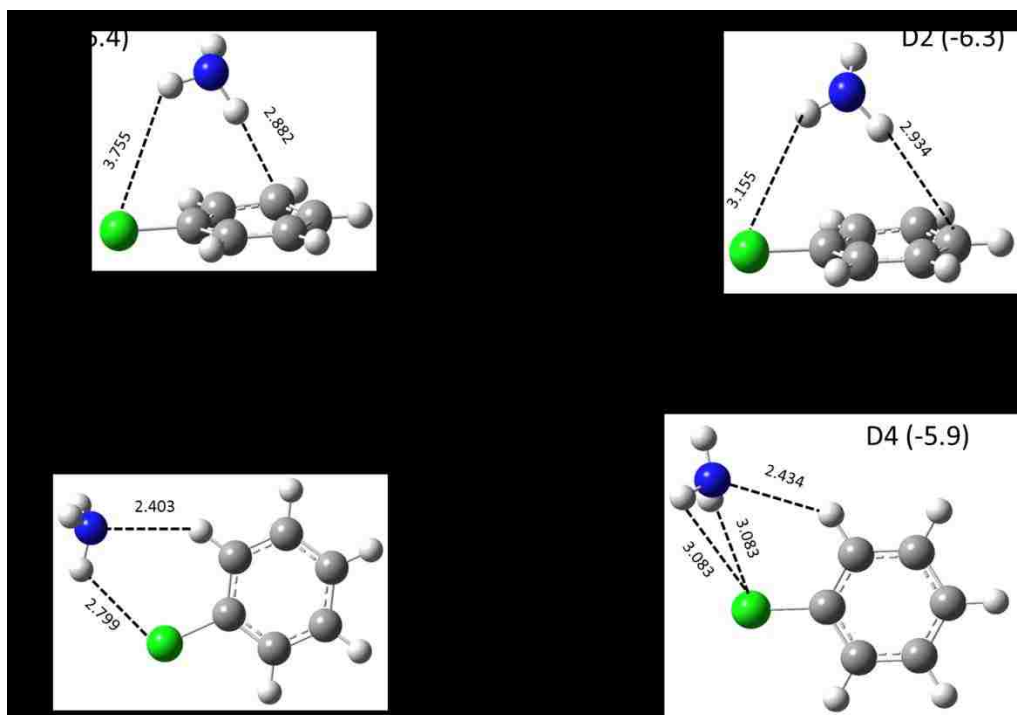


**Figure 22:** Optimized structures and binding energies (in parenthesis) of four minimum energy PhCl-NH<sub>3</sub> dimers structures (D1-D4) at M06-2X/aug-cc-pVDZ level.

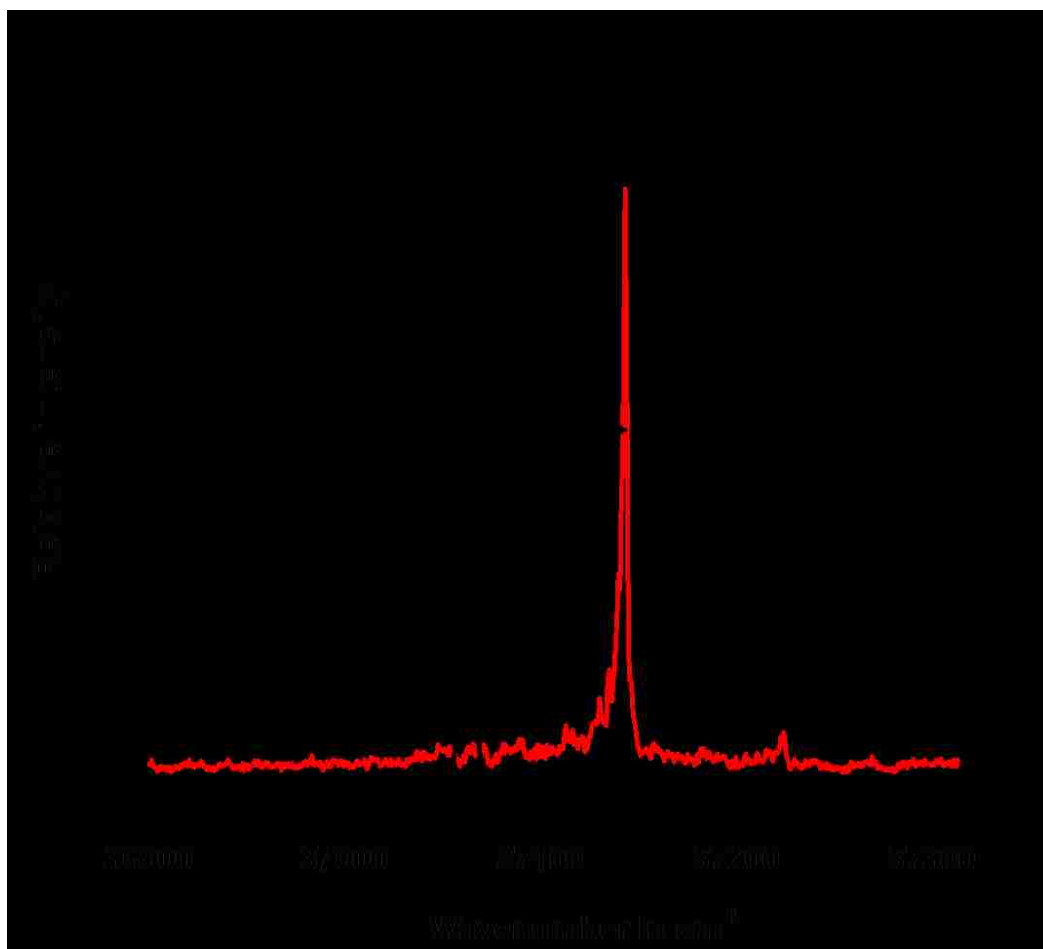


**Figure 23:** R2PI spectra of PhCl monomer and PhCl—NH<sub>3</sub> complex (measured in the protonated aniline mass channel due to the fast intracuster reaction upon ionization).

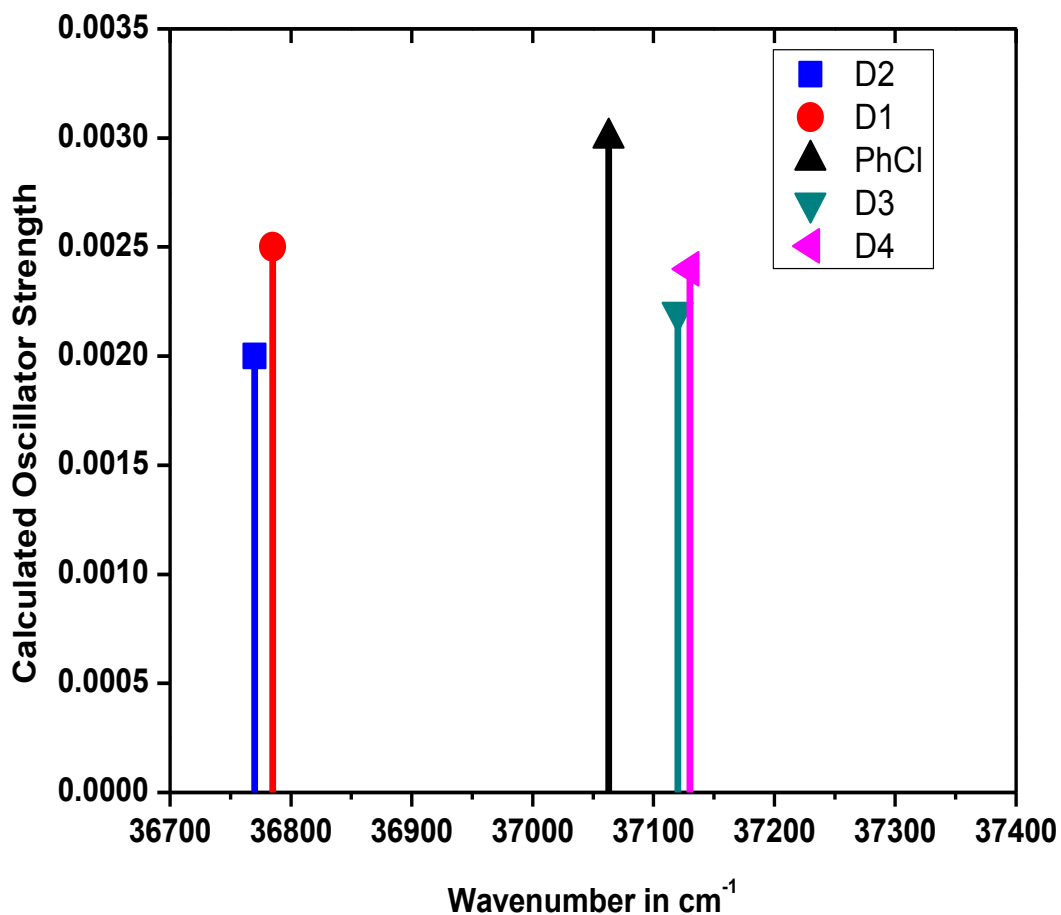


**Figure 24:** Predicted positions of the electronic origins of the PhCl monomer and two  $\sigma$ -type structures of the PhCl—NH<sub>3</sub> complex obtained from TDM06-2X/aug-cc-pVTZ calculations. The calculated transition energies have been scaled to match the experimental origin of the monomer.

## SUMMARY

In studying noncovalent interactions in order to understand their nature and strength, prototypical systems are employed in which these types of interaction may exist. An examination of the bromobenzene homoclusters and mixed bromobenzene–benzene clusters was done using R2PI spectroscopy in concert with electronic structure calculations.

In the bromobenzene dimer system, seven minimum energy structures were optimized; it should be stated that these are only representative structures since more conformers do exist. It was shown that three  $\pi$ -stacked structures, one T-shaped structure bound through CH/ $\pi$  interaction and three halogen bonded structures. The  $\pi$ -stacked structures are the most strongly bound (between  $-19$  and  $-21$  kJ/mol), and the halogen bonded isomers the weakest (between  $-4$  and  $-7$  kJ/mol). Calculated TDDFT spectra of these isomers show that these absorb over a range consistent with the breadth of the experimental spectrum, and with the exception of one halogen bonded dimer, the calculated absorptions are red-shifted with respect to the monomer transition.

Four minimum energy structures for the bromobenzene–benzene dimer were optimized computationally and the TDDFT spectra absorptions show a broad and unresolved vibronic structure around the origin band. This trend was also observed in bromobenzene dimer as well as similar systems studied before. Frank-Condon activity in the low frequency intermolecular mode has also been attributed to contribute to the broadness of the spectra. It was observed computationally that the  $\pi$ -stacked dimer conformations undergoes a significant change in geometry upon electronic transition into the  $\pi^*$  orbital leading to the rise of these weak intermolecular vibrational modes. These modes can easily congest a spectrum to make look like one broad absorption.

For the bromobenzene trimers, a total of six local minimum energy structures were optimized. As in chlorobenzene trimers, the fully  $\pi$ -stacked structures were the most bound with an average binding energy of  $\sim 43.0$  kJ/mol which is similar to that calculated for chlorobenzene trimers. This similarity indicates that the nature of the halogen atom is not critical in the stabilization of the  $\pi$ -stacked conformations.

The TDDFT calculated spectra of the trimers show three absorptions split by an exciton splitting that is also isomer dependent. All trimers were predicted to be red shifted with respect to the bromobenzene monomer origin transition. The R2PI spectrum of the trimer was also similar to that of the dimer, this could be due to the presence of multiple isomers, whose electronic spectra span a similar range as the dimers. Conducting ‘hole burning’ experiments may shade more light on which conformations are most important and their respective absorption regions.

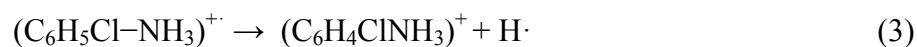
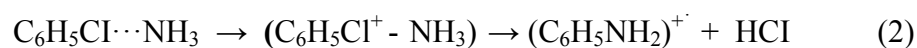
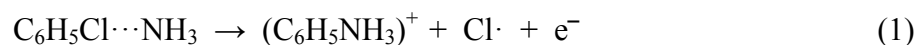
Future studies could include the study of halobenzene clusters with other donors including N atom and O atom donors. However, due to the difficulty in ionizing the halobenzenes as a result of the short  $S_1$  lifetime, using N atom and O atom containing chromophores such as aniline and phenol to further investigate halogen-bonding interactions will be more informative. Such an approach will greatly expand the range of systems that can be examined.

## CHAPTER 3. PhBr-NH<sub>3</sub> VAN DER WAALS DIMER

### 3.1 INTRODUCTION TO PhX-NH<sub>3</sub> VAN DER WAALS COMPLEXES

The growing interest on weak van der Waals interactions involving halogenated benzenes in molecular clusters has been driven by the key role they may play in several chemical and biochemical reactions.<sup>24, 25, 31, 32, 115-118</sup> These interactions include, amongst others, halogen bonding, hydrogen bonding,  $\pi$ - $\pi$  stacking, C-H/  $\pi$  and N-H/  $\pi$ . In solution, these interactions have been found to control the chemical and physical properties of molecular systems.<sup>34, 38, 113, 119</sup> Most of these weakly bound clusters involving halogenated benzenes in gas phase have been found to be prone to some kind of intra-cluster reaction, fragmentation or photodissociation. The literature on these halogenated benzene clusters with ammonia have generally shown that their photodissociation and subsequent intra-cluster reactivity upon ionization will produce products that may include phenyl cation, aniline cation, hydrogen halide or the anilinium cation and a halogen radical. These processes observed experimentally and computationally can actually reveal some characteristics of elementary processes occurring in their condensed phase, hence, their widely use as typical prototypes to study these interactions. In this study, both experiment and theory is employed to investigate the non-covalent interactions between bromobenzene and ammonia. This system has been experimentally elusive to many researchers interested in weakly bound cluster chemistry using photoionization techniques.

As highlighted earlier in Chapter 2, bromobenzene is very short lived in its  $S_1$  state (30 ps) and is prone to high spin orbit coupling with other repulsive states.<sup>82, 101</sup> However, there is a fair amount of work done on similar systems, in 1990, Maeyama and Mikami, using two-color mass-selected multiphoton ionization technique showed that the  $C_6H_5Cl \cdots NH_3$  van der Waals dimer undergoes a nucleophilic substitution ( $S_N$ ) reaction upon ionization resulting in the preferential generation of protonated aniline cation and a Cl-atom loss.<sup>4, 119, 120</sup> It was suggested that the chemical bond with  $NH_3$  is made as the Cl atom is kicked out from the aromatic ring. The other reaction pathway observed is the HCl loss.



In 2013, Reid and coworkers probed the reactive pathways in the chlorobenzene-ammonia dimer cation radical using R2PI and electronic structure calculations using DFT methods.<sup>110</sup> In addition to the two channels identified by Maeyama and Mikami, they observed a third channel involving a H-atom loss. Even though reaction 1 and 2 had been studied before, it wasn't made clear what kind and structure of the intermediate  $(C_6H_5NH_3)^+$  involved in these channels leading to the products. Reid et al suggested an ipso substituted Wheland intermediate linking two stationary points either side.

They also suggested a second ortho substituted Wheland intermediate for the H-atom loss channel. They also quantified the branching ratios of the two competing reactions 1 and 2 using microcanonical transition state theory to confirm the dominance of channel 1 to be about 85%.

Another area of concentration is the structure determination of the 1:1 halogenated benzene – ammonia dimer. The common type of geometry that has been obtained over the years for non-covalent dimer systems involving benzene, toluene, phenol, fluorobenzene, chlorobenzene, difluorobenzene are with water or ammonia has been the in-plane  $\sigma$ - type (the  $\text{NH}_3$  interacting with the aromatic molecule either through the formation of a conventional hydrogen bond with an electron-rich substituent at the aromatic ring) and the second is the out of plane  $\pi$  – type geometry (a hydrogen bond is established with the electron cloud of the aromatic molecule).<sup>121-123</sup> Halogen bonding in these systems is even weaker if present at all, and very difficult to characterize experimentally. In the computational and experimental study on fluorobenzene and chlorobenzene with ammonia, no halogen bonded structures were found. However, in this study of bromobenzene – ammonia, one in-plane structure was found with the N atom lone pair interacting with the sigma hole on the bromine atom. This is not surprising as the strength and size of the sigma hole to the covalently bonded halogen atom is expected to increase in the order  $\text{F} < \text{Cl} < \text{Br} < \text{I}$ . Ammonia can act as both proton donor and acceptor as far as its hydrogen bonding to the halobenzene is concerned.<sup>124</sup>

Finding these different dimer conformations using computational methods has been quite successful over the years and there is a fair amount of literature for fluorobenzene and chlorobenzene.<sup>110, 120, 125-128</sup>



However, determining the dimer conformation responsible for the experimental spectra has left a few open questions. To start with, Tonge and coworkers studied the PhF-NH<sub>3</sub> system using R2PI spectroscopy.<sup>128</sup> They obtained a two-color R2PI dimer spectrum that was dominated by the S<sub>1</sub> origin band that was blue shifted by 59 cm<sup>-1</sup> with respect to the PhF monomer S<sub>0</sub>-S<sub>1</sub>( $\pi, \pi^*$ ) transition band (37875cm<sup>-1</sup>). The conformational search they conducted at MP2/aug-cc-pVDZ found a mixture of  $\pi$ -type and  $\sigma$ -type conformers. In order to determine which conformer(s) they formed in their supersonic molecular beam, they went on to do multi-dimensional Frank-Condon simulation of the electronic spectra of the most stable  $\pi$ -type and the  $\sigma$ -type conformer. The  $\sigma$ -type simulated resembled that obtained experimentally, with a dominant origin band. The  $\pi$ -type simulated spectrum was congested with intermolecular vibrational bands, a big contrast to the experimental spectrum. The conclusion drawn from this is that the experimental spectrum of PhF-NH<sub>3</sub> derives from an in-plane  $\sigma$  bound structure in the neutral ground state rather than an N-H/ $\pi$  bound structure. Vaupel and coworkers studied various van der Waals dimer systems involving NH<sub>3</sub> and benzene, toluene, PhF, PhCl and para-difluorobenzene.<sup>125</sup> They employed one-color resonant two photon ionization (R2PI) and IR-vibrational predissociation spectroscopy (depletion spectroscopy) in the region of the N-H stretch and obtained the experimental NH stretching shifts of NH<sub>3</sub> upon its interaction with the various kinds of  $\pi$  systems. The experiments were complemented by ab initio calculations carried out at the second-order Møller-Plesset (MP2) level of theory. They compared experimental shifts from free NH<sub>3</sub> absorptions, assigned the out of plane  $\pi$  structures as the ones responsible for the experimental spectra.

Recently Reid and coworkers used one color R2PI technique in conjunction with DFT and post HF methods on the PhCl-NH<sub>3</sub> dimer.<sup>110</sup> They obtained essentially two out of plane  $\pi$ -type conformers and two in plane  $\sigma$ -type conformers, both types were nearly isoenergetic bound by on average, 6.0 kJ/mol. The experimental spectrum was blue shifted by 76 cm<sup>-1</sup> and TDDFT at M06-2X/aug-cc-pVDZ predicted the the  $\sigma$ -type dimers to be blue shifted by the same amount whilst the  $\pi$ -type dimers were predicted to be red shifted about 300 cm<sup>-1</sup>. On top of this evidence that the  $\sigma$ -type is the one formed in the molecular beam, the multi-dimensional Frank-Condon simulations also predicted the experimental spectrum to be  $\sigma$ -type. No halogen bonded structures were found in these studies. The desire to study halogen bonding prompted us to study the bromobenzene-ammonia system. The approach adopted here uses one-color R2PI spectroscopy and density functional theory calculations.

### 3.2 EXPERIMENTAL AND COMPUTATIONAL DETAILS

Bromobenzene vapor was seeded in 1-5 % ammonia in helium gas at 25°C. The backing pressure was varied between 20 - 60 psi. The rest of the experimental setup remains the same as the one detailed in Chapter 2 of this document. Density functional theory electronic structure and binding energy calculations were performed using M06-2X functionals with aug-cc-pVDZ basis set. A total of five minimum energy structures were optimized, shown in Figure 25. The binding energies are zero-point energy corrected and basis set superposition errors (BSSE) were corrected.

To predict the vertical excitation energies of the dimers, TDDFT (M06-2X/aug-cc-pVDZ) calculations were carried out. The excitation energies were all scaled (0.86 scaling factor) relative to the observed PhBr monomer origin band. R2PI excitation spectra were simulated by performing multidimensional Franck-Condon calculations carried out using Pgopher.

### 3.3 RESULTS AND ANALYSIS

#### 3.3.1 GEOMETRY OPTIMIZATIONS

Geometry optimizations found five minimum energy structures shown in Figure 25: Two are  $\sigma$ -type (D1, D2), two  $\pi$ -type (D4, D5) and a halogen bonded structure (D3). For D1, in which the lone pair on N interacts with the ortho H atom whilst another N-H $\cdots$ Br is established making the ammonia both a proton acceptor and donor in a C-H $\cdots$ N-H $\cdots$ Br-C binding motif. In D2, the ammonia acts as a donor making a double C-H $\cdots$ N-H binding motif with the meta and para positions. The halogen bonded complex has the lone pair on the N atom facing directly to the bromine sigma hole (C-Br $\cdots$ N). The  $\pi$ -type dimers (D4 and D5) look similar in structure with the exception that in D5, the ammonia molecule has been rotated about 180° and is facing the other side above the system to that of D4. Both dimers form a C-Br $\cdots$ H-N-H $\cdots$   $\pi$  binding motif. The calculated binding energies have D1, D4 and D5 being the most stable, they are bound by about 6.5 kJ/mol.

The halogen bonded dimer D3 and the in plane para dimer D2 are bound by about half the binding energy of the other dimers. The binding energies are very small and this presents experimental challenges in trying to form these complexes in a supersonic jet expansion and have them last long enough to be probed and detected.

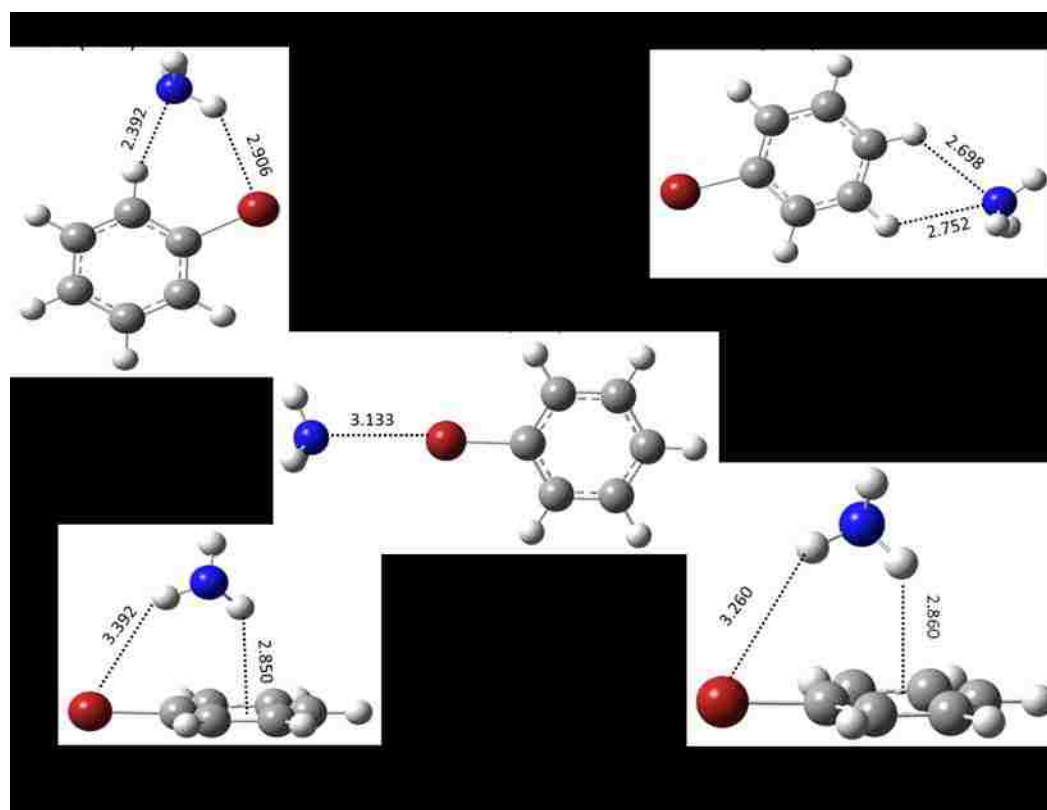


**Figure 25:** Ground state optimized geometries and binding energies (kJ/mol) for the PhBr-NH<sub>3</sub> 1:1 dimer.

### 3.3.2 R2PI SPECTRA AND REACTION PATHWAYS

Figure 26 shows the R2PI TOF mass spectra obtained for this system. The spectrum is heavily congested by daughter ion mass fragments from both the PhBr and the parent complex PhBr $\cdots$ NH<sub>3</sub>. The upper panel shows the full TOF mass spectrum and the bottom panel is a zoom-in in the region of interest. Ionic fragments observed include those with mass per charge ratio, m/z of 77, 93, 94, 156, 158, corresponding to the phenyl cation radical (C<sub>6</sub>H<sub>5</sub>)<sup>+</sup>, aniline cation radical (C<sub>6</sub>H<sub>5</sub>NH<sub>2</sub>)<sup>+</sup>, protonated aniline cation (C<sub>6</sub>H<sub>5</sub>NH<sub>3</sub>)<sup>+</sup>, bromobenzene cation radicals (C<sub>6</sub>H<sub>5</sub><sup>79</sup>Br)<sup>+</sup> and (C<sub>6</sub>H<sub>5</sub><sup>81</sup>Br)<sup>+</sup>. The mass spectrum also possesses other smaller mass peaks which did not hinder the mass selectivity of the peaks of interest as they were well resolved from one another. Under the conditions the spectra were taken, unfortunately no bromobenzene – ammonia van der Waals dimer was observed. There is a number of ways to explain the absence of the PhBr-NH<sub>3</sub>dimer mass peaks; as was noticed with the binding energies of these dimers (6.5kJ/mol), they are weakly bound, and the constituent monomer units can easily fly apart upon formation or probing by a laser pulse. It is also difficult to control complex formation; many undesired cluster combinations are formed in competition with the desired cluster size. However, by analyzing the mass spectrum and subsequent electronic spectra, one can actually deduce what is happening inside the ionization chamber. All daughter ion mass peaks could either be coming from fragmentation of parent molecules or parent molecular cluster or as products of a reaction between the species present at that particular moment. The species could still be neutral, ionic or radicals.

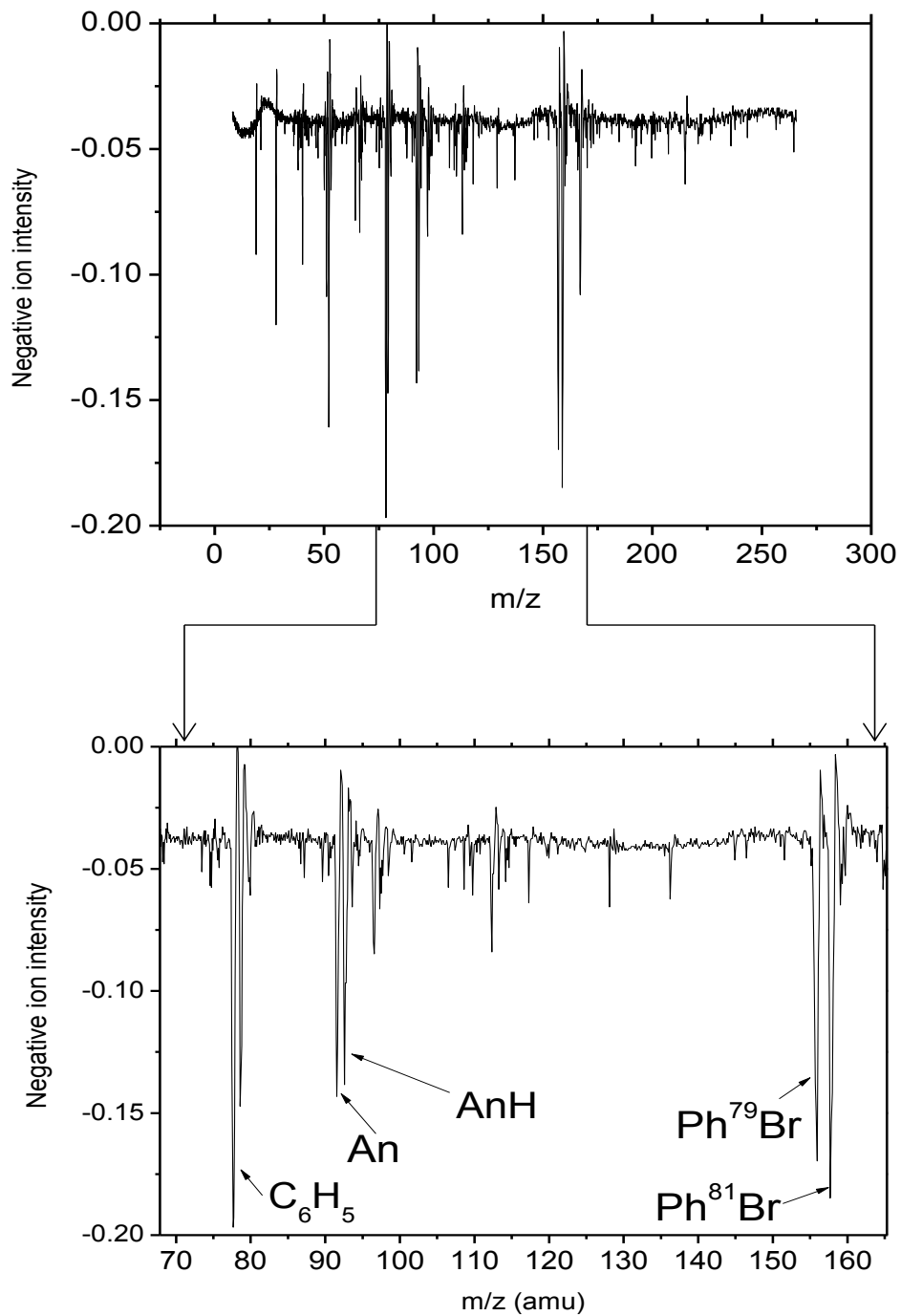


**Figure 26:** R2PI TOF mass spectrum for PhBr-NH<sub>3</sub> system. An=aniline, AnH=protonated aniline.



**Figure 27:** R2PI spectra of PhBr collected from the phenyl cation mass channel (top spectrum) and from the PhBr mass channel (bottom spectrum). The two spectra are identical, signifying a common source.

In order to characterize the daughter mass peaks and assign their source, each daughter peak scanned and a R2PI spectrum is obtained. Figure 27: shows a R2PI spectrum collected over the phenyl cation mass peak and it is overlaid with that of PhBr monomer. The two spectra are identical, implying that they come from the same precursor in the molecular beam, i.e bromobenzene. Bromobenzene is known to easily photodissociate upon ionization in its  $S_1$  state.<sup>82</sup> The photodissociation process leads to an alkyl/aryl radical and halogen atom elimination is found to be the dominant channel in the bromobenzene system and similar systems.

Equations 1-5 below help to understand how the observed daughter mass peaks came about. The first photon excites the PhBr or the neutral PhBr $\cdots$ NH<sub>3</sub> complex into S<sub>1</sub> state, the second photon ionizes the molecule/complex. An intracuster reaction may follow upon the ionization of the complex, leading to the formation of a cyclohexadienyl type intermediate, or Wheland intermediate. This Wheland intermediate has been frequently suggested in a number of aromatic substitution reactions, and its structure is a key to understanding the mechanism of aromatic substitution reactions.<sup>129</sup> From the Wheland intermediate, two competing reaction paths are possible; bromine atom loss and the HBr loss. In the HBr loss channel, the breaking away Br atom will supposedly have to form a four-center transition state bound by:



This four-center transition state was evidenced in the HCl loss channel for the PhCl system and was confirmed by intrinsic reaction coordinate calculations.



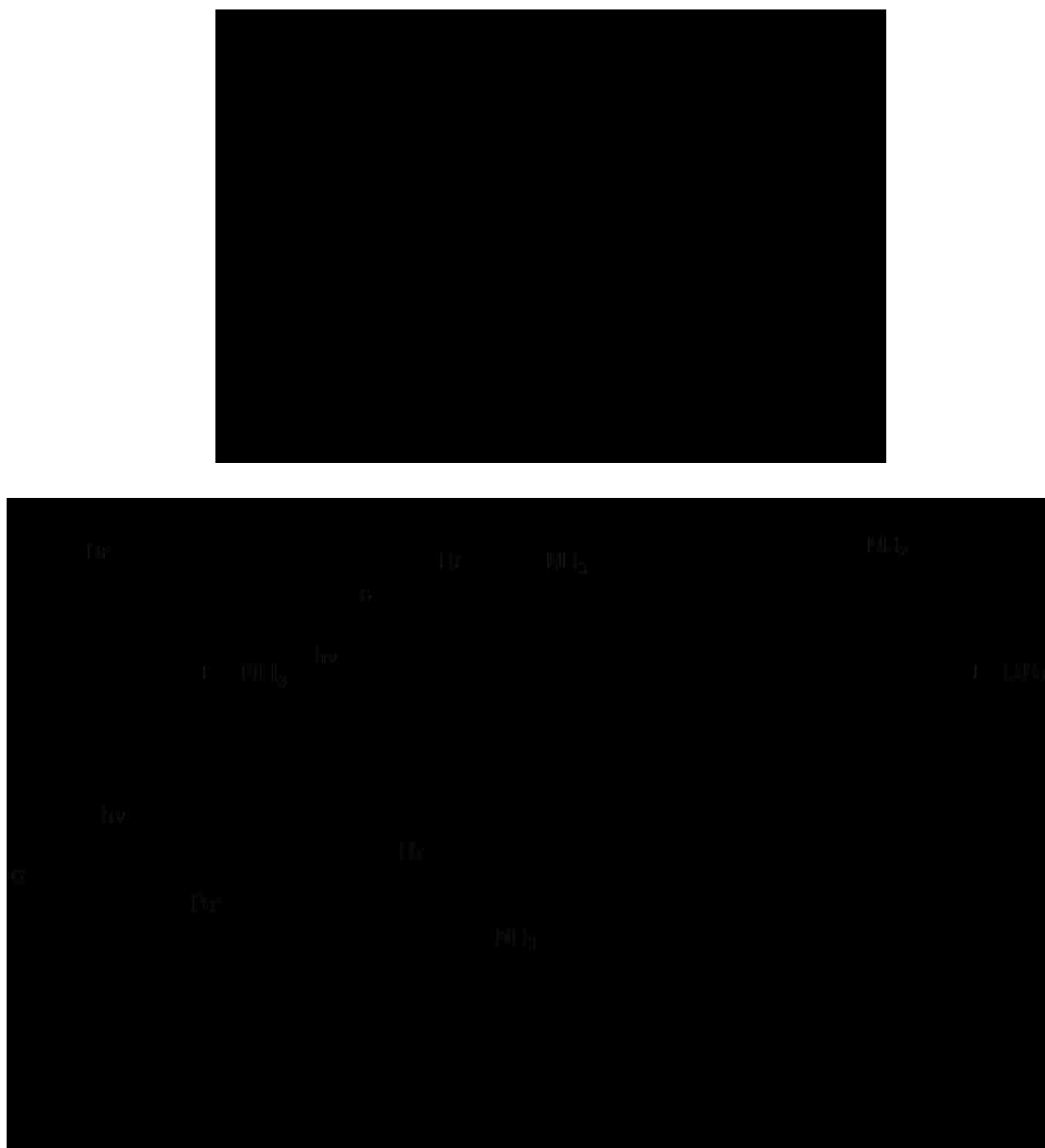


**Figure 28:** Schematic representation of process occurring after the photoionization of PhBr and PhBr-NH<sub>3</sub> complex. Two competing reaction pathways leading to the elimination of Br atom and HBr are shown.

Halobenzene molecular clusters with polar molecules such as ammonia have been known to result in intracuster nucleophilic substitution ( $S_N2$ ) reactions upon ionization.<sup>110, 113, 119, 120, 126</sup> Nucleophilic substitution ( $S_N2$ ) reaction mechanisms proceed by breaking one bond whilst forming another in one step. The two product channels occur competitively from the same Wheland intermediate, but it is not clear which channel is dominant in this system. However, in chlorobenzene – ammonia system, the halogen atom loss was found to be the dominant pathway by 85%.<sup>110</sup> In that study, they compared the mass ion ratios of aniline and protonated aniline and was found to be 1:5.4, this finding was also confirmed by microcanonical transition state theory calculations using Chemrate program suite. Here, the integrated ion intensity ratio is as good as 1:1 from the TOF mass spectrum Figure 26. There also exist an exit barrier to both channels from the Wheland intermediate, the size of the barriers for this system has not been studied yet, for the chlorobenzene system, it was found to be about 12kJ/mol for the Cl atom loss and about 25kJ/mol for the HCl loss.<sup>110</sup> The calculation of the stationary points leading to the products and of the branching ratios will be very informative on which pathway is favorable.

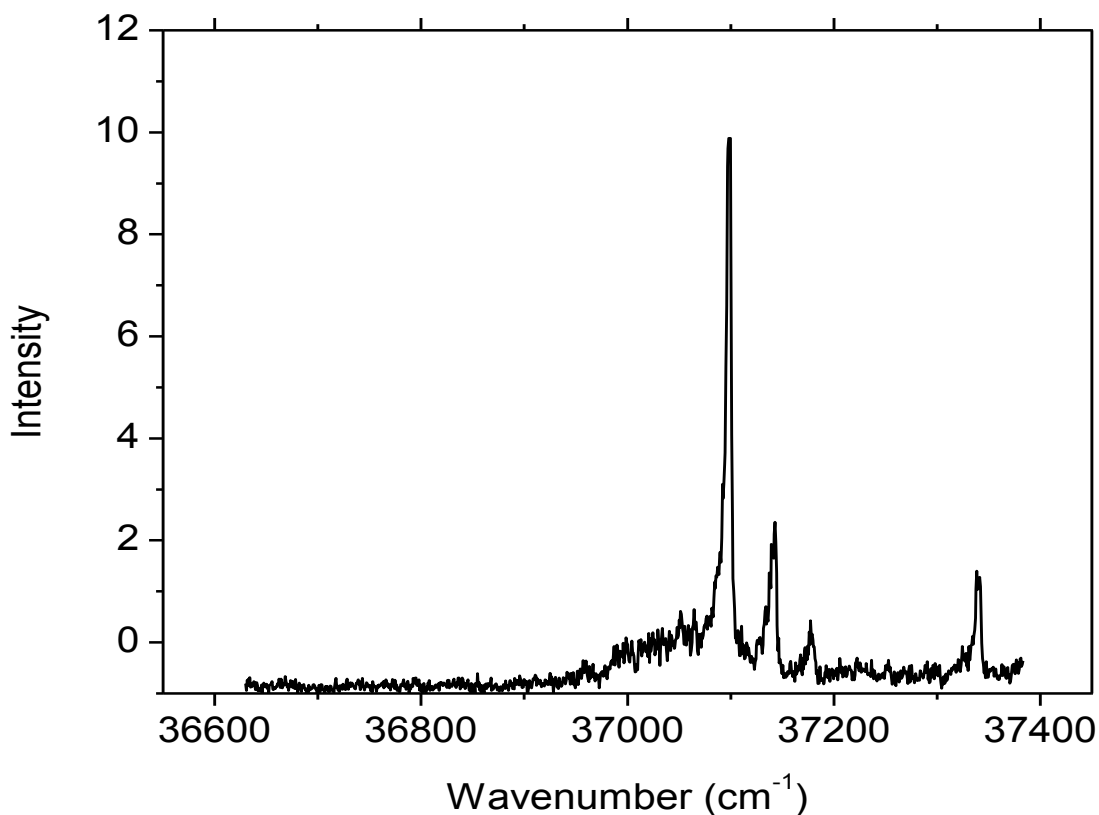


**Figure 29:** R2PI spectrum of PhBr-NH<sub>3</sub> van der Waals cluster obtained by scanning the protonated aniline mass channel.

The spectrum obtained by scanning the protonated aniline mass channel is displayed in Figure 29. It has a sharp origin band is at 37098 cm<sup>-1</sup>. Some weak unresolved vibrational hot bands can be seen to the red of the origin, these can be eliminated by further cooling of the molecular beam. The origin band is blue shifted by 90 cm<sup>-1</sup> from the S<sub>0</sub>-S<sub>1</sub> transition origin band of PhBr monomer. The corresponding dimer in PhF is blue shifted by 59 cm<sup>-1</sup>, and that of PhCl is blue shifted by 79 cm<sup>-1</sup>. The 1:1 dimer signal of PhCl and ammonia system was observed to be very small as compared to other higher order clusters with ammonia.

This was proven to be due to the fact that the 1:1 dimer undergoes a reaction upon ionization in the  $S_1$  state, hence its signal was diminished to such an extent that scanning over the protonated aniline mass channel produced a similar but cleaner spectrum in terms of signal to noise ratio. So far we have seen that PhBr is photo-fragmenting giving mainly the phenyl cation radical, this by itself reduces the number of PhBr molecules remaining to complex with ammonia. In its  $S_1$  state, PhBr is very short lived as was discussed earlier, its lifetime is 30 ps, that of PhCl is 1 ns, this short lifetime of PhBr makes the formation of clusters that last long enough to be probed very difficult. If the PhBr-NH<sub>3</sub> system behaves like the PhCl-NH<sub>3</sub> system, then its 1:1 dimer is expected to be completely consumed by secondary processes leaving close to nothing to be observed in the appropriate mass channel. The confidence that the spectrum in Figure 29 is that of 1:1 dimer comes from the fact that it is sharp, not broad. It could not be coming from higher order clusters of PhBr and NH<sub>3</sub> as these have a very broad electronic spectrum. Broad electronic spectra of higher order clusters were observed in similar systems of PhF and PhCl complexing with NH<sub>3</sub>. The conclusion drawn from this is that the 1:1 dimer complex is responsible for the R2PI spectra and it undergoes an intracuster nucleophilic substitution type reaction ( $S_N2$ ) forming aniline with the loss of neutral HBr molecule and the other channel producing protonated aniline with the loss of Br atom.

### 3.4 TDDFT CALCULATIONS

In order to address the question about which one amongst the five dimers optimized is responsible for the electronic spectrum shown in Figure 30. TDDFT calculations were carried out at M06-2X/ aug-cc-pVDZ level of theory. This level of theory was already benchmarked to perform fairly well for this kind of system. Its prediction of the vertical excitation energies to the  $S_1$  state of the PhCl-NH<sub>3</sub> system was accurate to within 10 cm<sup>-1</sup>.<sup>110</sup> The calculations predicted dimer 1 (D1), the most stable in plane  $\sigma$ -type conformer to be blue shifted with respect to the monomer absorption by about 150 cm<sup>-1</sup>. The experimental spectrum is blue shifted by 90 cm<sup>-1</sup>. This spectral blue shift indicates that the complex binding energy is smaller in the  $S_1$  state than in the electronic ground state by 90 cm<sup>-1</sup> because the electronic excitation has weakened the non-covalent interaction. D2, another  $\sigma$ -type conformer is not shifted with respect to the monomer absorption, the dimer is also the weakest bound (2.9 kJ/mol). The position of its NH<sub>3</sub> molecule at the para position makes it highly unlikely to attack the ipso carbon and form the cyclohexadienyl type intermediate. The leaving halogen atom is even too far to abstract a H atom from the NH<sub>3</sub>, hence, D2 is ruled out. On the other hand, the only halogen bonded dimer D3 is red shifted by 250 cm<sup>-1</sup>. The red shift signifies bond strengthening in the  $S_1$  state. The Br $\cdots$ N bond length shortens to 3.124 Å in the  $S_1$  state from 3.133 Å in the  $S_0$  state. D3 is ruled out as a candidate for the experimental R2PI spectra because of being red shifted and by such a wide margin. D4 and D5, the  $\pi$ -type conformers are slightly red shifted too by less than 10cm<sup>-1</sup> from the monomer.

This small red shift may not be enough to rule them out as their binding energy is similar to that of D1 and their geometry is well set to form the cyclohexadienyl type intermediate with the complex going through a massive geometry change in the S1 state. The NH<sub>3</sub> rotates and have its lone pair point towards the ipso carbon and the whole molecule translates towards the halogen atom and away from the ring whilst the hydrogen bond with the Br is maintained. The approach of the NH<sub>3</sub> bends the C-Br bond away from the plane of the PhBr which may lead to the formation of the intermediate. Multidimensional Frank-Condon vibronic structure simulations were then carried out. This procedure has been used in the past to streamline possible complex isomers that could be present in the molecular beam and responsible for the experimental spectra.

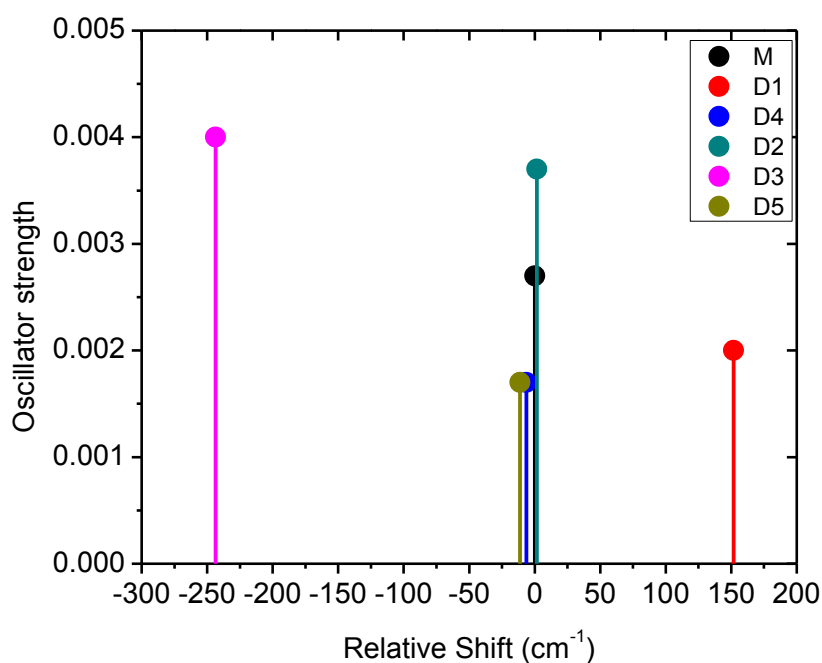


**Figure 30:** TDDFT calculations of the transition energy of the PhBr monomer (M) and five minimum energy structures. The energies were scaled (0.86 scaling factor) with reference to the experimental PhBr monomer absorption.

### 3.4.1 MULTIDIMENSIONAL FRANK-CONDON FACTOR SIMULATION

The simulation is based on the optimized geometries for ground and excited state, nuclear coordinates and the mass-weighted normal mode displacements incorporating the full effects of Duschinsky effect. The calculations were only done for the most stable  $\sigma$ -type (D2) and  $\pi$ -type conformer (D4). For  $\sigma$ -type, only five lowest frequency intermolecular modes were used in the simulation, three were used for the  $\pi$ -type conformer. In the implementation of this approach, only transitions from the ground state  $v=0$  were considered in the calculation of Franck-Condon factors for progressions of up to the third quanta in any one vibrational mode for  $\sigma$ -type. Increasing the transitions to higher vibrational quantum levels did not make any difference. However for the  $\pi$ -type, up to the eighth vibrational quantum level for the first intermolecular vibrational mode was included. The lowest three intermolecular frequency modes were used in the simulation; however, the lowest mode had a negative frequency for the  $\pi$ -type isomer (D4) in the  $S_1$  state which signifies a first order saddle point. The simulation uses ground state frequencies for the  $S_1$  state. Any differences in the standard orientation of the two states,  $S_0$  and  $S_1$ , are accounted for by the inclusion of Duschinsky normal coordinate transformation in its linear standard form as it is implemented in Pgopher.<sup>130</sup> Figure 31 shows the simulated electronic spectrum overlaid by the experimental spectrum collected over the phenyl cation mass channel. The simulation was done a selected most stable  $\sigma$ -type (D2) isomer. The stick spectra were transformed into continuous spectra by the convolution with the Gaussian function of  $5\text{ cm}^{-1}$  full width at half-maximum. The simulation for a selected  $\pi$ -type (D4) isomer is shown in Figure 32.

The spectrum is very rich in strong intermolecular vibrational structure associated with a massive change in equilibrium geometry from  $S_0$  to  $S_1$ . This significant change in geometry during the electronic transition is well evidenced by the strong Frank-Condon activity in these low-frequency intermolecular modes. The spectrum is in direct contrast with the experimental spectrum in which it was dominated by the  $S_0$ - $S_1$  origin band. However, for the  $\sigma$ -type (D2) complex, a spectrum exhibiting weak intermolecular activity and dominated by the origin band was obtained and it matches with the experimental spectrum. Coupling this with the fact that the D2 was the only blue shifted isomer, D2 is assigned the sole contributor to the experimental spectra.

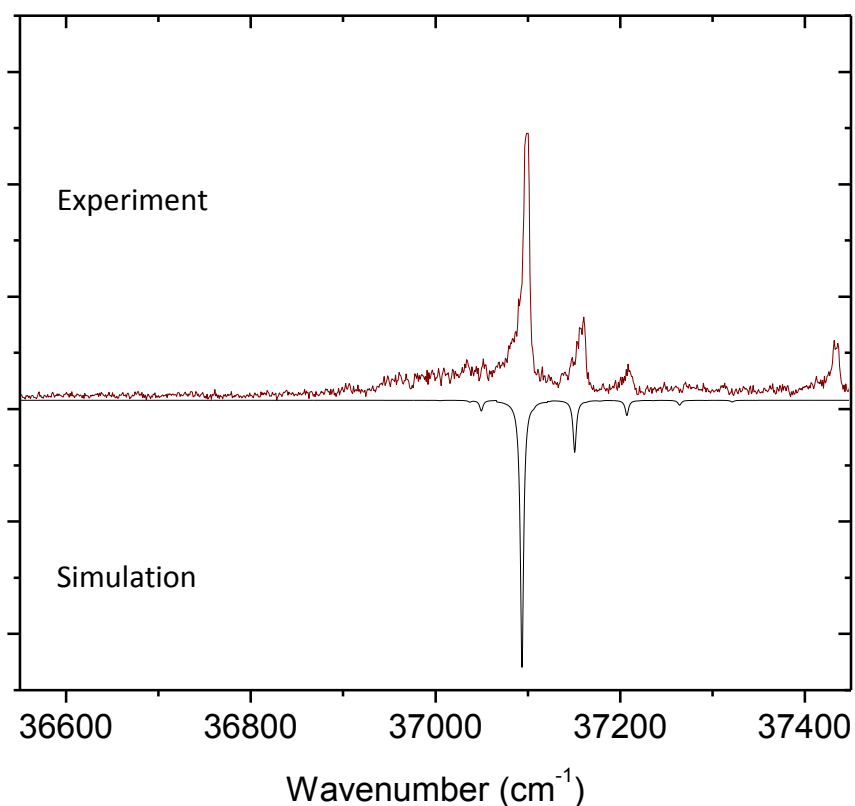


**Figure 31:** The experimental R2PI spectra for PhBr-NH<sub>3</sub> complex collected over the phenyl cation mass channel. The simulation is shown for the most stable  $\sigma$ -type (D2) isomer. The stick spectrum is convoluted with a Lorentzian linewidth of 3 cm<sup>-1</sup>.



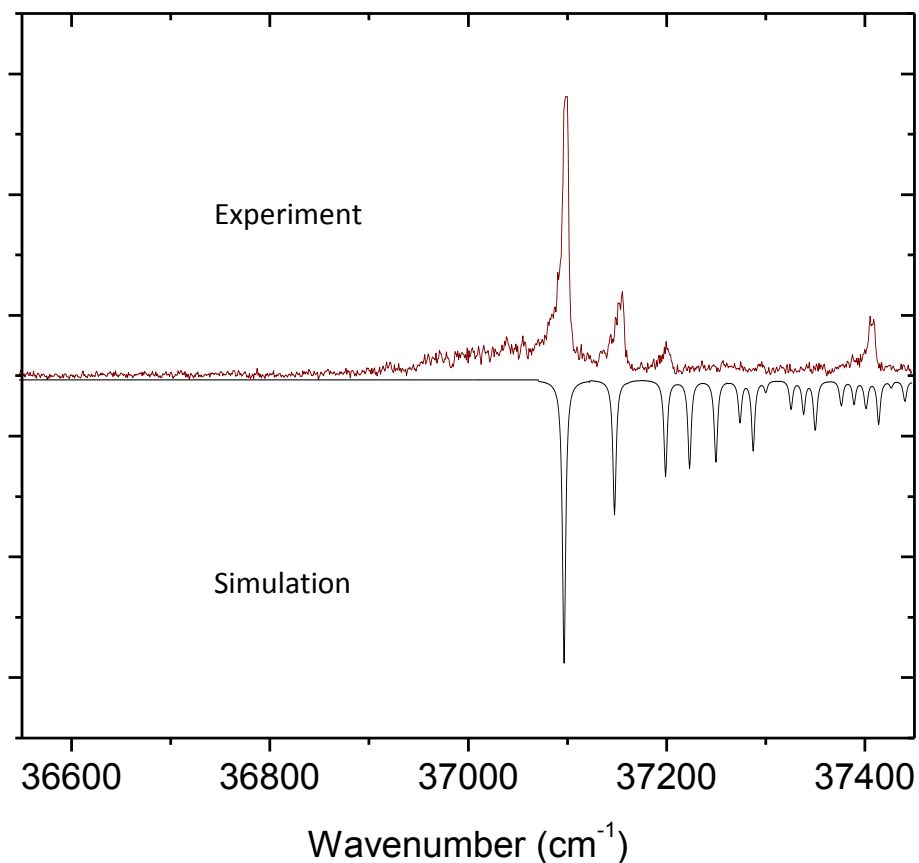


**Figure 32:** The experimental R2PI spectra for PhBr-NH<sub>3</sub> complex was collected over the phenyl cation mass channel. The simulation is shown for the most stable  $\pi$ -type (D4) isomer. The stick spectrum is convoluted with the Lorentzian linewidth of 3 cm<sup>-1</sup>.

#### SUMMARY ON PhBr-NH<sub>3</sub> DIMER

Studying bromobenzene systems hasn't been easy due to its shortened life time in the excited state and easy photo fragmentation upon photoionization. Regardless of the 1:1 dimer complex not observed in the TOF mass detection, the experimental spectrum was collected over a daughter ion mass peak. Computationally, five minimum energy structures were optimized, with the most bound  $\sigma$  and  $\pi$  type structures being isoenergetic (6.5kJ/mol).

Dimer 1 ( $\sigma$ -bound) has been shown to be the only structure predicted to exhibit a spectral blue shift upon electronic excitation to the  $S_1$  state. The experimental shift is  $90 \text{ cm}^{-1}$ , and TDDFT shift was  $150 \text{ cm}^{-1}$ . This is reasonable considering that the same method overestimated the shift in the PhCl-NH<sub>3</sub> system by about 12%. The computed neutral ground and first excited state geometries and frequencies were used to perform multidimensional Franck-Condon simulations of the  $S_0$ - $S_1$  vibronic spectrum for each of the relatively most stable conformers D1 and D4. The D1 simulated spectrum matched the experimental spectrum; both spectra were characterized by a dominant, blue shifted band origin with weak activity in intermolecular vibrational modes. The representative spectrum for the N-H/ $\pi$  bound structure (D4) was characterized by heavy Frank-Condon activity in the low frequency intermolecular vibrational modes. Summing up all these results, bromobenzene-ammonia van der Waals dimer complex is suggested that it preferentially adopts  $\sigma$ -bound structure.

#### SUMMARIZATION ON THE PhX-NH<sub>3</sub> VAN DER WAALS DIMERS

This section is a summarization of trends in the experimental work done on the non-covalent interactions involving mono substituted halobenzenes and ammonia. Table 1 list down the positions of the PhX monomer  $S_0 - S_1(\pi, \pi^*)$  transition origins as well as those for the corresponding van der Waals dimer with NH<sub>3</sub>. As the size of the halogen atom gets bigger, the excitation energies gets smaller. The relative shifts are all positive (blue shift) and the shifts gets bigger from PhF to PhBr complex system. Blue shifts signify a weakening binding of the cluster in the excited electronic state.

The agreement between computational results and experiment favors assignment of the spectra to the in-plane  $\sigma$ -type complex as responsible for the experimental R2PI spectra obtained. The experimental spectra are show in Figure 33.

**Table 1:** Summary of PhX-NH<sub>3</sub> van der Waals dimer complexes. The energies are in wavenumbers.

Van der Waals Dimer Complex	PhX monomer origin	Complex origin	Blue shift	Isomer Attributed
PhF-NH <sub>3</sub>	37830	37889	59	$\sigma$ -type
PhCl-NH <sub>3</sub>	37064	37143	79	$\sigma$ -type
PhBr-NH <sub>3</sub>	37008	37098	90	$\sigma$ -type

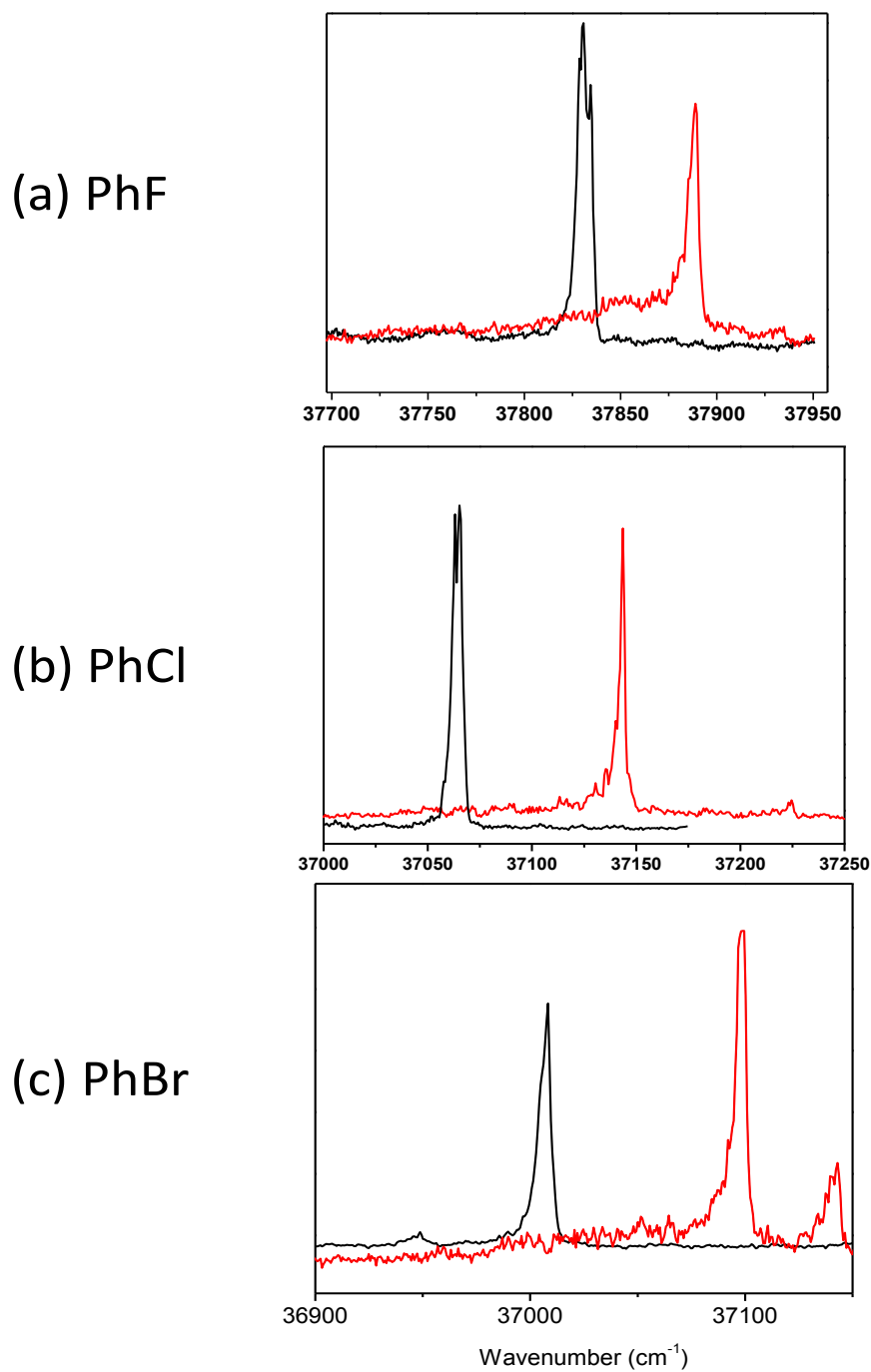


**Figure 33:** One-color R2PI spectra of mono substituted halobenzenes, PhX (black) and corresponding van der Waals dimer complex with  $\text{NH}_3$  (red). All dimers are blue shifted with respect to the PhX monomer origin.

## CHAPTER 4. ANILINE-CF<sub>3</sub>X VAN DER WAALS COMPLEXES

### 4.1 INTRODUCTION TO ANILINE-CF<sub>3</sub>X VAN DER WAALS

In the previous chapters, the properties and formation of a halogen bond were discussed. It was shown that it heavily depends on the size of the  $\sigma$ -hole.<sup>20, 24</sup> Fluorine as the most electronegative and hence least polarizable halogen, it was found it forms no sigma hole, unless it is attached to a heavily electron withdrawing residue.<sup>20, 24</sup> In a nutshell, for a given halogenated residue group, the  $\sigma$ -hole potential becomes more positive as its polarizability increases in the order  $F < Cl < Br < I$ . In search of halogen bonded complexes through experimental and computational means, work was done on fluorobenzene, chlorobenzene, and bromobenzene homo clusters.<sup>88, 131</sup> Expectation of finding a halogen bonded structure also increases in that order. Three weakly bound halogen bonded dimers were computationally optimized for bromobenzene, with the most bound dimer bound by 7.0 kJ/mol.<sup>24</sup> There were no halogen bonded structures in fluorobenzene or chlorobenzene. Instead of using homogenous halobenzene monomer units to form clusters and search for halogen bonded structures, a polar molecule in form of NH<sub>3</sub> was used as a nucleophile to form PhX-NH<sub>3</sub> dimers. Ab initio calculations found one minimum energy structure with a halogen bond bound by 3.7kJ/mol. This dimer structure is predicted to be red shifted with respect to the PhBr monomer absorption. Experimentally no red shifted absorption was observed and the conclusion was no halogen bonded structure was formed in the molecular supersonic jet.

Since these dimer conformations are formed in competition, the targeted halogen bonded type was just too weak to prevail.

This chapter is a continuation of a search of an experimentally characterized halogen bond. Here a system comprising of a stable aromatic chromophore in phenylamine (aniline)  $C_6H_5NH_2$  and trifluorohalomethanes,  $CF_3X$  ( $X=Cl, Br, I$ ) is chosen. The sigma hole on the halogen is expected to be boosted by using a powerful electron withdrawing residue. This was demonstrated recently by Metrangolo and coworkers who employed a variety of fluorine based residues to show that the size of the sigma hole depends also depends on electron withdrawing power of the residue. Even fluorine itself can have a significant sigma hole in  $CF_3O-F$ .<sup>24</sup> In  $C_6H_5NH_2 \cdots CF_3X$  system, the strongest halogen bond is expected with trifluoroiodomethane  $CF_3I$ .

#### 4.2 EXPERIMENTAL AND COMPUTATIONAL DETAILS

The spectroscopy of aniline and aniline-trifluoroiodomethane was studied using one color resonance two photon ionization spectroscopy (1+1 R2PI). Detailed description of the R2PI experimental setup is given in Chapter 2. High purity aniline and  $CF_3I$  samples were purchased from Sigma Aldrich and were used without any further processing.  $CF_3I$  was seeded to a 1-5% gaseous mixture with high purity He in a lecture bottle, the lecture bottle is connected to a bubbler that contains liquid aniline. The bubbler was maintained at 20°C and backing pressures ranging from 15-80 psi were used.

Geometry optimization of the  $C_6H_5NH_2 \cdots CF_3X$  van der Waals structures and their corresponding binding energies was done using the DFT functionals (M06-2X) with an aug-cc-pVDZ basis set. However for iodine containing species, aug-cc-pVDZ-PP basis set was employed as aug-cc-pVDZ is not available for iodine in Gaussian format. The basis set (aug-cc-pVDZ-PP) uses the aug-cc-pVDZ basis set in combination with an effective core potential, also called pseudo potential, to describe the valence charge density. Calculation of excitation energies were done using TD-M06-2X/ aug-cc-pVDZ level of theory.

#### 4.3 RESULTS AND ANALYSIS

The geometry optimization yielded at least six confirmations for each dimer system involving aniline interacting with  $CF_3Cl$ ,  $CF_3Br$  and  $CF_3I$ . The structures are shown in Figures 35, 36 and 37 respectively. All the structures optimized are out of plane  $\pi$ -type geometry. No in-plane  $\sigma$ -type structures were found. At least three halogen bonded structures were found for each  $C_6H_5NH_2 \cdots CF_3X$  dimer complex. The most stable structures were obtained for  $CF_3I$ , bound by 20kJ/mol. The conformations have the sigma hole on the halogen atom directly pointing into the electron rich  $\pi$  ring or directed towards the lone pair on the nitrogen. Other structures present involves establishment of hydrogen bonds with the  $\pi$  system and these were weaker. The trend of the binding energies in the halogen bonded structures increased from  $C_6H_5NH_2 \cdots CF_3Cl$  (10 kJ/mol) to  $C_6H_5NH_2 \cdots CF_3I$  (20 kJ/mol).

This proves that as the halogen atomic size increases, the polarizability of the electronic charge around the halogen atom improves leading to a larger positive electrostatic region along the C-X bond axis.

The R2PI electronic spectrum for aniline is shown in Figure 34. The  $S_0$ - $S_1$  ( $\pi \rightarrow \pi^*$ ) transition origin band is at  $34043 \text{ cm}^{-1}$ . The spectrum is sharp and dominated by the ( $S_0$ - $S_1$ ) origin band and the symmetric ring breathing mode  $6a$ . Yeh and coworkers (1996) obtained a similar spectrum with the origin band at  $34030 \text{ cm}^{-1}$ .<sup>93</sup> In search of the dimer complexes signal, also observed are some aniline – water clusters in the TOF mass spectrum. Aniline formed these hydrogen bonded clusters with water from the background; this was eliminated by evacuating the system over night and using liquid nitrogen in the shroud to trap the background gases. The search of the dimer signals is still on going as there were some experimental setbacks during this period and the problems have since been rectified. Once the experimental spectrum is obtained, it is compared with the ab initio calculation results obtained. A convincing conclusion can then be made of the preferred binding motif in the An- $\text{CF}_3\text{I}$  van der Waals dimer system as well as the An- $\text{CF}_3\text{Br}$  and An- $\text{CF}_3\text{Cl}$  system.



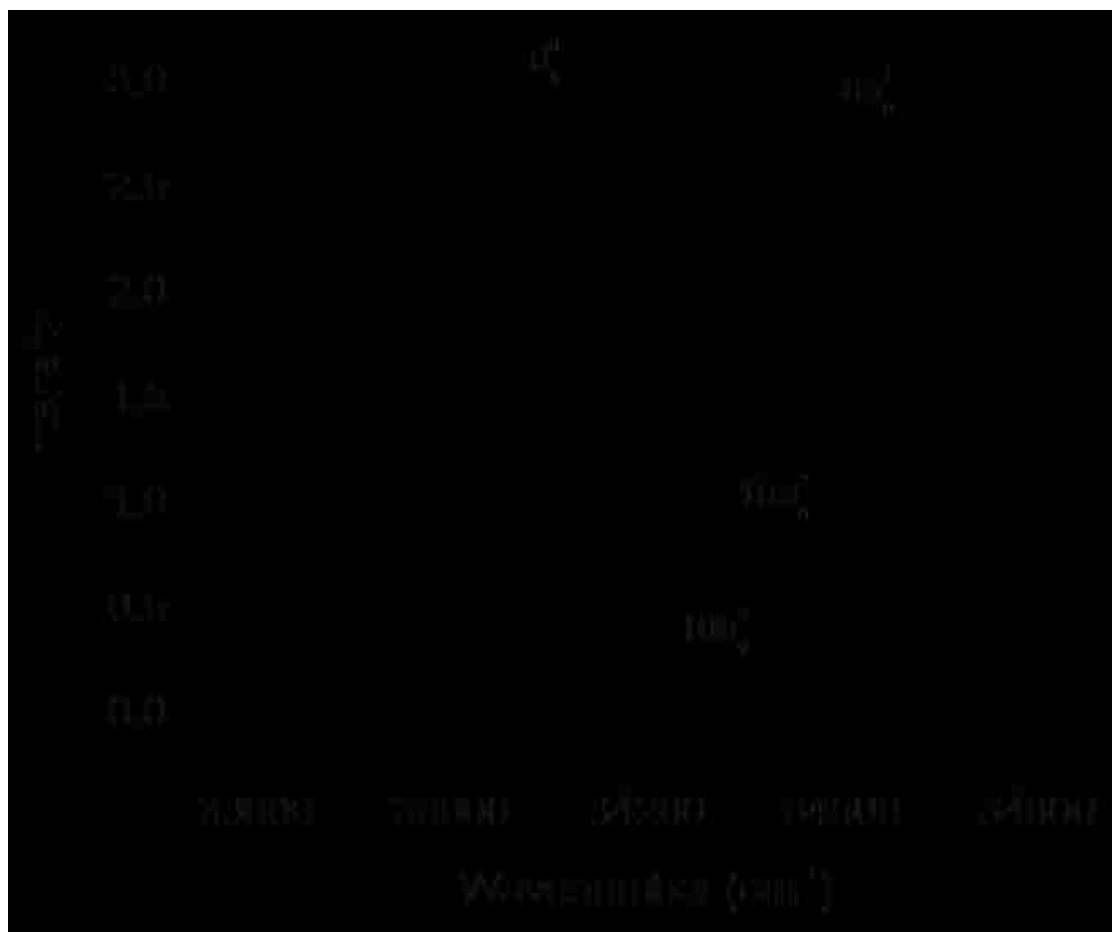


**Figure 34:** R2PI spectrum of aniline. The assignments of the vibrational modes is obtained from reference.<sup>93</sup>

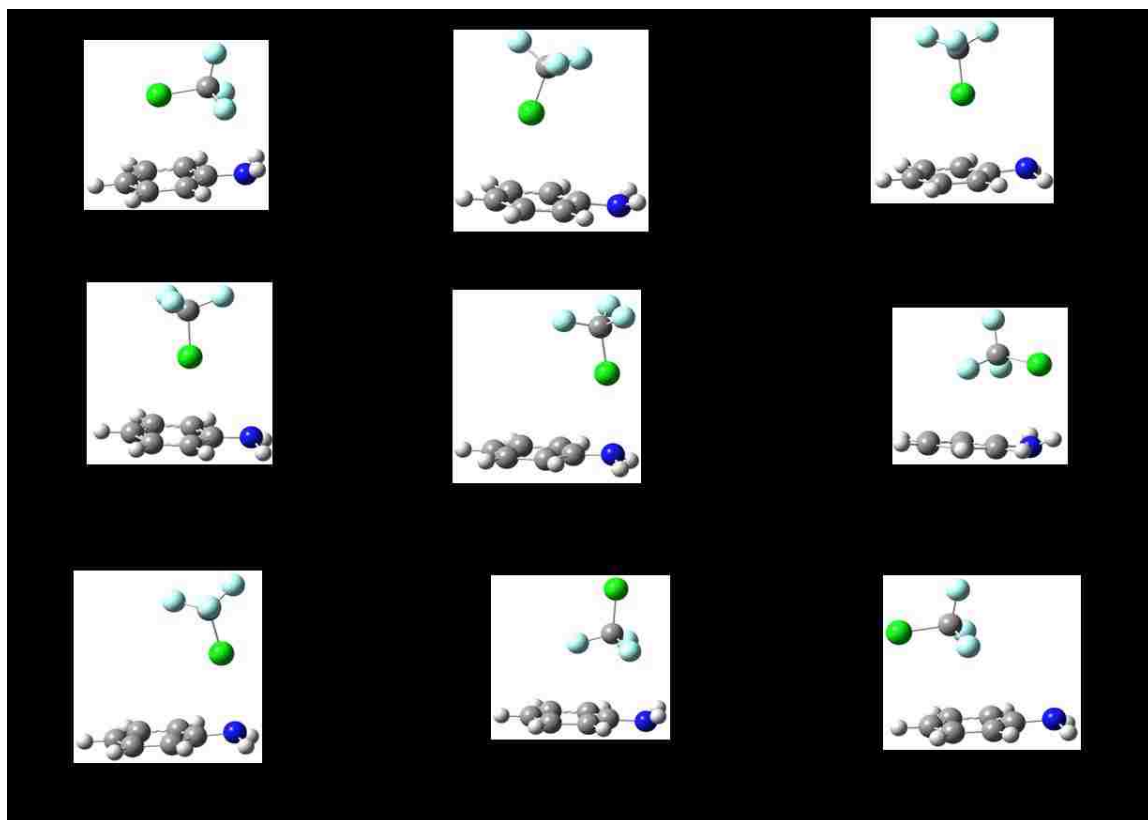


**Figure 35:** Aniline-CF<sub>3</sub>Cl van der Waals dimer system calculated at M06-2X/aug-cc-pVDZ level of theory. The binding energies are corrected for basis set superposition error and zero point energy.

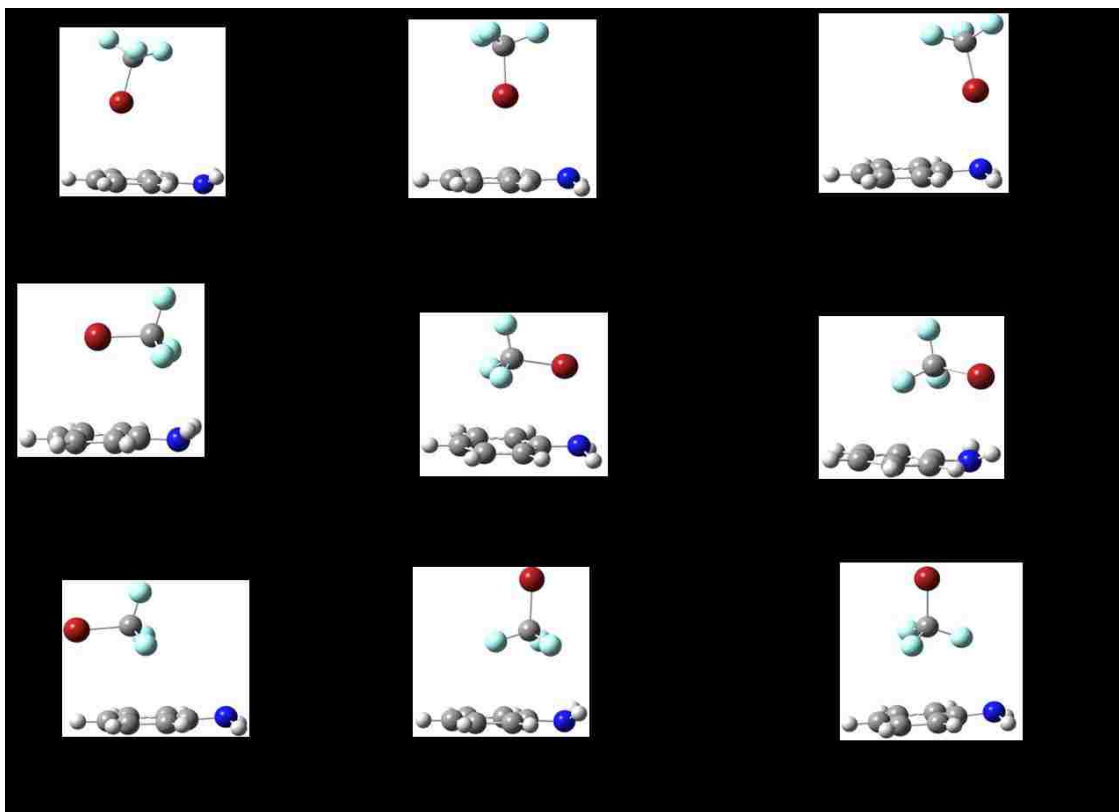


**Figure 36:** Aniline- $\text{CF}_3\text{Br}$  van der Waals dimer system calculated at M06-2X/aug-cc-pVDZ level of theory. The binding energies are corrected for basis set superposition error and zero point energy.

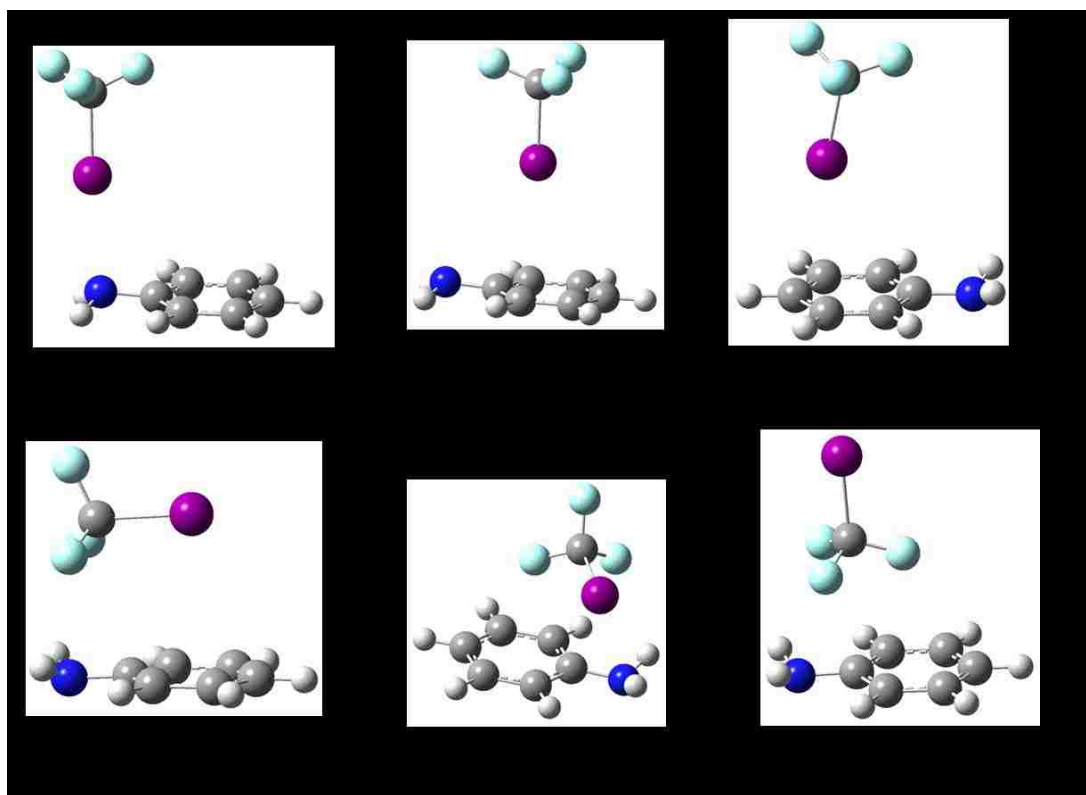


**Figure 37:** Aniline-CF<sub>3</sub>I van der Waals dimer system calculated at M06-2X/aug-cc-pVDZ-PP level of theory. The binding energies are corrected for basis set superposition error and zero point energy.

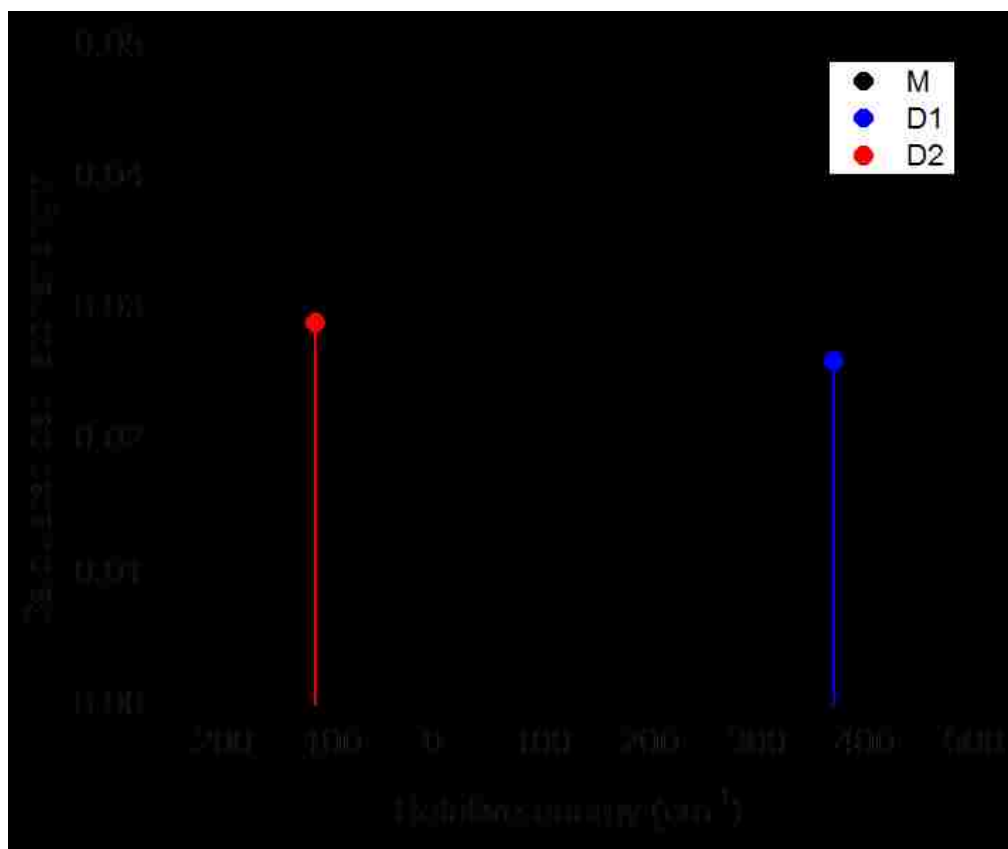


**Figure 38:** Relative excitation energies calculated for D1 and D2 conformers of the An-CF<sub>3</sub>I system. The energies are scaled using the experimental aniline monomer (M) origin transition.

TDDFT vertical excitation energy calculations on selected  $C_6H_5NH_2 \cdots CF_3I$  halogen bonded dimers (D1 and D2) were carried out and are shown in Figure 38. The energies were scaled with respect to the experimental aniline  $S_0-S_1$  transition origin band energy ( $34043\text{ cm}^{-1}$ ). In D1, the sigma hole is interacting with nitrogen's lone pair and in D2 the sigma hole is interacting with the negative aromatic  $\pi$  field. As was seen in bromobenzene dimers, any interaction involving the perturbation of the  $\pi$  electron system destabilizes the delocalized electron system resulting in the lowering of energy levels in both electronic states. In case of a red shift in transition energy, the lowering of energy levels is effected more in the excited state than the ground state. The excited state will be stabilized more than the ground state.

In the  $C_6H_5NH_2 \cdots CF_3X$  dimer systems, it's not a question of whether the structure is an in plane  $\sigma$ -type or out of plane  $\pi$ -type because all structures are out of plane. To characterize the most bound structures further as either  $\sigma$ -hole-NH interaction or  $\sigma$ -hole/ $\pi$  interaction, one can employ a combination of one-color resonant two photon ionization (R2PI) and IR-vibrational spectroscopy (depletion spectroscopy) to obtain the N-H stretching frequencies. The calculated IR shifts in the region of the N-H symmetric stretching mode are shown in Figure 39. The calculated shifts are with respect to the calculated N-H stretching frequencies in free aniline molecule. D1 is red shifted by  $32\text{ cm}^{-1}$  and D2 is blue shifted by  $12\text{ cm}^{-1}$ . A small blue shift in both split stretching frequencies is associated with a  $\sigma$ -hole/ $\pi$  interaction whilst a larger red shift is associated with a  $\sigma$ -hole-NH interaction. IR/R2PI depletion spectroscopy can be used to obtain experimental N-H stretching frequencies that can be compared with the calculated frequencies to determine which conformer is formed in the molecular beam.

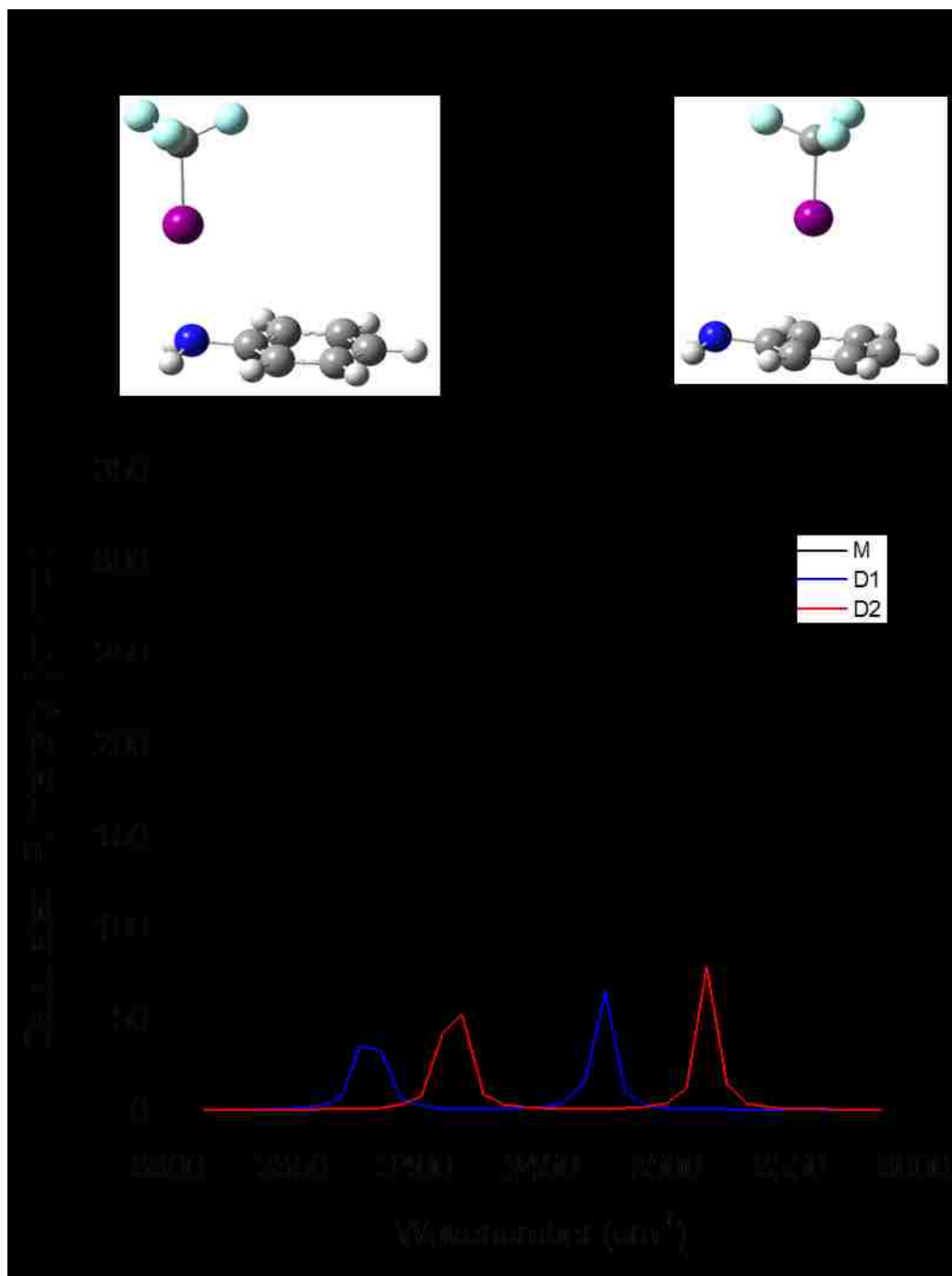


**Figure 39:** IR stretching N-H frequencies of An-CF<sub>3</sub>I dimers D1, D2 and that of the monomer (free aniline molecule).

## SUMMARY

Ab initio calculations obtained multiple dimer isomers for Aniline-CF<sub>3</sub>X van der Waals dimer systems. It was found that the system is composed of only out of plane structures with the strongly bound structures being the halogen bonded structures. As expected, An-CF<sub>3</sub>I system produced the most stable structures bound by 20kJ/mol. This binding energy is equal to that calculated for the most stable chlorobenzene and bromobenzene non covalent dimers, which were experimentally observed. The TDDFT calculations have shown that dimers bound by the  $\pi$ -electron system have red shifted ( $S_0$ - $S_1$ ) excitation energies whilst the dimers bound by nitrogen lone pair are blue shifted with respect to the aniline origin band. The two kinds of binding motifs are also isoenergetic and cannot be distinguished by calculation alone. The R2PI experimental spectra can shed more light on the type of binding motif preferred in these dimer systems. IR/R2PI depletion spectroscopy can also be used to compare the N-H stretching frequencies with those in a free aniline monomer molecule. If the binding with the sigma hole is over the  $\pi$ -electron system, minimal shifts are expected on the N-H stretching frequencies. If the binding is targeting the negative electronic charge on the nitrogen, then large red shifts are expected.



## CHAPTER 5. MODELING SPIN-ORBIT COUPLING IN MONOHALOCARBENES

## 5.1 INTRODUCTION TO MONOHALOCARBENES

Carbenes are organic molecules with a neutral divalent carbon atom that is covalently bonded to two other substituents. The central carbon has two non-bonding electrons. Methylene ( $\text{CH}_2$ ) is taken as the prototype carbene molecule. Other simple carbene species after methylene are the halomethylenes ( $\text{CHX}$ ,  $\text{X}=\text{F}$ ,  $\text{Cl}$ ,  $\text{Br}$ ,  $\text{I}$ ). Halocarbenes plays an important role in atmospheric and interstellar chemistry. In addition to their atmospheric importance, carbenes find a very useful application in synthetic and polymer chemistry<sup>132</sup>. They are also involved in gas phase combustion<sup>133</sup> and organic synthesis in which they usually occur as reactive intermediates.<sup>134-139</sup> Carbenes gathers a lot of interest in these applications due to their unusual chemical properties emanating from the multiple electronic configurations by which the two non-bonding valence electrons can be arranged, see Figure 40.

The history of carbenes in general is dated back to early nineteenth century when they were first postulated. Most of the studies were centered on the determination of the geometry, singlet-triplet gaps and intersystem crossing rates. In spectroscopy and photochemistry, electronic spectra of halocarbenes have been studied both experimentally and theoretically and continue to receive a fair amount of attention today. The lowest lying  $\text{CHX}$  singlet states ( $\tilde{X}^1\text{A}'$  and  $\tilde{A}^1\text{A}''$ ) can also be used to study the Renner-Teller (RT) coupling since they are formed via Renner-Teller coupling from a degenerate  $^1\Delta$  electronic state at linear geometry.<sup>140, 141</sup>

The coupling of these two states as the barrier to linearity is approached greatly affect the radiative emission back to the singlet ground state,  $\tilde{X}^1A'$  by enhancing internal conversion to the  $S_0$  state<sup>137</sup>. Between the ground singlet state,  $\tilde{X}^1A'$  and the first excited state,  $\tilde{A}^1A''$ , there lies a background triplet state,  $\tilde{\alpha}^3A''$ , which couples with the ground  $\tilde{X}^1A'$  via spin-orbit coupling and also couples with the first excited singlet state,  $\tilde{A}^1A''$ , via second order mixing. The strength of these interactions in halo carbenes varies from species to species depending on a number of factors, some will be discussed here as well as has been done in great details in other references.<sup>136, 137, 141-155</sup>

In this study, spin-orbit coupling in mono-halocarbenes is being modelled. This type of interaction was found to play a major role in the perturbation of vibrational levels of the interacting states.<sup>13, 136, 137, 141, 143, 146, 148, 156-163</sup>. Motivation to probe the spin orbit coupling comes from previous experimental and theoretical work done so far on mono halocarbenes. For all the carbene species, higher lying energy levels were difficult to assign firmly because of the presence of some perturbation between the electronic states. My research group has done some extensive work on carbenes in recent years that mainly involve laser induced fluorescence (LIF), single vibronic level emission (SVL), stimulated emission pumping (SEP) experiments, and some theoretical studies to support the practical work. It was observed that some vibrational levels, both in the singlet and triplet state were heavily perturbed from their zeroth order positions that were predicted theoretically by different computational methods. Assignment of the observed perturbed vibrational levels proved a challenge without the knowledge of the amount of perturbation on a particular vibrational level.

There is need to develop a global spin orbit coupling analysis method that can predict perturbed positions of the vibrational levels. There is a growing understanding of the types of interactions and processes that exist in halocarbenes that involves their electronic states. In this report, modeling of spin orbit coupling in halocarbenes has enabled us to account for the strong perturbations of vibrational energy levels observed in the SVL emission and SEP experiments. Vibrational levels were then assigned firmly for both the singlet and triplet state.

## 5.2 ELECTRONIC STRUCTURE OF MONOHALOCARBENES

The divalent carbon and its lone pair of electrons gives carbenes three possible spin states, namely, two singlet states and a triplet state as indicated in Figure 40. There has been a lot of theoretical and experimental work on monohalocarbenes in the past few years.<sup>135, 152, 153, 157, 162, 164-172</sup> From *ab initio* calculations, monohalocarbenes were found to possess a singlet ground electronic state with  $^1A'$  orbital symmetry in  $C_s$  point group symmetry. The first excited state is a triplet with  $A''$  orbital symmetry in  $C_s$  symmetry. Studies have shown that for  $CH_2$ , the triplet configuration is more stable than the first excited singlet state.<sup>161, 173</sup> The first singlet state ( $S_0$ ) is less stable in  $CH_2$  due to the electron- electron repulsion between the two electrons in the same molecular orbital which is an  $sp^2$  hybrid orbital. Also the triplet state is lower in energy than the next singlet state ( $S_1$ ), this is due to the spin exchange interaction (Hund's rule; a quantum mechanical interaction that spreads out electrons with parallel spins).

However, in CHX carbenes, a string of studies have shown that the singlet is the ground state ( $\tilde{X}^1A'$ ), with the first excited state being a low lying triplet state ( $\tilde{a}^3A''$ ).<sup>140, 143, 146, 156, 157, 174, 175</sup> Back donation from the p-orbital of the halogen atom stabilizes the singlet configuration.<sup>173</sup> Figure 40 shows the electronic structure of singlet mono halocarbenes. The singlet ground state ( $S_0$ ), have two non-bonding spin paired electrons in an  $sp^2$  hybridized orbital which is the HOMO (highest occupied molecular orbital). The carbon center also has an empty p orbital, or LUMO (lowest unoccupied molecular orbital). The first four low lying electronic states in CHX/CDX carbenes ( $S_0, T_1, S_1, S_2$ ) are given in Figure 40. The triplet states possess two unpaired electrons in separate orbitals. A lot of studies have been centered on the geometry and the singlet- triplet energy gap as it is believed the reactivity of the two states is different. It was also shown that upon excitation, the C-H and C-X bond lengths change a little.<sup>137</sup> However, singlet CHX molecules have smaller bond angles ranging from 100 to 112 degrees, the triplets have a much wider bond angle ranging from 125 to 132 degrees. This significant change in geometry is due to the promotion of an electron from a carbon lone pair orbital coplanar with carbon – halogen bonds to an empty carbon p orbital that is orthogonal to the plane of the molecule.<sup>137</sup>

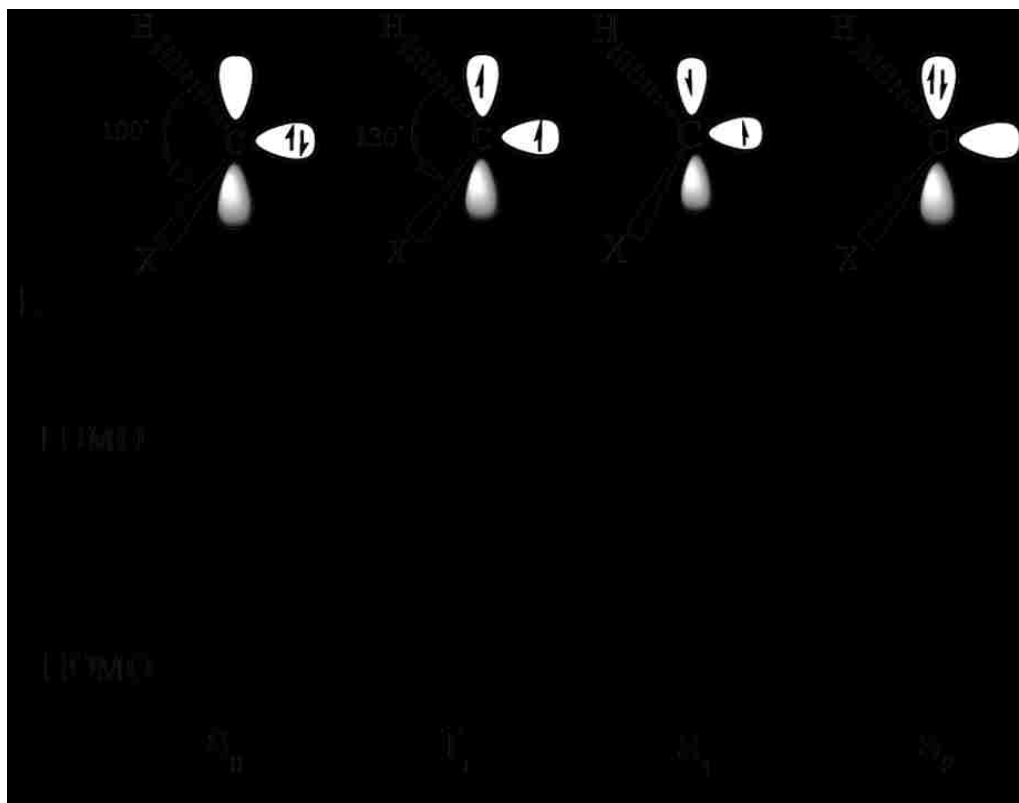


**Figure 40:** Electronic structure of mono-halocarbenes, CHX (X=I, Br, Cl, F). The bond angle is approximately  $100^\circ$  for the singlet states and about  $130^\circ$  for triplet excited states.  $S_0$  is the singlet ground state,  $S_1$  and  $S_2$  are excited singlet states,  $T_1$  is the first excited triplet state.

### 5.3 SPIN-ORBIT COUPLING

Spin-orbit coupling (SOC) arises from the interaction between the orbital angular momentum ( $\vec{L}$ ) of the nucleus and the electron spin angular momentum ( $\vec{S}$ ). The electron's spin angular momentum induces a magnetic moment  $\vec{\mu}_s$ , that interacts with another magnetic moment  $\mu_L$ , due to the electron's orbital angular momentum.<sup>176, 177</sup> Since angular momentum should be conserved during an electron's spin orientation change, the p orbital that is coupled to the electron spin must change its orientation in space a unit angular momentum.

This is achieved if the p orbital undergoes a 90° rotation, overlapping with the adjacent p orbital, this move produces one unit of angular momentum thereby satisfying the conservation of angular momentum.<sup>176</sup> This SOC causes shifts in atomic energy levels. The shift in energy is directly proportional to orbital angular momentum ( $\vec{L}$ ) and spin angular momentum ( $\vec{S}$ ),  $\Delta E \propto \vec{L} \cdot \vec{S}$ . The effect of SOC is also detectable as a splitting of spectral lines. In mono-halocarbenes, such as CHX and their deuterated isotopomers, there is a triplet state  $\tilde{a}^3A''$  that lies in close proximity to the ground singlet state  $\tilde{X}^1A'$ . As a result, this close proximity between these two states leads to mixing of their energy levels via SOC, thereby causing mixed levels to shift in position (perturbation). The energy difference between the unperturbed levels and the perturbing levels is a big factor that determines the strength of the mixing and perturbation, the larger the energy gap separation, the smaller is the probability of mixing via SOC, and the less singlet-triplet intensity borrowed to the perturbing triplet state.<sup>136, 142, 170</sup> As will be shown later, mixing is not necessarily guaranteed for all vibrational levels that happen to lie close to each other. The singlet states, which are basically being mixed with triplet states experiences different admixtures due to different mixing coefficients given by:

$$\text{Mixing coefficient} = \frac{\langle S_0 | \hat{H}_{SO}^{elec} | T_1 \rangle}{E_t - E_s}$$

Where  $\langle S_0 | \hat{H}_{SO}^{elec} | T_1 \rangle$  is the matrix element,  $\hat{H}_{SO}^{elec}$  corresponds the interaction that couples  $S_0$  and  $T_1$  electronic states and  $E_t - E_s$  is the energy gap between the triplet state and the singlet state vibrational level.<sup>176, 178, 179</sup>



Without SOC interaction, and neglecting all other kinds of interactions, any radiative transitions from the singlet to the background triplet state are strictly spin-forbidden. However the introduction of SOC will see some of these transitions being allowed. These spin-forbidden transitions from the  $S_1$  to the  $T_1$  state have been observed experimentally due to the mixing of the  $S_0$  state with the  $T_1$  state.<sup>136, 142, 157, 162, 170</sup> The corresponding radiative rates of the transitions are dependent on the oscillator strength. The intensity of the singlet – triplet transitions is directly proportional to the magnitude of the SOC between the two interacting states. SOC itself is strongly depended on the following factors:<sup>176</sup>

- a) The ability of the non-bonding electrons to approach the positive nucleus as close as possible.
- b) Size of the positive charge on the atom center to be felt by the approaching electrons (atomic number).
- c) The presence of a one-atom center  $p_x \rightarrow p_z$  transition that is used to generate orbital angular momentum that couples the spin angular momentum.
- d) The probability of transitions between the perpendicular orbitals.



### 5.3.1 SPIN-ORBIT COUPLING IN GAUSSIAN 09

The method used in Gaussian 09 to approximate spin-orbit coupling between two states is based on the theoretical work by Abegg et al (1975).<sup>180</sup> It is only available for the elements H through to Cl (online Gaussian 09 User Reference). Gaussian 09 can compute spin-orbit coupling between two electronic states during a CASSCF calculation by including the *CASSCF=SpinOrbit* keyword in the route section.<sup>103</sup> This computes approximate spin orbit coupling between two states, specified on a separate input line. Calculations on excited states of molecular systems are requested using the *NRoot* option. For CASSCF *NRoot=1* is the ground state, so to make the first excited state the state of interest, *NRoot* is set to 2 (*NRoot=2*). In calculating spin-orbit coupling, the integrals are computed in a one-electron approximation involving relativistic terms, and then it uses effective charges that scale the *Z value* for each atom to empirically account for 2 electron effects<sup>103</sup> This value can be specified for each atom via the molecule specification nuclear parameters.

Most *ab initio* calculations of spin orbit coupling treat spin-orbit coupling as a perturbation.<sup>181-186</sup> In this perturbation approach one-component calculations are to obtain molecular orbitals and then use them to compute spin-orbit coupling. One can work with all electron basis sets or choose to replace them with some core electrons potentials, this greatly reduce computation costs and allow calculations on larger systems.

Examples of core potentials includes, effective core potential (ECP), model core potential (MCP), *Ab initio* model potential (AIMP).

Computer codes that calculate SOC have mostly followed the following path:<sup>184</sup>

1. *The Hamiltonian.*

The most commonly used operator is the Breit-Pauli. It includes two-electron terms (spin-same orbit and spin-other orbit interactions).<sup>183</sup>

$$H_{so} = \frac{1}{2}\alpha^2 \sum_{i\lambda} \left[ \frac{Z_\lambda}{r_{i\lambda}^3} (\mathbf{r}_{i\lambda} * \mathbf{p}_i) \mathbf{s}_i \right] - \frac{1}{2}\alpha^2 \sum_{i \neq j} \left[ \frac{1}{r_{ij}^3} (\mathbf{r}_{ij} * \mathbf{p}_i) (\mathbf{s}_i + 2\mathbf{s}_j) \right]$$

$Z_\lambda$  denotes actual charge on nucleus  $\lambda$ . The first term is the spin-same orbit interaction (one electron) and the second term is the spin –other orbit interaction term (two-electron term). Neglecting the two-electron term, in-order to simplify the operator, leads to a significant over-estimation of the SOC.<sup>186</sup> The distance between electron  $i$  and electron  $j$  is denoted as:  $|r_{ij}| = |r_i - r_j|$ ,  $\mathbf{p}_i$  is the momentum operator for the  $i^{\text{th}}$  electron,  $\mathbf{s}_i$  is an appropriate spin operator,  $\alpha$  is a constant.

2. *Electronic molecular wave functions:*

SOC is treated as a perturbation using non-relativistic unperturbed wave functions and found to be more accurate only if the SOC is small, valid for small molecules involving the up-to period 3 elements. Configuration interaction (CI) has been the popular method of choice to develop the zero-order wave functions.<sup>187</sup>

3. *Integrals:*

Integral evaluation has been achieved by efficient algorithms. Similar algorithms are used to generate atomic components of one and two-electron SO interactions.

4. *Matrix elements:*

The involvement of two different spin states in a transition makes the computation of SOC matrix elements challenging. However convenient expressions have been adopted for determinants and spin adapted electronic wave functions.<sup>188</sup>

5. *Atomic orbital bases:*

Numerical HF orbitals for atoms, Slater type orbitals for diatomics and Gaussian type for molecules have the popular representation used.

6. *Configuration interaction (CI) algorithms:*

Full CI limit was employed on small diatomics to test the reliability of the various truncated CI treatments available, one has to compromise between cost and accuracy.<sup>189</sup>

#### 5.4 GROUND STATES IN CARBENES: SINGLET - TRIPLET STATE PREFERENCE

Carbenes can have a ground state possessing two spin paired electrons in a non-bonding orbital (NB) forming a singlet state with a  $(\text{NB})^2(\text{NB})^0$  configuration. Triplet carbenes have the non-bonding electrons in different orbitals with an  $(\text{NB})^1(\text{NB})^1$  configuration.

The highest occupied NB orbital of a singlet state is a strongly bonding MO, any spin paired electrons in this orbital form a stable configuration. The two NB orbitals are localized on the carbon atom of the carbene molecule. The small energy gap separating these two NB orbitals has a significant effect on the rate of singlet-triplet transitions. A small energy gap between the two NB orbitals enhances mixing of the excited  $S_1$  and  $T_1$  state with the  $S_0$  state. Since there is not much energy advantage to be gained by pairing electrons in such circumstances, and rather to minimize electron repulsion associated with  $(NB)^2(NB)^0$  configuration, electron configuration  $(NB)^1(NB)^1$  is favored resulting in a triplet ground state. On the other hand, large energy gap between the two orbitals in the excited state lowers the probability of mixing with the ground state with  $(NB)^2(NB)^0$  configuration being highly favored, hence such molecule will have an electron paired singlet ground state. All the mono halocarbenes under discussion in this work were found to possess a singlet ground state whilst methylene has a triplet ground state. In halocarbenes under study here (CHX), the singlet state is more stable than the triplet state, unlike in  $CH_2$  where the triplet state is more stable.<sup>173</sup> The stabilization of singlet states by halogen substituents can be explained in a couple of ways. The halogen atom has a high electron affinity, it occupies orbitals of increased p character, and this enhances the s character of the nonbonding pair of electrons  $sp^2$  hybridized orbital leading to a stable singlet state.<sup>190</sup>

The singlet state stabilization was also explained in a different way by Schwartz<sup>173</sup>, he considered the  $\pi$  –electron-donating capacity of the halogen constituent atom induce greater stabilization of the singlet state by electron donation to the empty p orbital.

## 5.5 LITERATURE SURVEY

In recent years, there has been a lot of advancement on the theoretical and experimental work on methylene and halocarbenes.<sup>136, 152, 153, 155, 161, 163-172, 191-194</sup> This section mainly summarizes the work that has been done prior to this study. The experimental data used in the new calculations comes from the single vibronic level emission (SVL) and stimulated emission pumping (SEP) experiments from literature. I will briefly describe these two techniques. Later on, a detailed discussion of the theoretical work will be given.

### 5.5.1 SINGLE VIBRONIC LEVEL EMISSION (SVL) SPECTROSCOPY

A single vibronic level (SVL) emission spectrum is typically obtained following the excitation from the ground state ( $\tilde{X}$ ) to a particular excited state( $\tilde{A}$ ) vibrational level. The fluorescence from that particular excited vibronic level is directed into a spectrograph equipped with a diffraction grating. The grating, acting as a monochromator disperses the fluorescence into its constituent wavelengths and mirrors would direct the dispersion towards the detector.

The initial excitation of the molecules is from the ground state ( $S_0$ ) state level to a particular vibronic level in the  $S_1$  state. Emission to the lower electronic states then follows.

The frequency of light emitted is a function of the energy of the transition, and since energy must be conserved; the energy difference between the two states equals the energy carried off by the photon and detected. Usually, there is need for calibration of the emission spectra, one can calibrate using for example a hollow cathode lamp spectra.

### 5.5.2 THE SINGLET-TRIPLET GAP IN MONO HALOCARBENES

A central goal in carbene chemistry has been to experimentally determine and theoretically predict the magnitude of the singlet-triplet gap ( $\Delta E_{ST}$ ). Singlet states and triplet states have different reactivities, thus making the  $\Delta E_{ST}$  crucial in determining the reactivity of a given carbene species. Our research group has played a leading role in mono halocarbene chemistry in recent years.<sup>152, 166, 167, 170</sup> The  $\Delta E_{ST}$  decreases with increasing atomic size of the halogen atom as shown in Figure 41.

#### 5.6.1 THEORETICAL DETERMINATION OF $\Delta E_{ST}$

Schwartz and Mashall<sup>173</sup> performed high level of theory calculations on  $\text{CH}^{35}\text{Cl}$  using a quadratic configuration interaction with single and double excitations and a triples excitation contribution (QCISD(T)) with the 6-311+G(3df,2p) basis set. They also employed the Gaussian-2 (G2) method with the same basis set. Their calculations suggested that the  $\Delta E_{ST}$  in  $\text{CH}^{35}\text{Cl}$  lies between 23.7-37.7  $\text{kJmol}^{-1}$  (1991-3167  $\text{cm}^{-1}$ ).

Tarczay and coworkers<sup>195</sup>, using a complete quartic force field computed with a coupled-cluster theory including all single and double and perturbation correction for triple excitations (CCSD(T)) with an augmented correlation consistent polarized valence quadruple-zeta basis set (aug-cc-pVQZ). This level of theory estimated the  $\Delta E_{ST}$  of  $\text{CH}^{35}\text{Cl}$  to be  $2170(40) \text{ cm}^{-1}$ . Calculations using a multi-reference configuration interaction with a triple-zeta basis set, MRCI/aug-cc-pVTZ incorporating spin orbit coupling by Yu and co-workers predicted the same  $\Delta E_{ST}$  in  $\text{CH}^{35}\text{Cl}$  at  $2160.3 \text{ cm}^{-1}$ .<sup>194</sup> All these results are in strong agreement with *ab initio* and DFT calculations using the B3LYP hybrid functional with an augmented triple-zeta basis set, B3LYP/aug-cc-pVTZ with the inclusion of spin orbit interaction between the two states. The  $\Delta E_{ST}$  energy gap in the  $\text{CH}^{35}\text{Cl}$  was predicted to be  $2167.8 \text{ cm}^{-1}$  and that in  $\text{CD}^{35}\text{Cl}$  to be  $2183.9 \text{ cm}^{-1}$ .

The  $\Delta E_{ST}$  in  $\text{CHBr}$  and  $\text{CDBr}$  has also received a fair amount of theoretical investigation in recent years. Yu and coworkers<sup>193</sup> carried out some high level *ab initio* calculations at MRCI/cc-pVTZ, they computed the spin orbit coupling matrix elements using a complete active space(CAS) self-consistent field with a minimal basis set that uses slater type orbitals simulated by 3 gaussians added together (CASSCF/STO-3G). They obtained the singlet-triplet transition energy of  $2028.35 \text{ cm}^{-1}$  for  $\text{CHBr}$  and  $2065.76 \text{ cm}^{-1}$  for  $\text{CDBr}$ . As expected, in their results, the spin orbit effects on the vibrational energy levels in the singlet state for  $\text{CHBr}$  induced large energy shifts in the bending and combination modes. Another recent singlet-triplet gap investigation on bromocarbenes comes from Jean Standard and coworkers.<sup>163</sup>

They computed the  $\Delta E_{ST}$  gap ( $1669\text{cm}^{-1}$ ) in CHBr at the MRCI+Dav/cc-pVTZ (multi-reference configuration interaction plus the Davidson's correction which approximately corrects the size consistency error of the MRCI) level and corrected for zero-point vibrational energies. However, they also investigated the effect of using larger basis sets on the energy gap by using larger basis sets, cc-pVQZ ( $1854\text{cm}^{-1}$ ) and cc-pV5Z ( $1922\text{cm}^{-1}$ ). The results indicated that an increase in basis set size also increases the singlet–triplet gap. Their calculations however ignored the effects of spin-orbit coupling as they regarded the effect to be small.

The amount of work done on iodocarbenes over the years has shown that, unlike other halocarbenes, CHI/CDI have been more elusive. Hajgato and co-workers<sup>146</sup>, tried quite a number of computational methods in trying to predict the singlet-triplet gap. One of the methods they used was CCSD(T)/6-311++G(3df,2p) that predicted the CHI  $\Delta E_{ST}$  at  $18.9\text{KJ/mol}$  ( $1578\text{cm}^{-1}$ ).<sup>146</sup> Bacskay and co-workers<sup>140</sup> computed relative energies of the singlet ground state  $\tilde{X}^1A'$ , excited singlet state  $\tilde{A}^1A''$ , and excited triplet state  $\tilde{a}^3A''$  of CHI. They calculated atomization and dissociation energies in the complete basis limit by extrapolating (R/U)CCSD(T) and Davidson corrected MRCI energies calculated with aug-cc-pVxZ (x=T, Q, 5) basis sets. The basis sets were corrected for core-valence correction, spin-orbit coupling and zero point energies. Geometries and vibrational frequencies were computed at CASPT2/cc-pVTZ, which is a second-order perturbation theory based on a CASSCF reference state. They predicted the singlet-triplet gap in CHI at  $3.7\text{kcalmol}^{-1}$  ( $1294\text{cm}^{-1}$ ) which is relatively comparable to the value of  $1392\text{cm}^{-1}$ . Theoretical studies on the singlet-triplet gap in CHF/CDF predicted values which range from about  $4600 - 5530\text{cm}^{-1}$ .<sup>154, 159, 173, 190, 196</sup>



The singlet-triplet gap in CHF/CDF is larger than any of the halocarbenes shown in Figure 41. Martin Schwartz and Paul Marshall<sup>173</sup> computed the adiabatic energy gaps between the singlet and triplet state (which included vibrational ZPE). They did this for a number of halocarbenes using G2 and QCISD(T)/6-311+G-(3df,2p) energies. The  $\Delta E_{ST}$  [QCISD(T)] for CHF was predicted at  $59.8 \text{kJmol}^{-1}$  ( $4930 \text{cm}^{-1}$ ), which lies within the theoretical range predicted by most groups. It is believed the spin orbit coupling matrix elements in CHF/CDF are very small; there was no theoretical evidence of coupling in this system. When the spin orbit coupling constant is now comparable to the anharmonicity of the vibrational levels, it becomes very difficult to accurately determine the coupling effect between the two states, therefore any  $\Delta E_{ST}$  in CHF or CDF system that includes spin orbit coupling effect wasn't pursued.

### 5.6.2 EXPERIMENTAL DETERMINATION OF $\Delta E_{ST}$

Tao and co-workers obtained a  $\Delta E_{ST}$  in  $\text{CH}^{35}\text{Cl}$  at  $2163.28 \text{cm}^{-1}$  or  $6.1852(2) \text{kcalmol}^{-1}$  via some high resolution stimulated emission pumping spectroscopy experiments.<sup>170</sup> Lin and coworkers<sup>160</sup> observed a weak emission triplet peak for  $\text{CH}^{35}\text{Cl}$  and  $\text{CD}^{35}\text{Cl}$  at  $2167 \text{cm}^{-1}$  and  $2187 \text{cm}^{-1}$  respectively. They obtained laser excitation spectra of several vibronic bands originating from the origin of the  $\text{CH}^{35}\text{Cl}/\text{CD}^{35}\text{Cl}$  ground singlet state, to the first excited singlet state. They then recorded a dispersed fluorescence spectra from some excited state levels to various singlet state levels.

The  $\Delta E_{ST}$  energy gap in  $\text{CH}^{35}\text{Cl}$  was predicted to be  $2167.8\text{cm}^{-1}$  and that in  $\text{CD}^{35}\text{Cl}$  to be  $2183.9\text{cm}^{-1}$ , which is in very good agreement with both theory and other experimental results.

The singlet – triplet gap in  $\text{CHBr}$  and  $\text{CDBr}$  has also been investigated both experimentally and theoretically.<sup>140, 141, 157, 165, 173, 193</sup> Early studies were done by Xu and co-workers, they obtained laser induced fluorescence excitation spectra for both molecular species at visible wavelengths in a pyrolysis free jet expansion experiments.<sup>192</sup> Tao and co-workers reported a fluorescence excitation and SVL emission spectra of jet cooled  $\text{CDBr}$  and they assigned the triplet origin to be at  $2065(1)\text{cm}^{-1}$ .<sup>165</sup> Chang and co-workers performed some dispersed fluorescence experiments on  $\text{CHBr}$  and  $\text{CDBr}$  following excitation of several  $\tilde{A} \leftarrow \tilde{X}$  vibronic bands. They used an ICCD detector and their spectra had very good signal to noise ratio. In their studies, they confirmed the singlet – triplet gap in  $\text{CHBr}$  to be at  $2005\text{cm}^{-1}$  and at  $2061\text{cm}^{-1}$  for  $\text{CDBr}$ .<sup>141</sup>

A spectrum of  $\text{CHI}$  was obtained only a few years ago by Chong and company, and a few other groups have worked on the singlet-triplet energy gap.<sup>145, 154, 166, 173, 196</sup> Chong Tao and his coworkers observed three levels centered at around  $1400\text{cm}^{-1}$ , the region where the triplet origin is expected to show up. Obviously two of the levels were singlet and probably perturbed by the neighboring levels. They assigned the triplet origin to be the peak that showed up at  $1407\text{cm}^{-1}$  and made it clear that the position is not the true triplet origin; one has to do some deperturbation analysis in order to determine the true unperturbed triplet origin position. They did a two level non-degenerate perturbation theory analysis and calculated the  $\Delta E_{ST}$  to have a lower limit of  $1315\text{cm}^{-1}$  ( $3.76\text{ kcal mol}^{-1}$ ).<sup>166</sup>

There is more theoretical work done on the determination of the  $\Delta E_{ST}$  gap in CHF/CDF than experimental determination. Gilles and coworkers, from their experimental photoelectron spectra of CHF deduced a  $\Delta E_{ST}$  of  $5210(140) \text{ cm}^{-1}$ .<sup>145</sup> Mukarakate and coworkers reported a single vibronic level emission spectra of CHF and CDF which mapped vibrational levels up to  $10000 \text{ cm}^{-1}$  above the ground singlet state ( $\tilde{X}^1A'$ ) origin in which they determined the triplet origin position.<sup>135, 164, 171</sup> In this report, no  $\Delta E_{ST}$  can be given that takes into account the presumably small effect of the spin orbit coupling. Previous studies<sup>135</sup> couldn't find any evidence of the existence of spin-orbit interactions between the low lying triplet state and the ground singlet state.

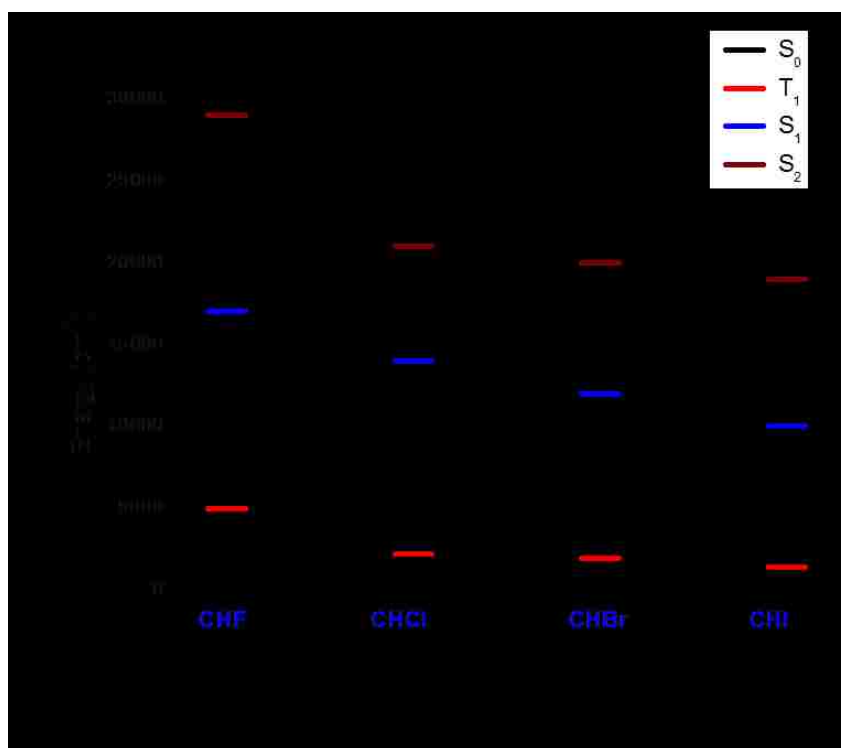


**Figure 41:** Energy level diagram for monohalocarbenes, showing how the singlet-triplet energy gap varies with the atomic size of the halogen atom on the molecule.  $S_1$  and  $S_2$  energies taken from literature.<sup>174</sup>

## 5.7 SPIN-ORBIT COUPLING (SOC) AND PERTURBATION OF STATES

The interaction of the electron spin with the orbital angular momentum of non-circular orbits leading to a spin flip was found to be more pronounced in molecules that contain heavy halogen atoms (heavy atom effect).<sup>136</sup> The halogen atom improves the chances of a spin forbidden singlet-triplet transition by coupling of the electron's spin with its angular orbital momentum. The coupling causes some orthogonal atomic orbital interactions at almost same geometry, this increases the probability of a spin change.<sup>177</sup> It is expected that the spin orbit coupling in CHX be of similar magnitude to that experienced in the deuterated species, CDX. This is because substituting hydrogen with deuterium or heavy hydrogen (hydrogen with an added neutron to its nucleus) does not affect the electronic structure of the molecule or the positive nuclear charge the electrons feels from the center atom. However, this is not always the case, some corresponding singlet state energy levels from CHX and CDX were perturbed by different margins, which means the matrix elements coupling the two levels in each molecule are not uniform or there are other effects contributing the selective perturbations. The next subsections cover a few selected examples of these perturbations.

### 5.7.1 SOC IN CHF AND CDF

The magnitude of the spin-orbit element dramatically drops as the atomic number of the halogen atom decreases and as the singlet-triplet gap increases.<sup>142, 151, 173</sup>

In their dispersed fluorescence spectra of CHF, Mukarakate and co-workers<sup>135</sup> observed a strongly perturbed vibrational structure in the  $\tilde{X}^1A'$  state, but did not obtain any evidence of spin-orbit interactions with the low lying  $\tilde{a}^3A''$  state. The perturbations observed were due to the anharmonic resonances within the  $\tilde{X}^1A'$  manifold. In one of their articles<sup>148</sup>, they used polarization and Zeeman quantum beat spectroscopy (QBS) to probe the perturbations and the nuclear hyperfine structure of CHF. QBS can efficiently distinguish RT and spin-orbit effect contributions in a system. In the calculations, no significant spin orbit fit parameter for CHF/CDF was obtained; its contribution to the perturbations is quite very minimal.

### 5.7.2 SOC IN CHCl AND CDCl

Spin orbit effects in CHBr/CDBr are expected to be larger than those of CHCl/CDCl. This means the perturbations experienced by singlet levels in CHCl/CDCl due to nearby triplet levels are weaker. Yu and coworkers<sup>194</sup> used MRCI/cc-pVTZ method and calculated the vibrational energy levels incorporating spin-orbit effects. They predicted the spin-orbit coupling to be in the range of 80-120cm<sup>-1</sup> for the CHCl/CDCl system. To investigate the size of the spin-orbit interaction, Tao and co-workers selected three pairs of interacting singlet-triplet levels in CH<sup>35</sup>Cl, they derived their vibronic spin-orbit matrix elements using term energies and spin-spin constants.<sup>170</sup> They obtained an electronic spin orbit element of 150cm<sup>-1</sup>. As will be shown later, the calculated spin orbit coupling constant of 96.5cm<sup>-1</sup> is within the range predicted by Yu and co-workers for both CHCl and CDCl.

Analysis shows that the singlet bending levels are the most perturbed due to the larger vibrational overlap they share with the triplet state levels, which is associated with the large change in equilibrium bond angle.

### 5.7.3 SOC IN CHBr AND CDBr

Even though the amount of mixing between two electronic state energy levels heavily relies on the separation of the two energy levels, it was found that the interaction is also selective regardless of separation<sup>165</sup>. Yu and coworkers studied the coupling in CHBr/ CDBr system<sup>193</sup>. Their results showed that the bending and combination vibrational modes with a bending mode were most perturbed by the triplet state energy levels. For example the (0,2,0) level in  $\tilde{X}^1A'$  was perturbed by the triplet origin (0,0,0). The (0,0,0) triplet level was just  $158.6\text{cm}^{-1}$  below the  $\tilde{X}$  (0,2,0) level in CHBr. But the same triplet origin was about  $407\text{cm}^{-1}$  above the (0,2,0) level in CDBr  $\tilde{X}^1A'$ . The spin orbit coupling element for a pair of singlet-triplet levels in CHBr is expected to be of the same magnitude to that experienced by a corresponding pair of levels in CDBr even though they observed a weakened perturbation on (0,2,0) level in CDBr than in CHBr by the  $\tilde{a}$  (0,0,0) level. Unfortunately they did not give the magnitude of this spin orbit coupling element. However Tao and co-workers<sup>165</sup> did some deperturbation analysis, and derived the spin orbit matrix element to be around  $330\text{cm}^{-1}$  in the CDBr system.

### 5.7.4 SOC IN CHI AND CDI

Tao and co-workers<sup>166, 167</sup> reported a fluorescence excitation and emission spectra of CHI and CDI. In their work, they concluded that the spin-orbit mixing above the  $\tilde{a}$  (0,0,0) was so severe that only a few vibrational levels could be assigned. The spin-orbit matrix element for the  $\tilde{a}$  (0,0,0) and the  $\tilde{X}$  (0,2,0) was estimated to be around  $160\text{cm}^{-1}$ .

## 5.8 POTENTIAL ENERGY SURFACES

A typical mono halocarbene potential energy surface is shown in Figure 42 for CHI showing two singlet states  $\tilde{X}^1A'$ ,  $\tilde{A}^1A''$  and the  $\tilde{a}^3A''$ . At linear geometry, the two singlet states become doubly degenerate and become a  $^1\Delta$  electronic state. This low lying triplet state and the ground singlet state cross each other in nonlinear geometries and end up perturbing each other via spin orbit coupling. Yu and co-workers calculated the spin orbit coupling element near the crossing seam in the  $\text{CH}^{35}\text{Cl}$  system to be somewhere around  $80\text{-}120\text{cm}^{-1}$ .<sup>194</sup> Singlet-triplet transitions are strictly spin forbidden but spin-orbit coupling mixes the singlet and triplet states, making the transition weakly allowed. The strength of the transition is governed by the magnitude of the spin orbit coupling matrix element  $\langle S_0 | \hat{H}_{so} | T_1 \rangle$ , which should be non-zero for any coupling to be experienced. The coupling itself is inversely proportional to the energy gap between the two states and so to improve it, at least higher lying  $S_0$  vibrational energy levels need to overlap with the  $T_1$  origin and some lower lying excited vibrational levels as shown in Figure 42.

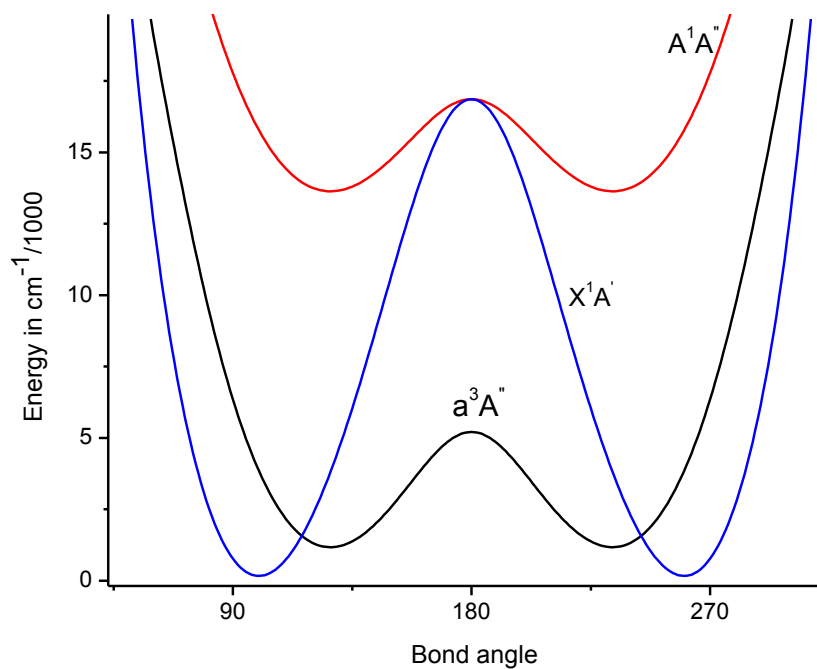


**Figure 42:** A potential energy surfaces for CHI in the lowest triplet state and two lowest singlet states interpolated from *ab initio* DFT calculations at B3LYP/sadlej-pVTZ level of theory.

## 5.9 METHODOLOGY

### 5.9.1 COMPUTATIONAL METHODS

A number of different computational methods and basis sets have so far been tried to calculate the vibrational frequencies, optimized geometries, singlet-triplet gaps and spin orbit coupling matrix elements in halocarbenes. From literature, Density Functional Theory (DFT) methods have been used to calculate vibrational frequencies, equilibrium geometries and singlet-triplet energy gaps.



However not all DFT functionals are good for computing all these parameters, hybrid density functionals tend to overestimate the singlet-triplet energy gap<sup>154</sup>. B3LYP functional was mainly used in conjunction with a triple-zeta basis set. B3LYP quantitatively reproduced harmonic vibrational frequencies very well. It was previously used in good agreement with experiment to predict the vibrational frequencies.<sup>152, 153, 165-170</sup> B3LYP functional however is not reliable on predicting the singlet-triplet energy gap. Schwartz and Marshall<sup>173</sup> investigated the singlet-triplet gaps in quite a number of carbenes and they used the QCISD(T) and Gaussian 2 (G2). The two methods were used with basis sets up to 6-311+G(3df,2p), the results deviated from the experimental values by some margin in all the carbene species. The calculations were performed on the singlet and triplet states of the mono-halocarbenes (CHX) and their deuterated isotopomers (CDX) using Gaussian 09 on Marquette University Pere cluster.<sup>103</sup> Density Functional Theory (DFT) method with B3LYP /aug-cc-pVTZ was employed for the geometry optimization and vibrational frequency calculations for CHBr, CHCl and their deuterated isotopomers. For CHI and CDI, Sadlej-pVTZ basis set was used as this reproduced the harmonic frequencies better. Computations on iodine species (CHI and CDI) were later done by employing the recently developed correlation consistent basis set for iodine, aug-cc-pVTZ-PP, it uses the aug-cc-pVTZ basis set in combination with an effective core potential, also called pseudo potential, to describe the valence charge density.<sup>197</sup> The basis set produced a slight improvement to the fitting from the previously employed B3LYP/Sadlej-pVTZ method.

From these calculations, structures, vibrational frequencies, and normal mode displacements are extracted and used to calculate the vibrational overlaps of the singlet and triplet state levels, incorporating the full effects of Duschinsky mixing<sup>198</sup> in Pgopher program.<sup>130</sup> Error analysis was done in Matlab.

### 5.9.2 EQUILIBRIUM GEOMETRIES

To investigate the equilibrium geometries of the  $\tilde{X}^1A'$  and the  $\tilde{a}^3A''$ , calculations at the B3LYP/aug-cc-pVTZ level were carried out for CHBr/CDBr and CHCl/CDCI system. B3LYP/Sadlej-pVTZ was used for CHI/CDI system. The general structure of all the mono halocarbenes is bent. Table 2 gives a summary of the findings; the deuterated species have similar geometry and are summarized in Table 3. The bond angle in the ground singlet states range was  $100.5^\circ - 102.2^\circ$ , the bond angle opens up in the triplet state to a range of  $126.7^\circ - 129.7^\circ$ . The bond lengths slightly shorten in the triplet state, the only major change change in geometry in the triplet state is the  $25^\circ - 30^\circ$  degree increase in the bonding angle in all the species.

**Table 2:** Optimized CHX geometries at the B3LYP/aug-cc-pVTZ level.

Species	R1(C-H)Å	R2(C-X)Å	Bond angle
<b>Singlet state</b>			
CHI	1.127	2.078	100.5
CHBr	1.107	1.868	101.1
CHCl	1.108	1.704	102.2
<b>Triplet state</b>			
CHI	1.101	2.013	129.7
CHBr	1.083	1.819	127.1
CHCl	1.083	1.664	126.7

**Table 3:** The optimized geometries of deuterated monohalocarbenes at the B3LYP/aug-cc-pVTZ level.

Species	R1(C-H)Å	R2(C-X)Å	Bond angle
<b>Singlet state</b>			
CDI	1.127	2.079	100.5
CDBr	1.107	1.868	101.1
CDCl	1.108	1.704	102.2
<b>Triplet state</b>			
CDI	1.101	2.013	129.7
CDBr	1.083	1.819	127.1
CDCl	1.083	1.664	126.7

### 5.9.3 VIBRATIONAL OVERLAPS

The Frank-Condon principle states that the most probable transitions between electronic states occur when the wave function of the initial vibrational state most closely resembles the wave function of the final vibrational state. The orbital overlap integral  $\langle\psi_1|\psi_2\rangle$  defines the extent of the mathematical orbital overlap for a pair of electronic wave functions or a set of orbitals. The  $\langle\psi_1|\psi_2\rangle$  takes a unit maximum value for perfectly overlapping vibrational wave functions. The square of the overlap intergral,  $\langle\psi_1|\psi_2\rangle^2$  gives the Frank-Condon Factor (FCF) between the two states. FCF is also a measure of the vibrational overlap of the two wave functions and it shades more light on the probability of a radiative or radiationless electronic transitions. Here the vibrational overlap intergral  $\langle S_0(v_1, v_2, v_3) | T_1(v_1, v_2, v_3) \rangle$  is defined as the extent of overlap between a pair of energy level wave functions from a singlet,  $S_0(v_1, v_2, v_3)$  and triplet,  $T_1(v_1, v_2, v_3)$  state.

The simulation of the vibrational overlaps between the ground singlet and the triplet state for each molecular halocarbene was done with Pgopher.<sup>130</sup> Important initial input parameters to the program includes, the molecular point group (Cs), atomic masses, nuclear coordinates, normal mode displacements, the harmonic frequencies in both states, minimum and maximum vibrational quantum number to include in a particular vibrational overlap simulation, and also symmetry of the electronic states. These results were then incorporated with the electronic spin-orbit matrix element into a matrix diagonalization scheme.

#### 5.9.4 FRANK CONDON FACTORS (FCF)

The calculation of the FCF involved a few steps in Pgopher<sup>130</sup>. The multidimensional potential energy surfaces of the two electronic states involved in the electronic transition is determined and the square of the vibrational overlap integral are evaluated. Figure 45 shows the Frank-Condon Factors associated with the overlap of the singlet vibrational level wave-functions with the triplet origin,  $\tilde{a}(0,0,0)$  level wave-function for combined transitions in CHI and CDI. Bending excitations have larger vibrational overlaps with the triplet state levels due to the large change in the bending angle in the triplet state, making their wave-functions overlap more into the singlet state manifold. Singlet combination vibrational levels containing a bending excitation have smaller FCF than bending levels, with the stretching levels having the least vibrational overlaps with the triplet origin. Vibrational parameters were calculated at the B3LYP/aug-cc-pVTZ level. Equivalent figures for CHBr/CDBr and CHCl/CDCl are also shown in Figure 44 and Figure 45 respectively. What can be summarized from the three figures is that; singlet bending vibrational modes have a significantly larger Frank-Condon overlap with the triplet levels than any other vibrational mode or combination vibrational modes.

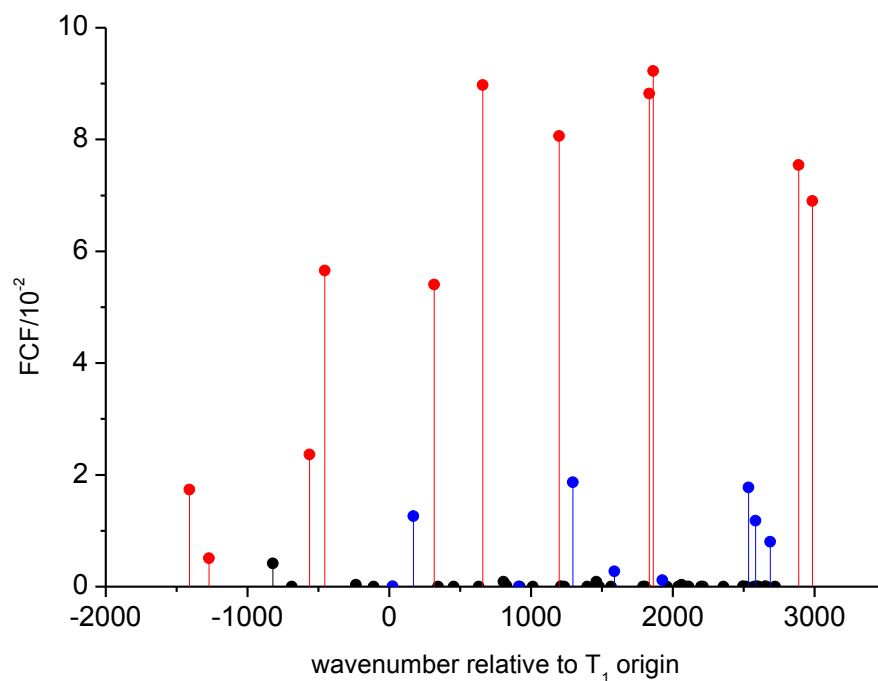


**Figure 43:** Frank-Condon factors for selected levels in CHI and CDI simulations. As expected, the largest FCF are between the interaction of the triplet origin with bending singlet levels (red bars). The blue bars represent combination levels involving C-I stretch ( $\nu_1 = 1$ ) and a bending mode ( $\nu_1=1,2,\dots$ ). The black bars represent C-H stretch and some combination vibrational levels involving the C-I and C-H stretching modes.

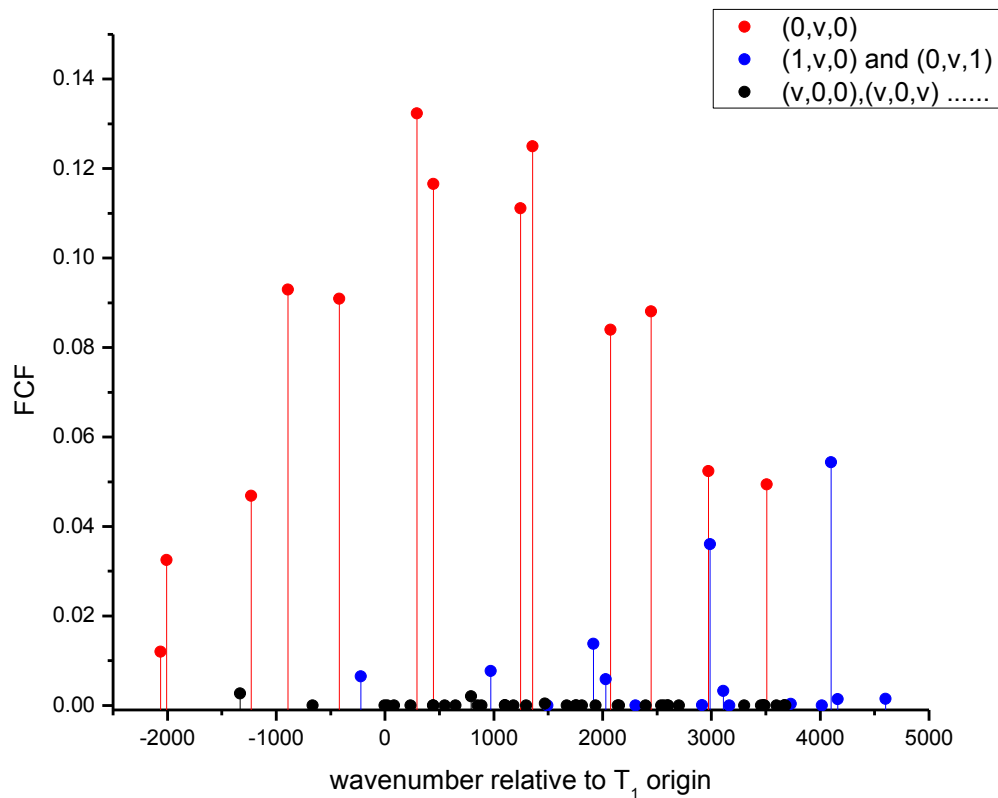


**Figure 44:** shows Frank-Condon factors for selected levels in CHBr and CDBr simulations. The tall red drop lines represent FCF between the triplet origin overlap with bending singlet levels. The blue drop lines represent combination levels involving C-I stretch ( $v_1 = 1$ ) and a bending mode ( $v_1=1,2\dots$ ). The black drop lines represent C-H stretch and some combination vibrational levels involving the C-I and C-H stretching modes.

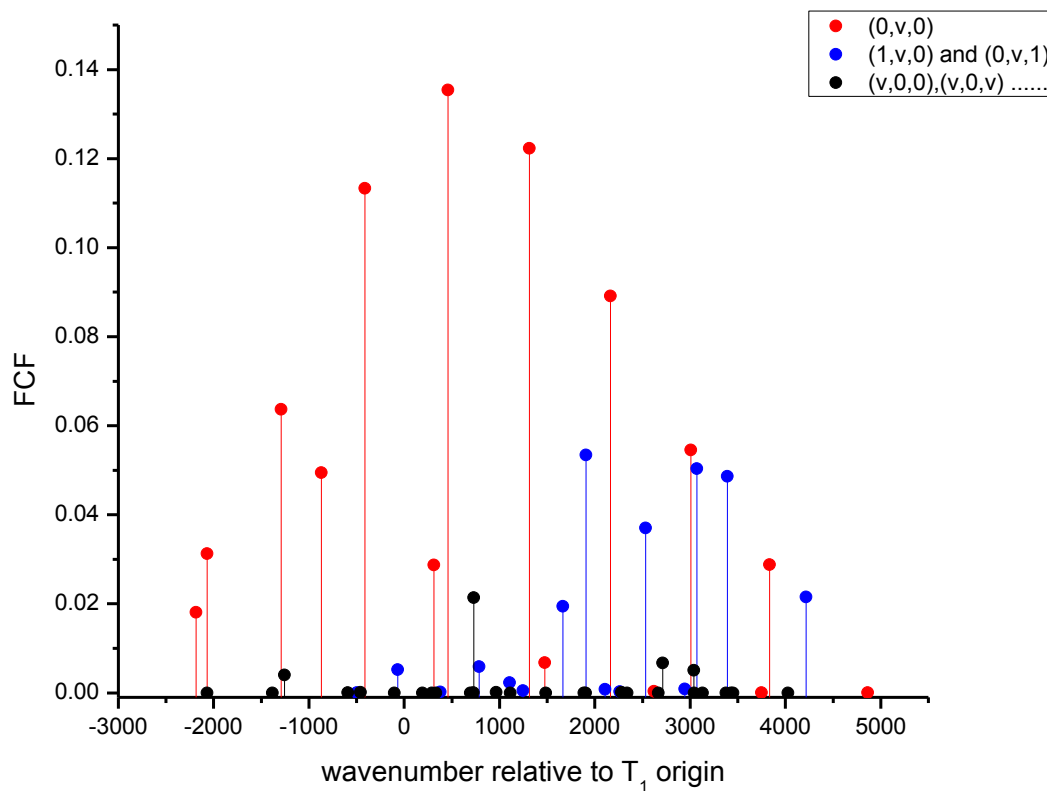


**Figure 45:** Frank-Condon factors for selected levels in CHCl and CDCl simulations. The largest FCF were predicted for the overlap between the triplet origin with bending singlet levels (red drop lines). The blue drop lines represent combination levels involving C-I stretch ( $\nu_1 = 1$ ) and a bending mode ( $\nu_1=1,2,\dots$ ). The black drop lines represent C-H stretch and some combination vibrational levels involving the C-I and C-H stretching modes.



## 5.9.5 MATRIX ELEMENTS: THE APPROXIMATION

A wave function  $\psi$  for a given atomic or molecular system is a mathematical function that contains all the information that is required to determine any measurable property of the system. Knowing the mathematical form of  $\psi$  enables one to compute the electronic, nuclear, spin configurations, and any experimental observable property like the electronic energy, dipole moment, nuclear geometry, transition probabilities between electronic states and so forth. To obtain a wave function of a system, the laws of quantum mechanics states that one must solve the Schrodinger wave equation:  $H\psi = E\psi$ .  $H$  is called the Hamiltonian and it corresponds to a mathematical operator for possible energies ( $E$ ) of the system, or the eigenvalues of the Hamiltonian operator. These energies can be the vibrational energies of molecular atoms, electronic energies of the molecule or spin energies of the electrons. The average value or expectation value, of an observable molecular property (energy of a state or the transition probability between two states) can be evaluated mathematically by the so called matrix element,  $\langle\psi|\hat{P}|\psi\rangle$ . In the case being studied here, the property of interest is energy ( $E$ ), so the operator  $P$  is given a special symbol  $H$ , for the Hamiltonian. The Hamiltonian is an energy operator; hence the matrix element  $\langle\psi|\hat{H}|\psi\rangle$  gives the quantum mechanical representation of the magnitude of the observable energies of a molecular system. In the calculations, diabatic approximation which assumes that nuclear motion evolves in a single potential energy surface was applied. In this approximation, the coupling of the electronic states is caused by the electron-nuclear interaction potential. This approximation requires the interaction be small as compared to the nuclear kinetic energy.<sup>199</sup>

Applying time dependent point of view, the condition is satisfied only if the nuclei move very fast thereby offering the electrons insufficient time to adjust to the nuclear motion. The electronic wavefunction is therefore assumed unchanged from the one before the motion. This makes diabatic approximations mathematically friendly as one only need to calculate the electronic wavefunction at a single and fixed nuclear coordinate. The motivation to assume diabatic potentials comes in the event that the Born-Oppenheimer approximation begins to fail towards degeneracy of the two interacting states. Figure 46 demonstrates the crossing between the  $S_0$  and  $T_1$  potential energy surfaces. It is known that in regions that are away from the avoided crossing, electrons are assumed to adjust instantaneously to the slower nuclei motion, in this case the adiabatic approximation holds. However, nuclear motion through an avoided crossing and other regions of strong spin-orbit coupling is assumed to occur quickly that the electronic configuration is entirely preserved.<sup>200</sup> The Born- Oppenheimer approximation is valid around the nuclear configuration where the nuclear kinetic energy is relatively small as compared to the energy gaps between the neighboring electronic states. If the electronic states cross, they are degenerate at that configuration and the diabatic approximation becomes more appropriate to apply.<sup>199</sup> If the coupling between the two electronic states is strong, the spin forbidden transitions or ‘surface hopping’ competes strongly with the spin allowed singlet-singlet transitions.<sup>201</sup> The probability of hopping from one surface to the other in the vicinity of the crossing region shown in Figure 46 is heavily controlled by the spin orbit matrix element  $H_{so}^{elec}$  between the two electronic wavefunctions. Spin orbit coupling maybe so strong that mixing of states is spread out over a broad range of geometries around the crossing region.<sup>201</sup>

*Spin orbit coupling matrix element approximation:*

$$\langle S_0(v_1, v_2, v_3) | \hat{H}_{so} | T_1(v_1, v_2, v_3) \rangle = H_{so}^{elec} \langle S_0(v_1, v_2, v_3) | T_1(v_1, v_2, v_3) \rangle$$

The notation  $(v_1, v_2, v_3)$  is used to label the vibrational states.

In accordance to this, assume the spin orbit coupling between the singlet state  $S_0(v_1, v_2, v_3)$  and the triplet state  $T_1(v_1, v_2, v_3)$  to follow the diabatic potential surfaces into the crossing region. The electronic spin orbit Hamiltonian fit parameter,  $H_{so}^{elec}$  can be factored. Only the electronic wavefunction at fixed nuclear configurations are needed to construct the coupling matrix, and no derivative coupling is required. Since each carbene species required on average a data set of more than 250 spin-orbit matrix elements, this approximation proved to be handy and reasonable. Support for this comes from previous studies on methylene ( $\text{CH}_2$ ) done by McKeller and co-workers<sup>161</sup> where spin orbit coupling varied slightly over a broad range of bond angles. They calculated the spin orbit coupling matrix element between the ground electronic state ( $\tilde{X}^3B_1$ ) and the first excited singlet electronic state ( $\tilde{a}^1A_1$ ) using microscopic spin orbit Hamiltonian<sup>161</sup>. Calculations were done at bond angles ranging from  $90^\circ$  to  $135.1^\circ$  thereby covering both equilibrium bond angles of the two electronic states and the crossing region. The spin orbit coupling was found to vary by less than 20%, showing that nuclear positions have little effect on the magnitude of the matrix elements.

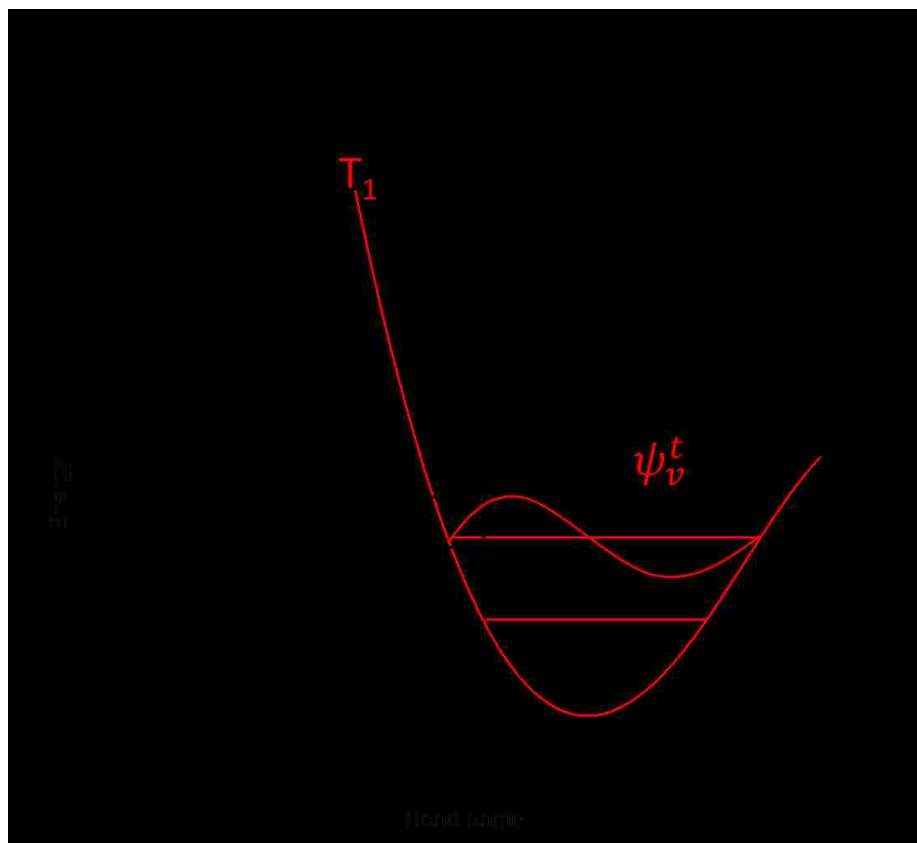


**Figure 46:** Schematic diabatic one dimensional picture of spin-orbit coupling in halocarbenes. The spin-orbit coupling is factorized into a purely electronic part and a nuclear part reflecting the vibrational overlap of the singlet and the triplet wavefunctions.

### 5.9.6 DUSCHINSKY EFFECT

The Frank-Condon factors between the ground singlet state and the excited triplet state were simulated with a full incorporation of the Duschinsky effect in Pqopher<sup>130</sup>. The Duschinsky effect arises when two electronic states have vibrational normal mode coordinate systems that are rotated and translated relative to each other. The consideration of this effect was found to give more reliable Frank-Condon spectral simulations.<sup>202-204</sup>

In a polyatomic molecule with  $3N-6$  ( $N$ =total number of atoms) vibrational degrees of freedom like the CHX/CDX carbenes, the vibrational and rotational coordinates in the ground electronic state are different from those in another excited electronic state. This difference is due to the different equilibrium geometries between the two electronic states. As was shown earlier, there is a large change in geometry from the singlet ground state ( $S_0$ ) to the excited triplet state ( $T_1$ ). The bond lengths does not make any significant change, but the bond angle increases by about  $30^\circ$ , leading to the change in the initial vibrational and rotational coordinates of the ground state in the triplet state. The effect of this difference in coordinates between the two states affects the vibronic transition intensity distribution. Duschinsky, made the first consideration of this effect in 1937,<sup>198</sup> and he pointed out the linear relation between the rotation of normal coordinates of two  $3N-6$  electronic states transforming as one irreducible representation. The normal modes of the  $T_1$  state ( $Q_{Ti}$ ) and the  $S_0$  state ( $Q_{Sj}$ ) are related through the Duschinsky transformation:<sup>198, 202</sup>

$$Q_{Ti} = \sum_j J_{ij} Q_{Sj} + D_i$$

where  $J$  is the Duschinsky rotation matrix and  $D$  is the displacement vector, which presents the displacement of the  $T_1$  potential surface with respect to that of  $S_0$ . This transformation matrix represents to what extent the normal modes of  $T_1$  are mixed based on the normal modes of  $S_0$ . The treatment of the normal modes rotation is crucial for a reliable calculation of spin-orbit matrix elements since matrix elements are generally a function of normal mode coordinates.

Figure 47. Shows the normal mode coordinates simulated for CDI molecule in Pgopher in the XY plane.

The shift in atomic Cartesian coordinates of the triplet state (red circles) in relation to the singlet state (black circles) is evident after the transformation. This was done for all the carbene species under study here.

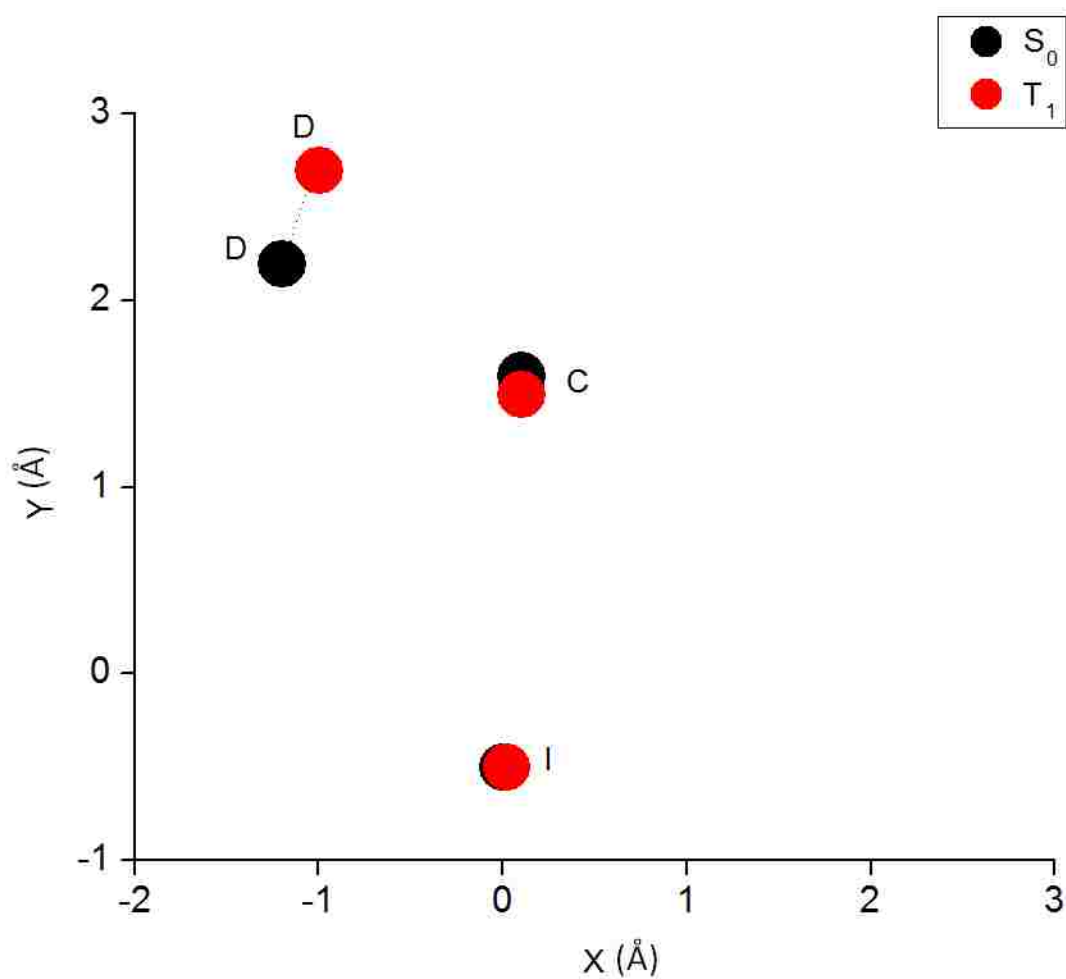


**Figure 47:** Shows an XY-plane Duschinsky transformation in CDI molecule. The dotted lines joins matching atoms or motions.

## 5.9.7 ANHARMONIC OSCILLATOR MODEL FIT

In nature, idealized situations break down and fail to describe linear equations of motion. A harmonic oscillator obeys Hooke's Law and is an idealized expression that assumes that a system displaced from equilibrium responds with a restoring force whose magnitude is proportional to the displacement. Anharmonic oscillation is described as when the restoring force is no longer proportional to the displacement and can be approximated to a harmonic oscillator and the anharmonicity can be calculated using perturbation theory. In these calculations, the vibrational energies were calculated using the anharmonic potential function called Dunham Expansion, and is of the form shown below. Previous studies<sup>168</sup> fitted the observed vibrational term energies to this function without the inclusion of spin-orbit coupling. As shall be shown later, there is an improved description of the vibrational term energies and assignments by the Dunham Expansion when spin orbit coupling is taken into account.

*Dunham Expansion approximation of term energies:*

$$G(v_1, v_2, v_3) = \omega_1^0 v_1 + \omega_2^0 v_2 + \omega_3^0 v_3 + x_{11}^0 v_1^2 + x_{22}^0 v_2^2 + x_{33}^0 v_3^2 + x_{12}^0 v_1 v_2 + x_{13}^0 v_1 v_3 + x_{23}^0 v_2 v_3$$

where  $\omega_1^0, \omega_2^0, \omega_3^0$  are harmonic frequencies,  $v_1, v_2, v_3$  are vibrational quantum numbers,  $x_{ij}$  are anharmonicity constants.

Notation  $(v_1, v_2, v_3)$ :  $v_1$  = C-X stretching mode, where X= Cl, Br, I;  $v_2$  = bending mode;  $v_3$  = C-H or C-D stretching mode.

### 5.9.8 SETTING UP THE HAMILTONIAN MATRIX

The Hamiltonian matrix requires initial guess diagonal matrix elements or eigenvalues, in this case, singlet and triplet energy levels as shown in Figure 48. The spin orbit matrix elements, simulated from Pgoopher, are also incorporated into the matrix as shown in the Figure 48. Jacobian algorithms for matrix diagonalisation was employed in Microsoft excel to obtain a fully diagonal matrix. The same process was also repeated using Matlab which is faster over very large matrices. The matrices set up were as large as 88 X 88 for systems like CHCl with large observed data to fit. Carrying out diagonalisation iterations using the Jacobi scheme returns a diagonal matrix, with the non-zero elements as the term energies. Microsoft Excel and Matlab was used to fit the calculated term energies to the observed term energies.

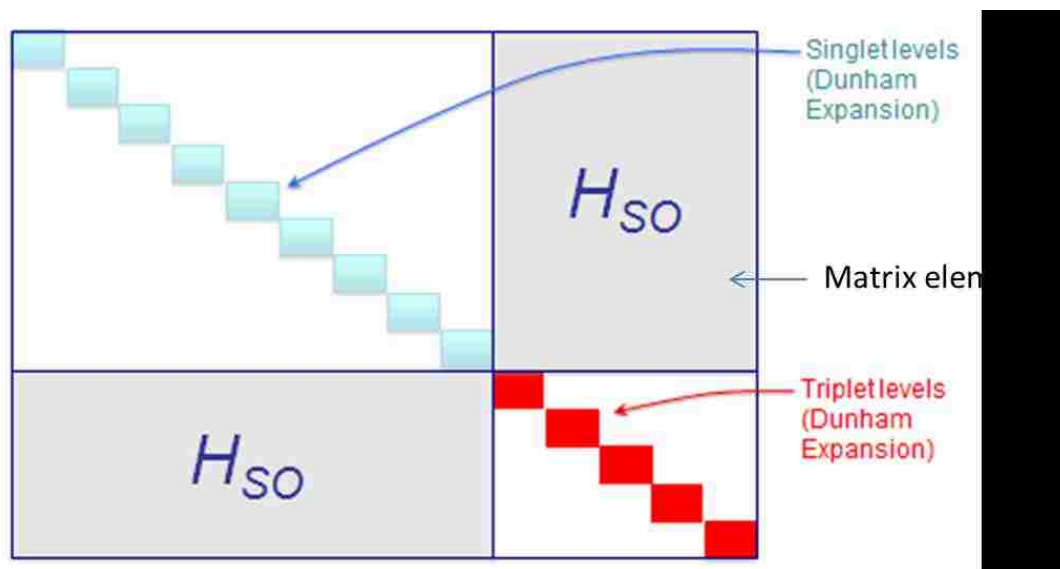


**Figure 48:** Setting up of the Hamiltonian matrix. The initial singlet and triplet eigenvalues are approximated by the Dunham Expansion. The matrix elements are obtained by simulation from Pgoopher and multiplying by a spin-orbit coupling fitting parameter.



## CHAPTER 6. CHI AND CDI

## 6.1 CHI SVL EMISSION SPECTRUM

Previous studies in other halocarbenes have shown that mostly bending levels and combination levels that contain a bending mode are perturbed due to better vibrational overlap with the triplet levels.<sup>166, 167</sup> The calculation results are displayed in Table 4, spin orbit coupling between the two low lying electronic states ( $\tilde{X}^1A'$  and the  $\tilde{a}^3A''$ ) was taken into account. The triplet origin was predicted to be at  $1409\text{cm}^{-1}$  which is in very good agreement with the observed SVL emission spectrum.<sup>166</sup> Also the singlet – triplet energy gap in CHI was predicted to be  $1392\text{cm}^{-1}$ . A number of values for the singlet – triplet energy gap have been proposed that ranges from as low as  $0.8\text{ kcal mol}^{-1}$  to about  $6.3\text{ kcal mol}^{-1}$  ( $280\text{cm}^{-1} - 2200\text{cm}^{-1}$ ).<sup>137, 146, 154, 161, 166, 173, 196</sup> This was in good agreement with the SVL emission results,<sup>166, 167</sup> and most importantly, spin orbit coupling was taken into account. Bending states are severely perturbed, with the lowest bending level  $\tilde{X}(0,1,0)$  lying at  $948\text{cm}^{-1}$ , which is about  $100\text{ cm}^{-1}$  below theoretical prediction  $1048\text{ cm}^{-1}$ .

## 6.2 CHI VIBRATIONAL ENERGY LEVEL ASSIGNMENTS

Table 4 lists the assigned  $\tilde{X}$  and  $\tilde{a}$  state levels. A total of 14 singlet state levels and 5 triplet state levels were fit to 19 SVL emission observed levels previously obtained.<sup>166, 167</sup>

The levels produced a good fit with a mean averaged deviation of  $2.5\text{cm}^{-1}$ , which is in good agreement with an experimental standard deviation of about  $2\text{cm}^{-1}$ . 25  $S_0$  energy levels were calculated, going up to  $\tilde{X}(0,4,0)$  at  $4394\text{cm}^{-1}$  and 11  $T_1$  energy levels going up to level  $\tilde{a}(0,3,0)$  predicted at  $3850\text{cm}^{-1}$ . Shown in Table4 are singlet and triplet levels that were fit to the observed levels.

### 6.3 FIT PARAMETERS

C-H stretch vibrational frequency was not fit in the calculations since the experimental data used here did not observe any C-H stretching progression in the emission spectra. A comparison of the fitted to the calculated vibrational frequencies reveals how accurate the calculations are since the fitted frequencies does not vary much from the *ab initio* calculated frequencies using B3LYP/Sadlej-pVTZ level of theory. From previous studies, this level of theory has proved more accurate in determining the harmonic vibrational frequencies of halocarbenes. Only  $x_{11}$  was included in the fitting, the rest of the anharmonicity constants in the Dunham Expansion given earlier were zero and are not shown here. A singlet –triplet gap of  $1392\text{cm}^{-1}$  was obtained with a fitting electronic spin orbit element of  $731\text{cm}^{-1}$ .

**Table 4:** Assignments of the calculated and mixed SVL emission spectra energy levels for CHI. Energies are in  $\text{cm}^{-1}$ .

Energy Level	<sup>a</sup> Fitted (with SOC)	Calculated (No SOC)	<sup>b</sup> Observed	<sup>c</sup> F. -O.
(0,0,0)	0	0	0	0
(1,0,0)	589	572	591	-2
(0,1,0)	955	1056	948	7
(2,0,0)	1174	1140	1176	-2
<b>(0,0,0)</b>	<b>1409</b>	<b>1392</b>	<b>1407</b>	<b>2</b>
(1,1,0)	1579	1627	1582	-3
(3,0,0)	1754	1704	1754	0
<b>(1,0,0)</b>	<b>1971</b>	<b>2007</b>	<b>1975</b>	<b>-4</b>
(0,2,0)	2069	2111	2070	-1
(2,1,0)	2215	2196	2217	-2
(4,0,0)	2329	2265	2326	4
<b>(2,0,0)</b>	<b>2583</b>	<b>2623</b>	<b>2584</b>	<b>-1</b>
(1,2,0)	2705	2683	2704	1
(3,1,0)	2857	2760	2852	5
(5,0,0)	2889	2822	2891	-3
<b>(1,1,0)</b>	<b>3022</b>	<b>2812</b>	<b>3022</b>	<b>0</b>
<b>(0,2,0)</b>	<b>3168</b>	<b>3001</b>	<b>3168</b>	<b>0</b>
(0,3,0)	3270	3167	3275	-5
(2,2,0)	3335	3251	3330	5
<b>MAD</b>				<b>2.5</b>

<sup>a</sup>Fitted(with SOC) singlet and triplet energy levels,

<sup>b</sup> Stimulated emission pumping and SVL emission energy levels from reference <sup>166, 167</sup>

<sup>c</sup>MAD- mean average deviation

<sup>d</sup>F. -O. – Fitted – Observed

**Table 5:** Vibrational frequencies in  $\text{cm}^{-1}$ .

Species	Mode	<sup>a</sup> Fit Frequency	<sup>b</sup> Calculated Frequency
CHI ( $S_0$ )	C-H Stretch	2825(11)	2896.5
	Bend	1055(1)	1050.0
	C-I stretch	574(1)	587.8
CHI ( $T_1$ )	C-H Stretch	3132 <sup>c</sup>	3131.8
	Bend	802(5)	799.0
	C-I stretch	618(3)	642.9

<sup>a</sup>One standard deviation in parenthesis (right justified)

<sup>b</sup>Unscaled vibrational frequencies calculated at B3LYP/Sadlej-pVTZ level

<sup>c</sup>anharmonic frequency value

**Table 6:** Shows the fit parameters obtained during the fitting of the energy levels to the experimental values.

Fit Parameters/ $\text{cm}^{-1}$	
$H_{SO}^{elec}$	736(9)
$\Delta E_{ST}$	1392(4)
$x_{11}$	-1.9(0.3)

$\Delta E_{ST}$  is the singlet-triplet energy gap

$x_{11}$  is the anharmonic constant in the singlet state.

## 6.4 ENERGY LEVEL DIAGRAM

In Figure 49, the calculated and the observed energy levels for the CHI system are represented on a stick energy diagram. Here, the calculated energy levels of both the singlet and triplet state are being compared to the mixed experimental energy levels obtained from reference<sup>167</sup> and are in the middle column. The calculated energy levels incorporated spin orbit coupling between the ground singlet state and the low lying triplet state. The incorporation of the spin orbit coupling in the calculated energy levels has helped greatly in the making of firm assignments to the observed mixed levels. Most of the observed energy singlet levels are perturbed by a particular triplet level that lies nearby. Examples includes the triplet origin level  $\tilde{a}(0,0,0)$  at  $1409\text{cm}^{-1}$  that lies right in between two singlet levels,  $\tilde{X}(2,0,0)$  and  $\tilde{X}(1,1,0)$ .  $\tilde{a}(1,0,0)$  lies between the  $\tilde{X}(3,0,0)$  and  $\tilde{X}(0,2,0)$  levels. Spin orbit interaction effect would cause the lower levels  $\tilde{X}(2,0,0)$  and  $\tilde{X}(3,0,0)$  to be shifted down and the upper levels  $\tilde{X}(1,1,0)$  and  $\tilde{X}(0,2,0)$  to be shifted up by a few wavenumbers with respect to the triplet level position. Regardless all the perturbations that exists in the system, the calculations have accurately accounted for this and firmly predicted the positions perturbed levels. Pervious attempt to assign these perturbed levels wasn't an easy task.<sup>167</sup>

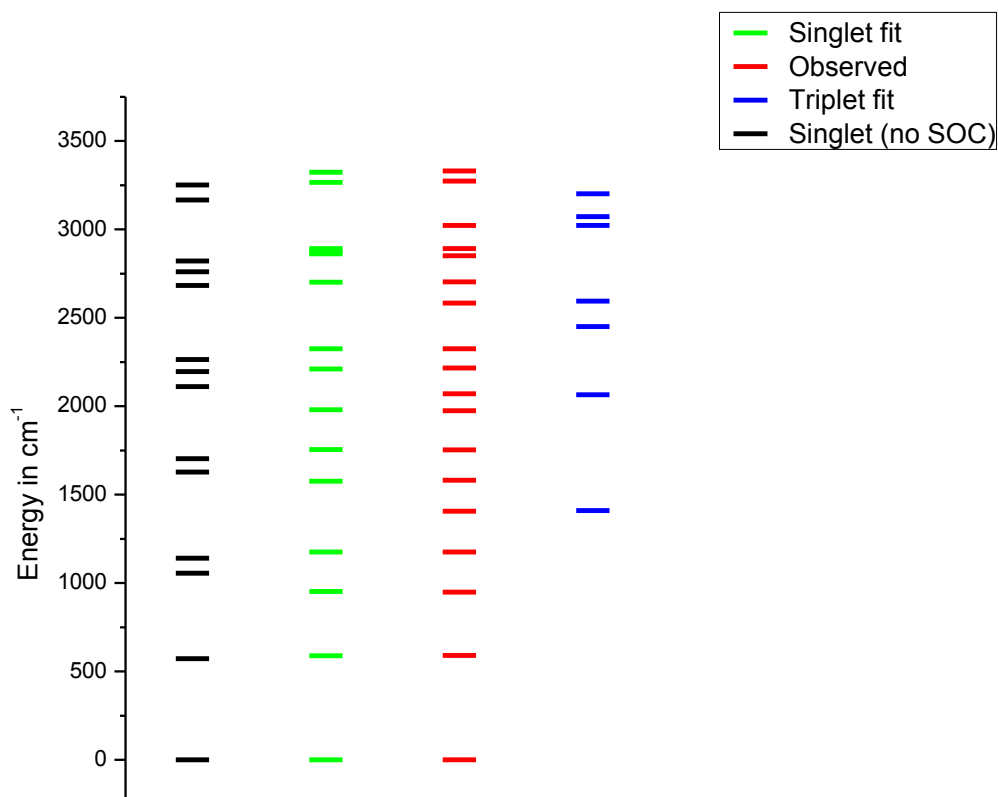


**Figure 49:** Shows the stick energy diagram of the calculated and observed term energies for CHI system. The first black column displays some calculated singlet levels without spin orbit coupling. The second green column shows some fitted singlet levels, and fitted triplet levels are in the last blue column. The third red column displays mixed observed levels from reference<sup>166, 167</sup>

## 6.5 CDI VIBRATIONAL ENERGY LEVEL ASSIGNMENTS

The assignments on the CDI system was based on the fitting to the experimental SVL emission lines.<sup>167</sup> A triplet origin  $\tilde{a}(0,0,0)$  was deduced to be located at  $1268\text{cm}^{-1}$ , above which singlet state energy levels become severely perturbed by the presence of the triplet levels. The assignments of the  $\tilde{a}(0,0,0)$  and lower energy levels agree very well with recent calculations and assignments shown in Table 7.

The  $\tilde{a}(0,0,0)$  was calculated to be lying at  $1273\text{cm}^{-1}$  above the vibrationless singlet state origin. The singlet fundamental C-I stretching frequency was obtained to be  $583\text{cm}^{-1}$ , a difference of  $1\text{cm}^{-1}$  from the observed value of  $582\text{cm}^{-1}$ . Also the triplet fundamental C-I stretching frequency was calculated to be at  $1874\text{cm}^{-1}$  but observed to be about  $2\text{cm}^{-1}$  lower at  $1872\text{cm}^{-1}$ . A total of 32 singlet state and 11 triplet state vibrational levels were calculated and assigned, but shown in Table 7 are only those levels that could be fit to the observed levels with a mean averaged deviation of  $4.0\text{cm}^{-1}$ .

**Table 7:** Vibrational level assignments for CDI. Energies are in  $\text{cm}^{-1}$ .

Level	Fitted (with SOC)	Calculated (No SOC)	<sup>a</sup> Observed	<sup>b</sup> F.-O.
(0,0,0)	0	0	0	0
(1,0,0)	583	563	582	1
(0,1,0)	711	793	722	-11
(2,0,0)	1161	1124	1156	5
<b>(0,0,0)</b>	<b>1273</b>	<b>1395</b>	<b>1268</b>	<b>5</b>
(1,1,0)	1296	1357	1304	-8
(0,2,0)	1588	1586	1586	2
(3,0,0)	1726	1681	1724	2
<b>(1,0,0)</b>	<b>1874</b>	<b>1956</b>	<b>1872</b>	<b>2</b>
(0,0,1)	2096	2057	2087	9
(1,2,0)	2187	2150	2200	-13
(4,0,0)	2286	2236	2286	0
(0,3,0)	2473	2380	2477	-4
(2,2,0)	2479	2710	2477	2
(1,0,1)	2670	2620	2666	4
<b>(1,1,0)</b>	<b>2797</b>	<b>2596</b>	<b>2800</b>	<b>-3</b>
(5,0,0)	2838	2787	2836	2
(0,1,1)	2870	2851	2869	1
(1,3,0)	3065	2943	3057	8
(4,1,0)	3078	3029	3072	6
<b>(3,0,0)</b>	<b>3243</b>	<b>3314</b>	<b>3240</b>	<b>3</b>
(6,0,0)	3387	3337	3391	-4
<b>(1,2,0)</b>	<b>3394</b>	<b>3157</b>	<b>3391</b>	<b>3</b>
<sup>d</sup> MAD				<b>4.0</b>

<sup>a</sup>SVL emission energy levels from reference <sup>167</sup>



## 6.6 FIT PARAMETERS

The computed vibrational frequencies for both electronic states are summarized in Table 7. Again, C-D stretch is not included in the fitting since no C-D stretch progression was obtained from the SVL emission spectra following the excitation of several  $S_0$  bands. The fitted frequencies did not vary too much from the *ab initio* calculated harmonic frequencies. One can also notice the re-ordering of the bending mode with the C-I stretch frequencies in the CDI triplet. Only the diagonal anharmonicity constant  $x_{11}$  was included in the fitting, the rest were insignificant. A singlet –triplet gap of  $1386\text{cm}^{-1}$  was obtained with a fitting electronic spin orbit coupling constant of  $728\text{cm}^{-1}$ . The singlet – triplet energy gap value of  $1386\text{cm}^{-1}$  is in good agreement with previous experimental values<sup>167</sup> of  $4.1\text{kcal mol}^{-1}(1435\text{cm}^{-1})$ .

**Table 8:** Vibrational frequencies in  $\text{cm}^{-1}$ 

Species	Mode	<sup>a</sup> Fit Frequency	<sup>b</sup> Calculated Frequency
CDI ( $S_0$ )	C-D Stretch	2058(2)	2121
	Bend	793(2)	775
	C-I stretch	565(1)	574
CDI ( $T_1$ )	C-D Stretch	2061(10) <sup>c</sup>	2314.8
	Bend	562(5)	576.0
	C-I stretch	641(4)	648.0

<sup>a</sup>One standard deviation in parenthesis (right justified)

<sup>b</sup>Unscaled vibrational frequencies calculated at B3LYP/Sadlej-pVTZ level

<sup>c</sup>anharmonic frequency value

**Table 9:** Shows the fit parameters obtained during the fitting of the energy levels to the experimental values for CDI.

Fit Parameters/cm <sup>-1</sup>	
$H_{so}^{elec}$	728(4)
$\Delta E_{ST}$	1386(4)
$x_{11}$	-0.7(0.1)

### 6.7 ENERGY LEVEL DIAGRAM FOR CDI

Figure 50 is an energy level diagram that is reflecting the data displayed in Table 7 for CDI isotopomer. It can be noted that for singlet levels lying below the triplet origin, there is a very good match with the observed levels. Evidence of levels becoming perturbed starts showing up around and above the triplet origin position. The singlet levels become mixed with the triplet levels to a different extent. The extent of the interaction of the singlet and triplet levels heavily depends on the electronic spin – orbit coupling element that exists between the two states. The calculations did a very good job by incorporating this spin –orbit coupling and predicted the positions of the perturbed levels. This is a great improvement from the Dunham Expansion fit employed earlier without including spin-orbit coupling for most of the species studied. Previously higher energy levels could not be firmly assigned due to this severe shift in positions. Again, due to improved vibrational overlaps, all levels associated with the bending mode are perturbed the most as compared to stretching vibrational mode levels. For example from Figure 50 the  $\tilde{a}(0,0,0)$  is calculated to be at  $1273\text{cm}^{-1}$ , that is, right in-between the  $\tilde{X}(2,0,0)$  and  $\tilde{X}(1,1,0)$  singlet levels.

The diagram clearly shows this region with the C-I stretching level  $\tilde{X}(2,0,0)$  unperturbed regardless of close proximity and  $\tilde{X}(1,1,0)$  level shifted by about  $13\text{cm}^{-1}$  from the observed perturbed position.

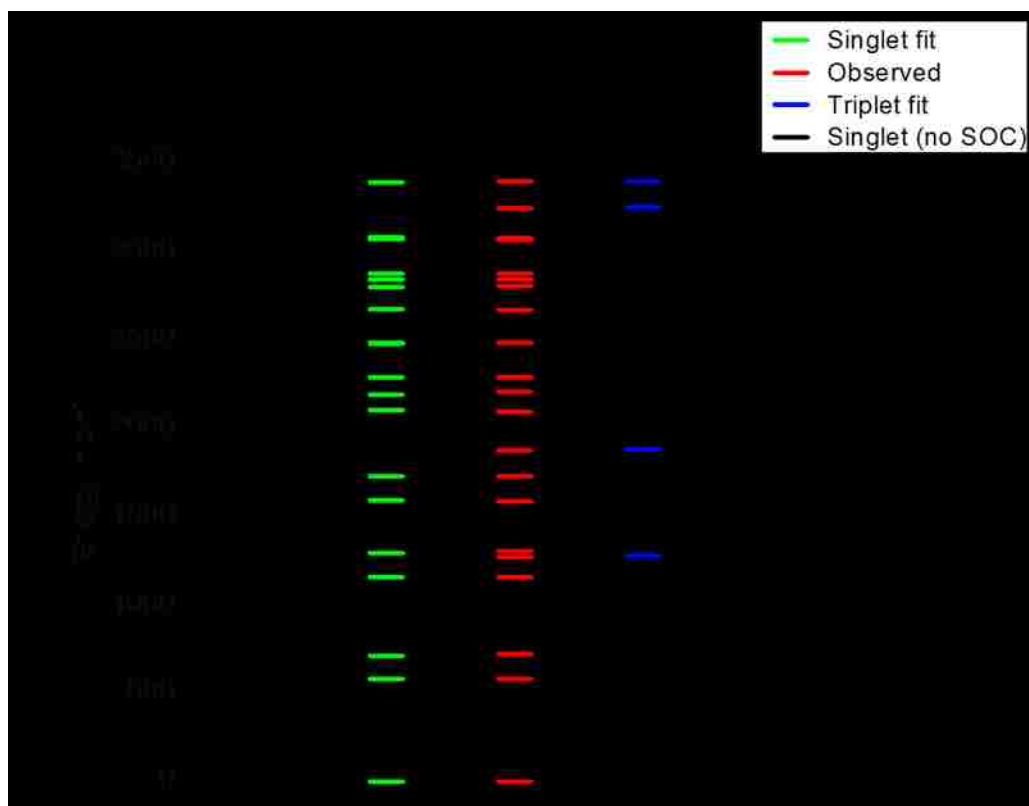


**Figure 50:** The stick energy diagram of the calculated and observed term energies for the CDI system. The first black column displays some calculated singlet levels without spin orbit coupling. The second green column shows some fitted singlet levels, and fitted triplet levels are in the last blue column. The third red column displays mixed observed levels from reference<sup>167</sup>

## CHAPTER 7. CHBr AND CDBr

## 7.1 CHBR VIBRATIONAL LEVEL ASSIGNMENTS

Deselnicu and co-workers obtained a dispersed fluorescence (DF) spectra for CHBr by pumping various levels in the  $S_1$  excited state.<sup>157</sup> In their work, they assigned quite a number of lower  $\tilde{X}$  levels and a few  $\tilde{a}$  levels. The current calculations however have managed to confirm the earlier assignments made in references<sup>141, 193</sup> and then go a step further in assigning the most of the higher energy levels which were difficult to assign in the presence of severe perturbations arising from the spin-orbit coupling of the two low lying electronic states. As expected, the bending levels were the most perturbed as compared to the stretching modes. The observed C-Br stretch progression have a fundamental vibrational frequency of  $677\text{cm}^{-1}$ . Bending level  $\tilde{X}(0,1,0)$  is observed at  $1119\text{cm}^{-1}$ , first C-H stretching level  $\tilde{X}(0,0,1)$  at  $2802\text{cm}^{-1}$ . These calculations predicted the positions of all these perturbed levels with decent accuracy as can be seen in Table 10. A total of 56 singlet state levels and 32 triplet state levels were calculated in the matrix diagonalization scheme. In Table 10 total of 30  $\tilde{X}$  levels and 7  $\tilde{a}$  levels were fit to the observed mixed levels, with a mean averaged deviation of about  $3\text{cm}^{-1}$ . The experimental fit standard deviation was  $16\text{cm}^{-1}$ , hence this is a great improvement in the fitting and assignment of the levels. The triplet origin  $\tilde{a}(0,0,0)$  level is predicted to be  $2008\text{cm}^{-1}$ , a  $2\text{cm}^{-1}$  shift from the observed value of  $2006\text{cm}^{-1}$ . The triplet state levels does not only cause perturbations to the singlet state levels without themselves being perturbed also from the spin orbit interaction of the two states.

The  $\tilde{a}(0,0,0)$  interacts with the nearby bending singlet levels , (0,1,0), (1,1,0), (0,2,0) and (2,1,0) more than it does with the degenerate (3,0,0) level . The larger change in geometry with the bending vibrations than the one caused by the stretching vibrations leads to a more improved Frank Condon Factor of the bending modes with the background triplet state levels.

## 7.2 FIT PARAMETERS

Table 11 compares the fitted vibrational frequencies to those from *ab initio* DFT calculations done at B3LYP/aug-cc-pVTZ level of theory. The C-Br stretch and bending modes are in relatively good agreement with the DFT calculated vibrational frequency modes, with only the C-H deviating by about  $85\text{cm}^{-1}$ . Unlike in CDI triplet state, there is no re-ordering of vibrational frequencies in CHBr triplet state. The computed fit parameters that include electronic spin –orbit element, the singlet-triplet energy gap  $\Delta E_{\text{ST}}$ , and the anharmonicity constants for both electronic states are summarized in Table 12. The  $H_{S_0}^{elec}$  was predicted to be  $354\text{cm}^{-1}$ , which is in good agreement with the  $330\text{cm}^{-1}$  obtained in reference<sup>141</sup>. The  $\Delta E_{\text{ST}}$  was calculated to be  $2059\text{cm}^{-1}$ , agreeing very well with other previous studies.<sup>141, 193</sup>  $x_{33}$  anharmonicity constant for the singlet state was set to zero because it could not be determined accurately in the fitting due to the absence of higher vibrational quantum numbers in the C-H stretch mode. A lot more anharmonicity constants for the triplet were excluded since only a first few triplet levels were dealt with in the fitting, which makes  $x_{11}$  the all-important parameter.

**Table 10:** Vibrational levels assignments for CHBr. Energies are in  $\text{cm}^{-1}$ .

Level	Fitted (with SOC)	Calculated (No SOC)	<sup>a</sup> Observed	<sup>b</sup> F. - O.
(0,0,0)	0	0	0	0
(1,0,0)	675	674	677	-2
(0,1,0)	1115	1126	1119	-4
(2,0,0)	1342	1340	1345	-3
(1,1,0)	1786	1797	1785	1
(3,0,0)	2003	1998	2006	-3
<b>(0,0,0)</b>	<b>2008</b>	<b>2060</b>	<b>2006</b>	<b>2</b>
(0,2,0)	2302	2241	2314	-12
(2,1,0)	2452	2460	2447	5
(4,0,0)	2657	2648	2660	-3
<b>(1,0,0)</b>	<b>2742</b>	<b>2810</b>	<b>2741</b>	<b>1</b>
(0,0,1)	2799	2796	2802	-3
(1,2,0)	2981	2909	2971	10
<b>(0,1,0)</b>	<b>3000</b>	<b>2940</b>	<b>3003</b>	<b>-3</b>
(3,1,0)	3110	3116	3104	6
(5,0,0)	3305	3290	3305	0
(0,3,0)	3364	3346	3362	2
<b>(2,0,0)</b>	<b>3459</b>	<b>3556</b>	<b>3464</b>	<b>-5</b>
(1,0,1)	3477	3470	3479	-2
(4,1,0)	3761	3763	3756	5
<b>(3,0,0)</b>	<b>3835</b>	<b>4298</b>	<b>3838</b>	<b>-3</b>
(0,1,1)	3923	3915	3917	6
(6,0,0)	3945	3924	3946	-1
(1,3,0)	4037	4011	4032	5
(2,0,1)	4147	4135	4146	1
(3,2,0)	4158	4222	4162	-4
(0,4,0)	4453	4439	4453	0
<b>(4,0,0)</b>	<b>4564</b>	<b>5035</b>	<b>4564</b>	<b>0</b>
(7,0,0)	4573	4550	4573	0
(2,3,0)	4710	4668	4715	-5
(3,0,1)	4811	4792	4809	2
(4,2,0)	4836	4866	4837	-1

<b>(2,2,0)</b>	<b>5220</b>	<b>5317</b>	<b>5217</b>	<b>3</b>
(4,0,1)	5464	5441	5462	2
(3,1,1)	5917	5902	5922	-5
(0,3,1)	6107	6118	6107	0
(5,3,0)	6570	6591	6570	0
<b><sup>c</sup>MAD</b>				<b>3</b>

<sup>a</sup>SVL emission energy levels from reference <sup>167</sup>.

**Table 11:** CHBr vibrational frequencies in  $\text{cm}^{-1}$

Species	Mode	<sup>a</sup> Fit Frequency	<sup>b</sup> Calculated Frequency
CHBr ( $S_0$ )	C-H Stretch	2802.2(1)	2881
	Bend	1123.3(1)	1147
	C-Br stretch	679.2(1)	686
CHBr ( $T_1$ )	C-H Stretch	3146 <sup>c</sup>	3147
	Bend	879.0(4)	916
	C-Br stretch	748.1(2)	747

<sup>a</sup>One standard deviation in parenthesis (right justified)

<sup>b</sup>Unscaled vibrational frequencies calculated at B3LYP/aug-cc-pVTZ level

<sup>c</sup>Anharmonic value

**Table 12:** Fit parameters for CHBr.

Fit Parameters/cm <sup>-1</sup>	
$H_{so}^{elec}$	354(3)
$\Delta E_{ST}$	2059(2)
$\tilde{X}$	
$x_{11}$	-3.9(0.1)
$x_{22}$	-5.9(0.3)
$x_{33}$	-2.5(0.6)
$x_{12}$	-3.4(0.3)
$x_{13}$	-2.0(0.1)
$x_{23}$	-21.9(1.2)
$\tilde{a}$	
$x_{11}$	-5.4(1.1)

### 7.3 ENERGY LEVEL DIAGRAM FOR CHBr

From literature<sup>141</sup>, it was shown how the triplet origin  $\tilde{a}(0,0,0)$  primarily interacts with the nearby singlet bending state levels, shifting them by as much as 100cm<sup>-1</sup>. Singlet levels  $\tilde{X}(0,1,0)$ ,  $\tilde{X}(1,1,0)$ ,  $\tilde{X}(0,2,0)$  experience more perturbation from  $\tilde{a}(0,0,0)$ , whilst  $\tilde{X}(4,0,0)$  and  $\tilde{X}(0,0,1)$  interacts with  $\tilde{a}(1,0,0)$  according to the size of the spin orbit matrix element that exist between them and the perturbing level.  $\tilde{X}(1,2,0)$ ,  $\tilde{X}(3,1,0)$  interacts with the  $\tilde{a}(0,1,0)$  level and the shift in positions is expected to be larger than the stretching level due to better vibrational overlaps between bending levels. At higher energies, previous studies could not assign the observed levels due to intense and selective perturbations. They needed some serious deperturbation analysis in-order to confidently assign the higher energy levels.



At higher energy regions, vibrational level spacings become narrower, hence the inclusion of anharmonicity constants in the fitting becomes essential. The matrix diagonalisation scheme with incorporation of the spin orbit coupling can accurately predict up to any energy level one wishes. Most previously observed but unassigned levels in ref<sup>41</sup> have been firmly assigned for CHBr as can be seen in Figure 51. The lower lying singlet energy levels that are below the  $\tilde{a}(0,0,0)$  can easily be fitted and assigned without any difficulties because they are not perturbed by any significant margin. However, as soon as the triplet levels comes into play, starting from the  $\tilde{a}(0,0,0)$  going up, there is a pronounced shift in positions of both electronic state levels. To help visualize the magnitude of the shifts, Figure 52 is a zoom-in region of upper lying vibrational levels indicated in Figure 51. The calculated energy levels incorporating spin orbit coupling (second and last columns of Figure 51 and Figure 52) could easily be assigned to the experimentally observed energy levels as indicated by the arrows. The corresponding energy levels calculated whilst ignoring the spin orbit coupling by using the Dunham Expansion (first column) are perturbed from as little as  $10\text{cm}^{-1}$  to hundreds of wavenumbers. This trend was observed all the halocarbene species. These calculations make a great improvement on fitting the observed data firmly as compared to the Dunham expansion which does not incorporate spin orbit coupling.

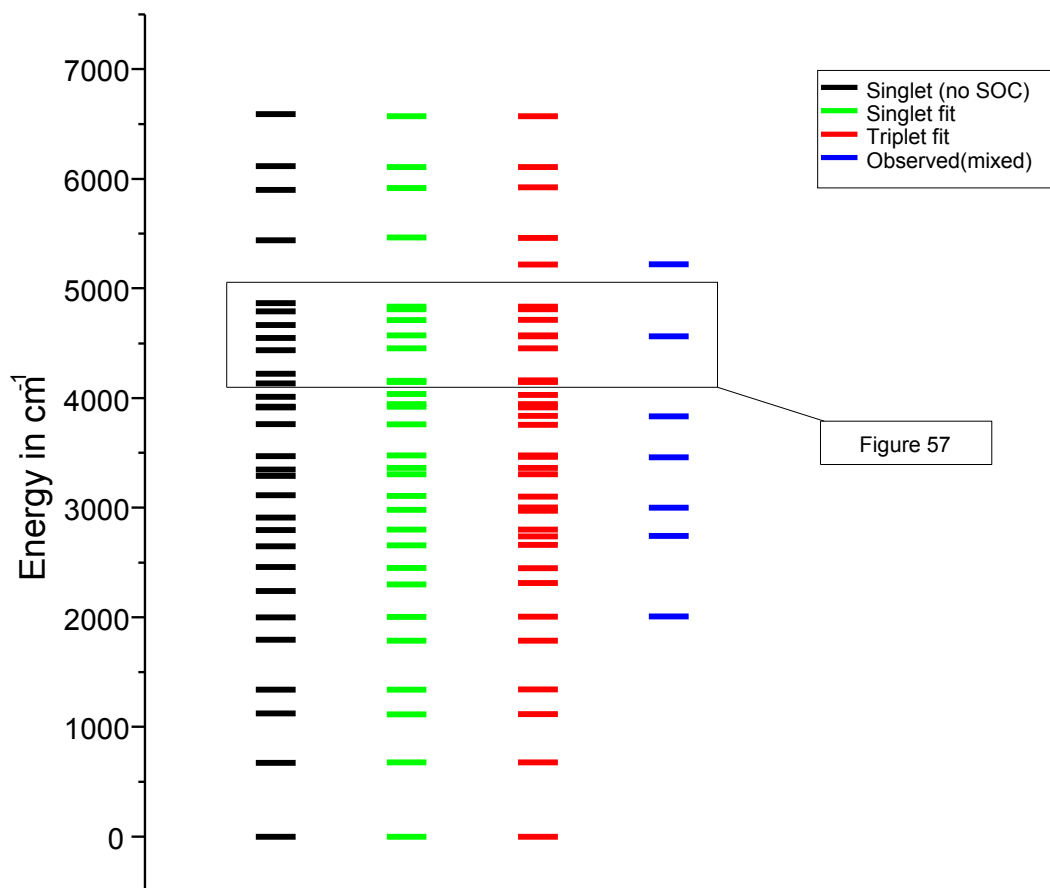


**Figure 51:** CHBr term energy diagram which compares the predicted singlet and triplet level positions to the experimental mixed levels. The first black column displays calculated singlet energy levels without spin orbit coupling. The second and last column shows some fitted singlet and triplet energy levels that incorporated spin orbit coupling respectively. The third column displays mixed observed levels from reference <sup>141</sup>.

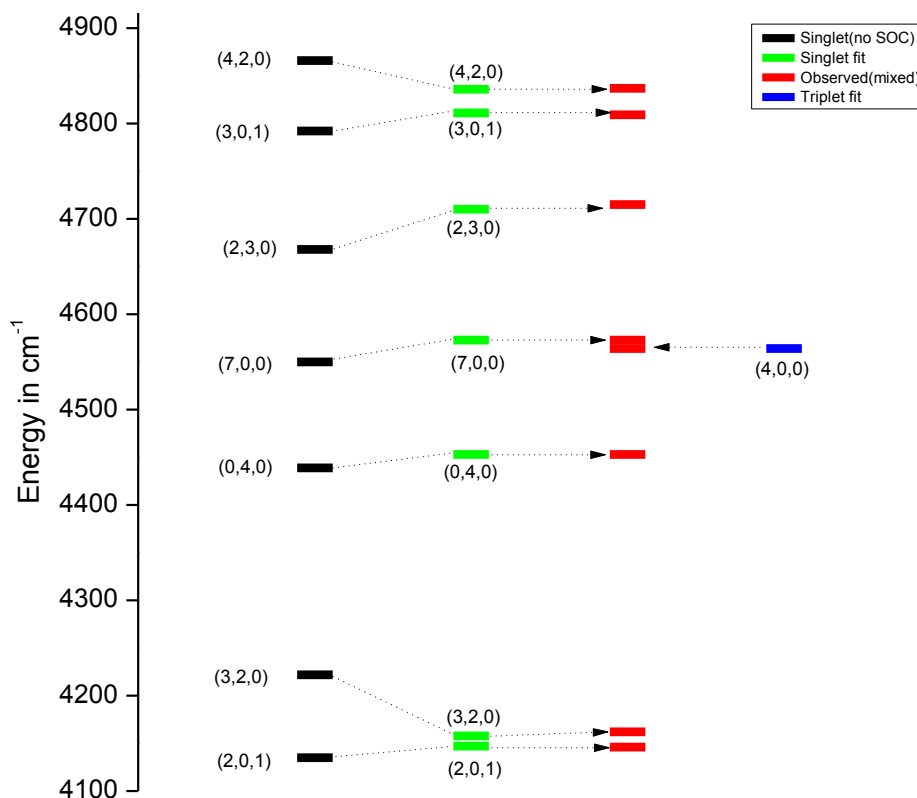


**Figure 52:** A zoom-in CHBr term energy diagram on upper lying levels in Figure 51. The region is where perturbations are most intense.

#### 7.4 CDBr VIBRATIONAL ENERGY LEVEL ASSIGNMENTS

More than 60 vibrational levels were calculated and Table 13 lists 35 assigned levels that include 6 triplet levels embedded in the singlet states manifold. Again here there is evidence of both the selective perturbation of the bending levels. The  $\tilde{X}(0,2,0)$  was fit with a  $7\text{cm}^{-1}$  deviation from the observed frequency whilst the C-D stretching level  $\tilde{X}(0,0,1)$  observed at  $2087\text{cm}^{-1}$  and only  $22\text{cm}^{-1}$  from the triplet origin level is not shifted.

This is consistent with the small spin orbit matrix elements calculated for such levels with the triplet levels. The calculations and the fitting is a big improvement from the work of Yu that had a  $70\text{cm}^{-1}$  standard deviation, Tao had a standard deviation of about  $39\text{cm}^{-1}$ , the calculated deviation in this study is  $3\text{cm}^{-1}$ . Chang and coworkers<sup>141</sup> approximated their errors to be  $\pm 4\text{cm}^{-1}$ . This improvement is credited to the treatment of spin orbit coupling between singlet and triplet states which, just like for CHBr tend to perturb each other. As can be noticed from the SVL emission spectrum for CHBr/CDBr, the intensity of the triplet states are smaller than those from CHI/CDI as the spin orbit element drops from  $736\text{cm}^{-1}$  to  $354\text{cm}^{-1}$ , thereby significantly reducing the degree of interaction between the singlet and triplet states, less intensity is borrowed to the singlet-triplet transition.

**Table 13:** Vibrational levels assignments for CDBr. Energies are in  $\text{cm}^{-1}$ .

Level	Fitted (with SOC)	Calculated (No SOC)	<sup>a</sup> Observed.	<sup>b</sup> F. - O.
(0,0,0)	0	0	0	0
(1,0,0)	664	660	664	0
(0,1,0)	835	842	834	1
(2,0,0)	1322	1314	1320	2
(1,1,0)	1492	1499	1494	-2
(0,2,0)	1645	1679	1638	7
(3,0,0)	1973	1959	1970	3
<b>(0,0,0)</b>	<b>2064</b>	<b>2074</b>	<b>2065</b>	<b>-1</b>
(0,0,1)	2087	2074	2087	0
(2,1,0)	2144	2149	2147	-3
(1,2,0)	2302	2332	2299	3
(0,3,0)	2509	2510	2506	3
(4,0,0)	2614	2598	2613	1
<b>(0,1,0)</b>	<b>2717</b>	<b>2695</b>	<b>2721</b>	<b>-4</b>
(1,0,1)	2750	2734	2749	1
(3,1,0)	2793	2791	2793	0

<b>(1,0,0)</b>	<b>2838</b>	<b>2793</b>	<b>2838</b>	<b>0</b>
(0,1,1)	2914	2908	2917	-3
(2,2,0)	2951	2978	2952	-1
(1,3,0)	3164	3159	3168	-4
(5,0,0)	3247	3230	3246	1
(2,0,1)	3404	3388	3404	0
(4,1,0)	3438	3427	3433	5
<b>(2,0,0)</b>	<b>3545</b>	<b>3512</b>	<b>3542</b>	<b>3</b>
(1,1,1)	3583	3565	3571	12
(3,2,0)	3597	3617	3600	-3
(0,2,1)	3730	3736	3730	0
(2,3,0)	3813	3802	3825	-12
(6,0,0)	3872	3855	3876	-4
<b>(0,3,0)</b>	<b>3942</b>	<b>3924</b>	<b>3939</b>	<b>3</b>
(3,0,1)	4050	4034	4052	-2
(5,1,0)	4071	4055	4067	4
(0,5,0)	4136	4153	4134	2
<b>(2,1,0)</b>	<b>4183</b>	<b>4133</b>	<b>4181</b>	<b>2</b>
(2,1,1)	4225	4214	4231	-6
(4,2,0)	4242	4249	4237	5
<b>(3,0,0)</b>	<b>4277</b>	<b>4230</b>	<b>4279</b>	<b>-2</b>
(1,2,1)	4391	4389	4389	2
(0,3,1)	4602	4558	4616	-14
<b>(2,2,0)</b>	<b>4779</b>	<b>4750</b>	<b>4774</b>	<b>5</b>
(1,0,2)	4827	4809	4820	7
<b>°MAD</b>				<b>3</b>

<sup>a</sup>SVL emission energy levels from reference<sup>167</sup>

## 7.5 FIT PARAMETERS

Table 14 compares the fitted vibrational frequencies to those from *ab initio* calculations done at B3LYP/aug-cc-pVTZ level of theory. The C-Br stretch and bending modes are in relatively good agreement with the calculated vibrational frequencies.

Table 15 shows the computed fit parameters that includes, electronic the spin-orbit element,  $H_{so}^{elec}$ , the singlet-triplet energy gap  $\Delta E_{ST}$ .  $H_{so}^{elec}$  was predicted to be  $350\text{cm}^{-1}$ , which is in good agreement with the  $330\text{cm}^{-1}$  obtained in reference<sup>141</sup>. The  $\Delta E_{ST}$  was calculated to be  $2080\text{cm}^{-1}$ . Only important non-zero anharmonicity constants obtained in the fitting are listed in Table 15.

**Table 14:** CDBr vibrational frequencies, in  $\text{cm}^{-1}$ .

Species	Mode	<sup>a</sup> Fit Frequency	<sup>b</sup> Calculated Frequency
CDBr ( $S_0$ )	C-Br Stretch	664(0.4)	640.9
	Bend	846(0.6)	853.7
	C-D stretch	2074(0.4)	2154
CDBr ( $T_1$ )	C-Br Stretch	720.2(0.6)	732.5
	Bend	623.1(1.5)	641.0
	C-D stretch	2339 <sup>c</sup>	2336

<sup>a</sup>One standard deviation in parenthesis (right justified)

<sup>b</sup>Unscaled vibrational frequencies calculated at B3LYP/aug-cc-pVTZ level

<sup>c</sup>Anharmonic vibrational frequency

**Table 15:** Shows the fit parameters obtained during the fitting of the energy levels to the experimental values for CDBr.

Fit Parameters/cm <sup>-1</sup>	
$H_{so}^{elec}$	350(3)
$\Delta E_{ST}$	2080(1)
$\tilde{X}$	
$x_{11}$	-3.55(0.1)
$x_{22}$	-3.02(0.2)
$x_{12}$	-3.57(0.2)
$x_{13}$	0.0
$x_{23}$	-8.9
$\tilde{a}$	
$x_{11}$	-0.49
$x_{22}$	-2.8(0.7)

## 7.6 ENERGY LEVEL DIAGRAM FOR CDBr

In order to visualize how close the calculated energy levels are to the experimental energy levels, Figure 53 displays these energy levels listed in Table 13. Below the triplet origin level, the singlet levels are easily assigned due to the absence of any perturbing level. However, the  $\tilde{X}(0,2,0)$  could have been pushed down a little bit further by the triplet  $\tilde{a}(0,0,0)$  level than could be detected by the theoretical computation.  $\tilde{X}(0,2,0)$  was observed at  $1638\text{cm}^{-1}$  and the calculated perturbed position is  $1345\text{cm}^{-1}$ , a further deviation of  $7\text{cm}^{-1}$ .

Chang and co-workers<sup>141</sup> predicted it to be at  $1636\text{cm}^{-1}$ .  $\tilde{X}(3,0,0)$  and  $\tilde{X}(0,0,1)$  are even much closer to the  $\tilde{a}(0,0,0)$  level but Tao and co-workers<sup>165</sup> proved that these levels are not perturbed due to a poor Frank Condon factor with the  $\tilde{a}(0,0,0)$  or any other perturbing state.

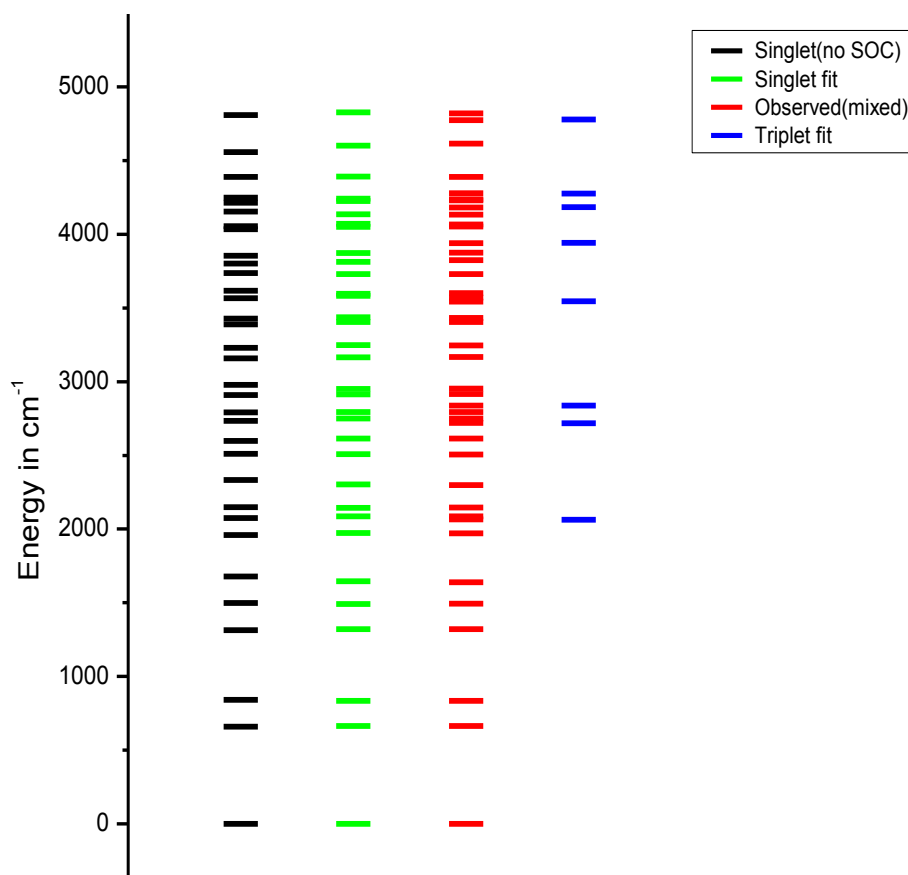


**Figure 53:** Term energy diagram for CDBr which compares the predicted singlet and triplet level positions. The first black column displays calculated singlet energy levels without spin orbit coupling. The second and last column shows some fitted singlet and triplet energy levels that incorporated spin orbit coupling respectively. The third column displays mixed observed levels from reference<sup>165</sup>



CHAPTER 8. CH<sup>35</sup>Cl AND CD<sup>35</sup>Cl8.1 CH<sup>35</sup>Cl VIBRATIONAL ENERGY LEVEL ASSIGNMENTS

The observed data for CH<sup>35</sup>Cl is so large as compared to CHBr or CHI, this resulted in the setting up of a large Hamiltonian matrix in order to reproduce the experimental term energies. As can be seen in Table 16, the new calculated energies are in very good agreement with the observed values even at higher energies where the perturbations become more unpredictable. The least squares fitting predicted numerous singlet and triplet vibrational levels up to 8200cm<sup>-1</sup> but displayed here are only those corresponding to the observed levels. The C-Cl fundamental stretching frequency was predicted with zero deviation from the experimental at 811cm<sup>-1</sup>. The fundamental bending vibrational frequency was observed at 1198cm<sup>-1</sup> with SVL emission and at 1196cm<sup>-1</sup> with SEP measurements. Calculations predicted it to be 1198cm<sup>-1</sup> which is impressive considering that these positions are not their zeroth order positions, they are shifted via spin orbit coupling with the background triplet electronic state. The triplet origin is also predicted at 2168cm<sup>-1</sup>, with zero deviation from the observed value. The calculations had a mean averaged deviation of 2cm<sup>-1</sup>. The experimental uncertainty is also 2cm<sup>-1</sup>,<sup>168</sup> Yu and co-workers.<sup>194</sup> Calculations produced a standard deviation of 9cm<sup>-1</sup> from a small data set that did not incorporate spin orbit coupling. Tarczay and co-workers<sup>195</sup> calculations that did not include spin orbit coupling between the states obtained a standard deviation of 6cm<sup>-1</sup> using VAR4<sup>+</sup> variational method for some 33 vibrational levels. The calculations make a very good improvement on the number of higher energy levels assigned as well as make

an improved fitting to the experimental data. The Dunham Expansion seemed to do very well also on the prediction of the term energies for  $\text{CH}^{35}\text{Cl}$ .

**Table 16:** Vibrational levels assignments for  $\text{CH}^{35}\text{Cl}$ . Energies are in  $\text{cm}^{-1}$ .

Level	Fitted (with SOC)	Calculate d (No SOC)	<sup>a</sup> Observ ed	<sup>c</sup> F. - O.
(0,0,0)	0	0	0	0
(1,0,0)	811	811	811	-1
(0,1,0)	1198	1198	1196	2
(2,0,0)	1611	1611	1613	-1
(1,1,0)	2001	2001	1999	2
<b>(0,0,0)</b>	<b>2168</b>	<b>2168</b>	<b>2168</b>	<b>0</b>
(0,2,0)	2380	2379	2387	-7
(3,0,0)	2402	2402	2401	1
(2,1,0)	2794	2794	2787	7
(0,0,1)	2797	2798	2795	2
<b>(1,0,0)</b>	<b>3050</b>	<b>3050</b>	<b>3049</b>	<b>0</b>
<b>(0,1,0)</b>	<b>3129</b>	<b>3127</b>	<b>3127</b>	<b>2</b>
(1,2,0)	3175	3174	3179	-4
(4,0,0)	3184	3183	3185	-2
(0,3,0)	3543	3543	3542	1
(3,1,0)	3577	3577	3577	0
(1,0,1)	3608	3608	3605	4
<b>(2,0,0)</b>	<b>3927</b>	<b>3929</b>	<b>3925</b>	<b>2</b>
(2,2,0)	3963	3959	3969	-5
(0,1,1)	3978	3979	3978	0
<b>(1,1,0)</b>	<b>4011</b>	<b>4009</b>	<b>4012</b>	<b>-1</b>
(1,3,0)	4331	4330	4329	1
(4,1,0)	4350	4350	4350	0

(2,0,1)	4409	4409	4408	1
(0,4,0)	4691	4689	4689	2
(3,2,0)	4735	4734	4729	5
(1,1,1)	4781	4779	4782	-1
(2,3,0)	5108	5107	5110	-2
(5,1,0)	5113	5113	5110	3
(0,2,1)	5139	5138	5132	7
(3,0,1)	5200	5200	5200	0
<b>(0,0,1)</b>	<b>5245</b>	<b>5244</b>	<b>5246</b>	<b>-1</b>
(0,0,2)	5445	5444	5447	-2
(1,4,0)	5470	5467	5467	2
(7,0,0)	5467	5466	5467	0
(4,2,0)	5500	5499	5499	1
(2,1,1)	5574	5572	5577	-3
(0,5,0)	5820	5819	5822	-2
(3,3,0)	5875	5874	5873	2
(1,2,1)	5934	5933	5934	0
(2,4,0)	6239	6238	6240	-1
(5,2,0)	6255	6254	6258	-3
(0,3,1)	6287	6283	6288	-1
(3,1,1)	6356	6355	6364	-8
(1,5,0)	6592	6590	6587	5
(4,3,0)	6632	6631	6630	2
<b>(3,2,0)</b>	<b>6726</b>	<b>6724</b>	<b>6726</b>	<b>0</b>
(0,6,0)	6933	6932	6934	-1
(6,2,0)	7001	7000	7002	-1
(2,0,2)	7056	7055	7055	1
(2,5,0)	7353	7352	7354	-1
(1,6,0)	7696	7695	7698	-2
(3,0,2)	7847	7846	7843	4
<b><sup>c</sup>MAD</b>				<b>2</b>

<sup>a</sup> Stimulated emission pumping and SVL emission energy levels from reference <sup>167</sup> and reference <sup>170</sup>

## 8.2 FIT PARAMETERS

The anharmonic vibrational frequency for C-H is listed in Table 17 for the  $T_1$  state because only  $\nu_3=0,1$  vibrational levels were needed and trying to fit only these few and smaller vibrational quantum number levels gives outrageous results. Other vibrational modes  $(\nu_1,0,0)$ ,  $(0, \nu_2,0)$  and  $(\nu_1,\nu_2,0)$  were well represented in the fitting data for higher quantum numbers ( $\nu_1=0-7$ ,  $\nu_2=0,6$ ). Table 18 shows some computed least squares fit parameters, the singlet-triplet energy gap  $\Delta E_{ST}$ .  $H_{SO}^{elec}$  was predicted to be  $115.0\text{cm}^{-1}$ . The  $\Delta E_{ST}$  was predicted to be  $2167.0\text{cm}^{-1}$ . Any missing anharmonicity constant from Table 18 that is found in the Dunham expansion could not be well determined in the fit due to low vibrational quantum numbers in the data and set was to zero. Since only a first few triplet levels were fit, only  $x_{11}$  had a significant effect on improving the fitting.

**Table 17:**  $\text{CH}^{35}\text{Cl}$  vibrational frequencies  $/\text{cm}^{-1}$ .

Species	Mode	<sup>a</sup> Fit Frequency	<sup>b</sup> Calculated Frequency
$\text{CH}^{35}\text{Cl}$ ( $S_0$ )	C-Cl Stretch	815.6(0.1)	792.6
	Bend	1206.5(0.2)	1228.2
	C-H stretch	2873.2(1.3)	2917.4
$\text{CH}^{35}\text{Cl}$ ( $T_1$ )	C-Cl Stretch	883.5(0.3)	874.8
	Bend	958.8(0.5)	952.8
	C-H stretch	3076.4(3.4) <sup>c</sup>	3173

<sup>a</sup>The parenthesis encloses the standard deviation in the average parameter value.

<sup>b</sup>Unscaled vibrational frequencies calculated at B3LYP/aug-cc-pVTZ level

<sup>c</sup>Anharmonic value

**Table 18:** Fit parameters for  $\text{CH}^{35}\text{Cl}$ . The parenthesis encloses the standard deviation in the average parameter value.

<b>Fit Parameters/cm<sup>-1</sup></b>	
$H_{so}^{elec}$	115.0(3)
$\Delta E_{ST}$	2167.0(0.4)
<b>Anharmonicity constants in <math>\tilde{X}</math></b>	
$x_{11}$	-5.0(0.1)
$x_{22}$	-8.5(0.1)
$x_{33}$	-75.6(1.3)
$x_{12}$	-7.9(0.1)
$x_{23}$	-19.1(0.2)
<b>Anharmonicity constants in <math>\tilde{a}</math></b>	
$x_{11}$	-1.3(0.2)
$X_{33}$	-2.1(1.1)
$X_{23}$	-1.0(3.3)

### 8.3 ENERGY LEVEL DIAGRAM

The stick energy diagram shown in Figure 54 represents the data in Table 16 for the  $\text{CH}^{35}\text{Cl}$ . Many higher energy levels were calculated but shown here are only levels that fitted very well to the observed energies. It is evident from the diagram that levels starts to get perturbed and squeezed together at higher energies just after the triplet origin. However the calculations predicted these perturbed positions with a mean averaged deviation of  $2\text{cm}^{-1}$  which is as good as the experimental error of  $2\text{cm}^{-1}$ .<sup>168, 170</sup>

It is important to mention that the Dunham Expansion regardless of excluding spin orbit coupling produced good term energy approximations which were comparable to the least squares fitting of the calculated singlet energies and triplet energies incorporating spin orbit coupling. This is expected as the spin orbit matrix elements becomes smaller and smaller from CHI to CHF.

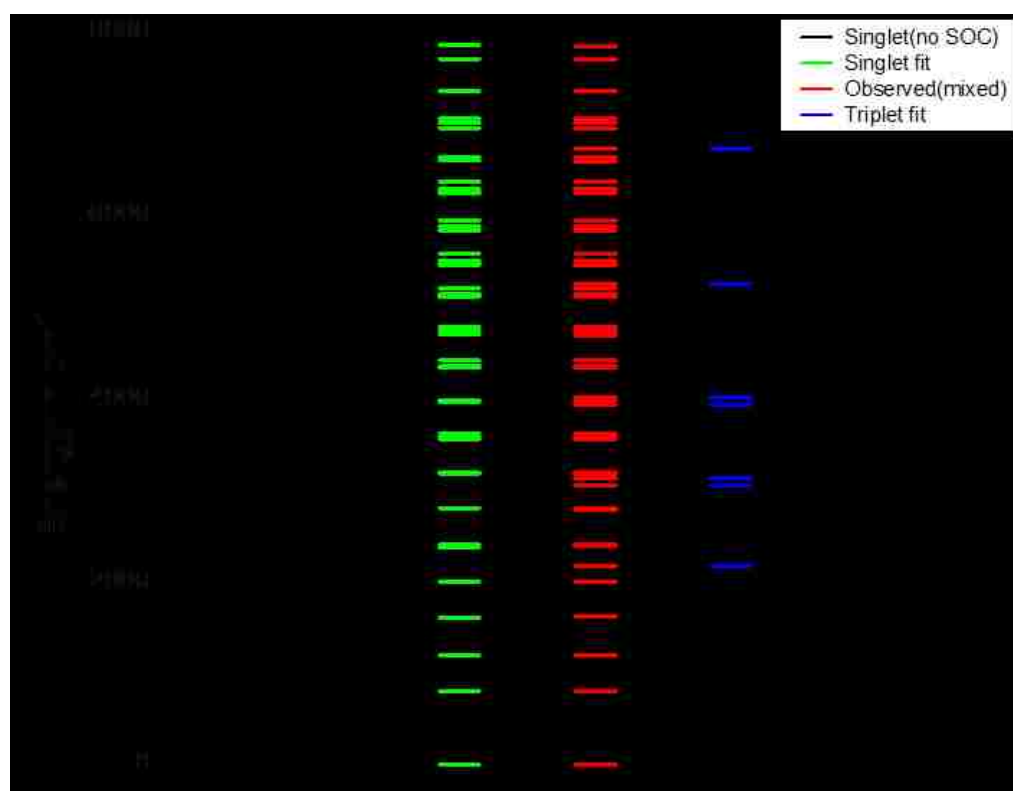


**Figure 54:** Stick energy diagram for CH<sup>35</sup>Cl. The fitted S<sub>0</sub> and T<sub>1</sub> term energies (with spin orbit coupling) are shown in the second and last column. The calculated singlet energies (without spin orbit coupling) are shown in the first black column. The observed term energies shown in the third column were taken from references<sup>168, 170</sup>.

#### 8.4 CD<sup>35</sup>Cl SINGLE VIBRONIC LEVEL EMISSION

Tao and co-workers<sup>169</sup> obtained a wide range of emission spectra from pumping various excited singlet levels, from these they probed the ground singlet state and the low lying triplet state vibrational levels. Lin and co-workers<sup>160</sup> obtained similar spectra earlier for both halogen isotopes (CD<sup>35</sup>Cl and CD<sup>37</sup>Cl) but only observed fewer levels as compared to Tao and co-workers studies. Calculations presented here predicted even more levels than Tao and co-workers and are in very good agreement as can be seen in Table 19 which lists the calculated and the observed levels side by side. The current assignments to the levels also agree very well with previous assignments made by Tao and co-workers. Assignments were made to more than 100 vibrational levels in CD<sup>35</sup>Cl and Table 19 displays about half of them which correspond to experimentally observed levels. The least squares fitting of the levels had a mean averaged deviation of 1.7cm<sup>-1</sup> which is in good agreement of the experimental deviation of 2cm<sup>-1</sup>.<sup>169</sup> The fundamental C-Cl stretching frequency was observed at 799cm<sup>-1</sup> and computed to be at 801cm<sup>-1</sup>. Also the bending fundamental only deviated from the experimental by just 1cm<sup>-1</sup>. The lower singlet energy levels are not likely to have been perturbed by the triplet origin level because these levels are well separated from the triplet origin to have an effect. However, the  $\tilde{X}(0,2,0)$  bending level and higher energy levels associated with the bending mode are most likely to be heavily perturbed from their zeroth order positions by the triplet levels. This is because the wave-functions of the excited bending levels of the  $\tilde{X}$  state extends deeper into crossing region of the two states.

**Table 19:** Vibrational level assignments for CD<sup>35</sup>Cl. Energies are in cm<sup>-1</sup>.

Level	Fitted (with SOC)	Calculated (No SOC)	<sup>a</sup> Observed	F. - O.
(0,0,0)	0	0	0	0
(1,0,0)	801	801	799	2
(0,1,0)	891	891	890	1
(2,0,0)	1593	1593	1591	2
(1,1,0)	1688	1688	1688	0
(0,2,0)	1770	1772	1768	2
(0,0,1)	2081	2081	2078	3
<b>(0,0,0)</b>	<b>2184</b>	<b>2184</b>	<b>2183</b>	<b>1</b>
(3,0,0)	2376	2375	2374	1
(2,1,0)	2475	2475	2476	-1
(1,2,0)	2563	2564	2565	-2
(0,3,0)	2643	2642	2643	0
(1,0,1)	2881	2881	2880	1
(0,1,1)	2970	2970	2974	-4
<b>(1,0,0)</b>	<b>3068</b>	<b>3148</b>	<b>3070</b>	<b>-2</b>
(4,0,0)	3149	3149	3148	1
(3,1,0)	3254	3254	3254	0
(2,2,0)	3346	3346	3348	-2
(1,3,0)	3432	3430	3433	-1
(0,4,0)	3498	3502	3494	5
<b>(0,2,0)</b>	<b>3587</b>	<b>3582</b>	<b>3589</b>	<b>-1</b>
(2,0,1)	3671	3670	3670	1
(1,1,1)	3764	3765	3767	-3
<b>(1,1,0)</b>	<b>3772</b>	<b>3767</b>	<b>3769</b>	<b>2</b>
(0,2,1)	3849	3841	3848	0
(5,0,0)	3913	3912	3912	1
(4,1,0)	4022	4022	4024	-2
(0,0,2)	4088	4087	4088	0
(3,2,0)	4120	4121	4120	0



(2,3,0)	4211	4209	4212	0
<b>(0,3,0)</b>	<b>4275</b>	<b>4280</b>	<b>4281</b>	<b>-5</b>
(1,4,0)	4292	4285	4295	-2
(0,5,0)	4349	4351	4349	1
(3,0,1)	4452	4451	4452	0
(2,1,1)	4551	4551	4555	-3
(1,2,1)	4638	4639	4640	-2
(0,3,1)	4719	4717	4717	3
(5,1,0)	4782	4782	4783	-1
(1,0,2)	4885	4884	4886	0
(4,2,0)	4885	4885	4886	-1
(3,3,0)	4984	4978	4988	-4
(2,4,0)	5059	5060	5059	1
(1,5,0)	5130	5130	5131	-1
(0,6,0)	5193	5189	5190	3
(3,1,1)	5328	5327	5329	-1
<b>(2,2,0)</b>	<b>5354</b>	<b>5350</b>	<b>5353</b>	<b>1</b>
(2,2,1)	5420	5421	5419	1
(1,3,1)	5508	5503	5506	2
(2,0,2)	5674	5672	5672	2
(3,4,0)	5824	5824	5823	1
(0,2,2)	5850	5850	5851	-1
(2,5,0)	5900	5900	5895	5
(1,6,0)	5965	5964	5963	2
(0,7,0)	6019	6017	6026	-7
(3,2,1)	6193	6192	6193	0
<b>MAD</b>				<b>1.7</b>

<sup>a</sup>SVL emission energy levels from reference <sup>153, 169</sup>

## 8.5 FIT PARAMETERS

The fitting parameters for  $\text{CD}^{35}\text{Cl}$  are shown in Table 20. The  $\Delta E_{\text{ST}}$  gap was predicted to be  $2183\text{cm}^{-1}$ , in good agreement with  $2187\text{cm}^{-1}$  obtained in reference<sup>160</sup> and also other publications.<sup>146, 194</sup> Spin orbit element of  $78.0\text{cm}^{-1}$  was obtained, which is consistent with the trend observed for mono halocarbenes. Here, only a few anharmonicity constants for the  $\tilde{a}$  state are considered due to the few observed triplet levels that can be fit. For singlet state, a lot of higher energy vibrational levels were observed and so all the anharmonicity constants are included.

**Table 20:** Fitted vibrational frequencies against the *ab initio* calculations using B3LYP/aug-cc-pVTZ level of theory for  $\text{CD}^{35}\text{Cl}$ . Vibrational frequencies are in  $\text{cm}^{-1}$ .

State(s)	Mode	$\omega$ Frequency	$\omega^a$ Calculated
$\tilde{a}(^3\Pi)$	$\nu_1$ (C-Cl stretch)	810.7(0.1)	794.7
	Band	1096.3(0.2)	908.9
	$\nu_2$ (C-Cl stretch)	2119.2(0.4)	2154.0
	$\nu_3$ (C-Cl stretch)	3084.3(1.3)	3060.4
$\tilde{a}(^1\Pi)$	Band	1598.0(0.7)	1610.2
	$\nu_1$ (C-Cl stretch)	2231.7 <sup>b</sup>	2121.0

<sup>a</sup>Standard deviation in parenthesis (right justified)

<sup>b</sup>Unscaled vibrational frequencies calculated at B3LYP/aug-cc-pVTZ level

<sup>c</sup>Anharmonic value

**Table 21:** Shows the fit parameters obtained during the fitting of the calculated energy levels to the experimental values for  $\text{CD}^{35}\text{Cl}$ . The parenthesis encloses the standard deviation in the average parameter value.

The image shows a table with fit parameters for  $\text{CD}^{35}\text{Cl}$ . The parameters are listed in two columns, with their values and standard deviations in parentheses. The parameters include  $\alpha_{11}$ ,  $\alpha_{12}$ ,  $\alpha_{21}$ ,  $\alpha_{22}$ ,  $\beta_{11}$ ,  $\beta_{12}$ ,  $\beta_{21}$ , and  $\beta_{22}$ . The values range from approximately -4.7 to 22.3.

Parameter	Value (Standard Deviation)
$\alpha_{11}$	-4.7(0.3)
$\alpha_{12}$	1(0.2)
$\alpha_{21}$	17.4(0.3)
$\alpha_{22}$	-4.4(0.1)
$\beta_{11}$	27(3.2)
$\beta_{12}$	2.3(1.7)
$\beta_{21}$	-0.1(0.3)
$\beta_{22}$	1.0(0.2)
$\beta_{31}$	22.3(1.2)

## 8.6 RESULTS ANALYSIS

### 8.6.1 SINGLET-TRIPLET ENERGY GAPS

Table 22 summarises findings on the singlet-triplet energy gaps in mono halocarbenes. As expected, the energy gap was predicted to increase with electronegativity of the halogen substituent.

This was explained in a number of ways, the popular one being; the electron withdrawing halogen substituents inductively stabilize the  $\sigma$  nonbonding orbital by enhancing its s character.<sup>159, 205</sup> The stabilization of the  $\sigma$  leads to a change in the hybridization and an increased  $\sigma^2 p$  (singlet state)-  $\sigma^1 p^1$ (triplet state) energy gap. Irikura and Bauschlicher<sup>159</sup> also suggested that the electron withdrawing halogens withdraw charge from the carbenic carbon leaving a positive charge. The increased positive charge stabilizes the 2s orbital relative to the 2p orbital, this favors a singlet state. The average singlet-triplet gaps of the carbenes are within the range obtained by other groups.<sup>173, 191</sup>

**Table 22:** Summarization of the singlet-triplet energy gap results in mono halocarbenes/cm<sup>-1</sup>.

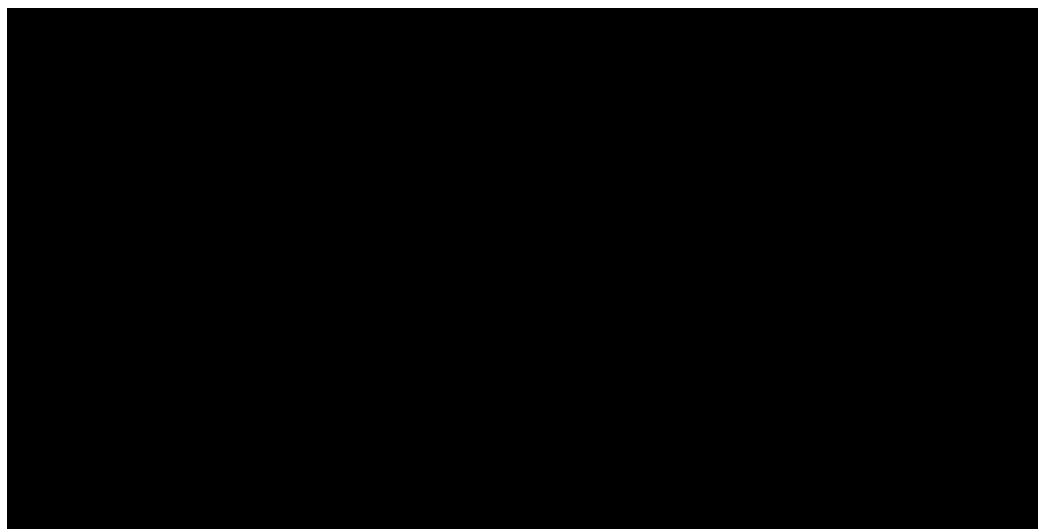
Halogenation	CTD Singlet-Triplet Energy Gap, $\Delta E_{ST}$	CTD Singlet-Triplet Energy Gap, $\Delta E_{ST}$	Average $\Delta E_{ST}$
X	1732(8)	1735(8)	1734
Fl	2159(2)	2189(1)	2174
Cl	2177(1)	2175(1)	2176
Br			1971 <sup>b</sup>

## 8.6.2 COMPARISON OF DERIVED SPIN-ORBIT COUPLING CONSTANTS

The atomic spin orbit constants for halogens increases with the increase in atomic size. Figure 55 shows the linear correlation between the atomic and molecular spin orbit coupling constants. The slope of the fitted linear curve defines the degree of spin orbit coupling constant quenching in CHX and CDX carbenes from the bare halogen atom spin orbit coupling constant. In CHX/CDX, the coupling drops to about 14% that of the corresponding bare halogen atom. If this linear relationship is true, then one would predict the spin orbit coupling in CHF to be around  $38\text{cm}^{-1}$ , (see Table 23). This is however not the case, as there was no evidence of any significant spin orbit coupling between the  $\tilde{X}^1A'$  and the  $\tilde{a}^3A''$  found in CHF<sup>135, 143, 144, 148</sup> even though evidence of perturbation of the singlet levels was observed, it was suggested they are not caused by the high lying triplet state,  $\tilde{a}^3A''$ . The  $H_{so}^{elec}$  was fitted separately for the deuterated species, giving a slight difference with that of CHX as shown in Table 23.  $H_{so}^{elec}$  is a purely electronic parameter and theoretically one should obtain the same spin orbit coupling matrix element for each pair of carbene species, for example in CHI and CDI, the only difference is the heavy hydrogen but similar electronic structure. However, the difference in  $H_{so}^{elec}$  is small and reasonable for CHI/CDI ( $8\text{cm}^{-1}$ ) and  $4\text{cm}^{-1}$  for CHBr/CDBr carbene species. There is relatively large difference between the  $H_{so}^{elec}$  in CHCl and CDCl ( $37\text{cm}^{-1}$ ).

The fitting of the parameters is slightly affected by the number of assignments made and included in the matrix scheme. Also different vibrational levels were assigned to the two systems. Other input fitting parameters to take into consideration are the singlet-triplet energy gap,  $\Delta E_{ST}$ , the anharmonicity constants and the fitted vibrational frequencies. CHX and CDX were also fit to the same  $H_{so}^{elec}$  and the results were within the range produced by the individual species.

**Table 23:** Comparison of atomic versus carbene spin-orbit coupling constants /  $\text{cm}^{-1}$ .



<sup>a</sup>Handbook of photochemistry, third edition.<sup>206</sup>

<sup>b</sup>QCISD(T)/6-311+G(3df,2p).<sup>173</sup>

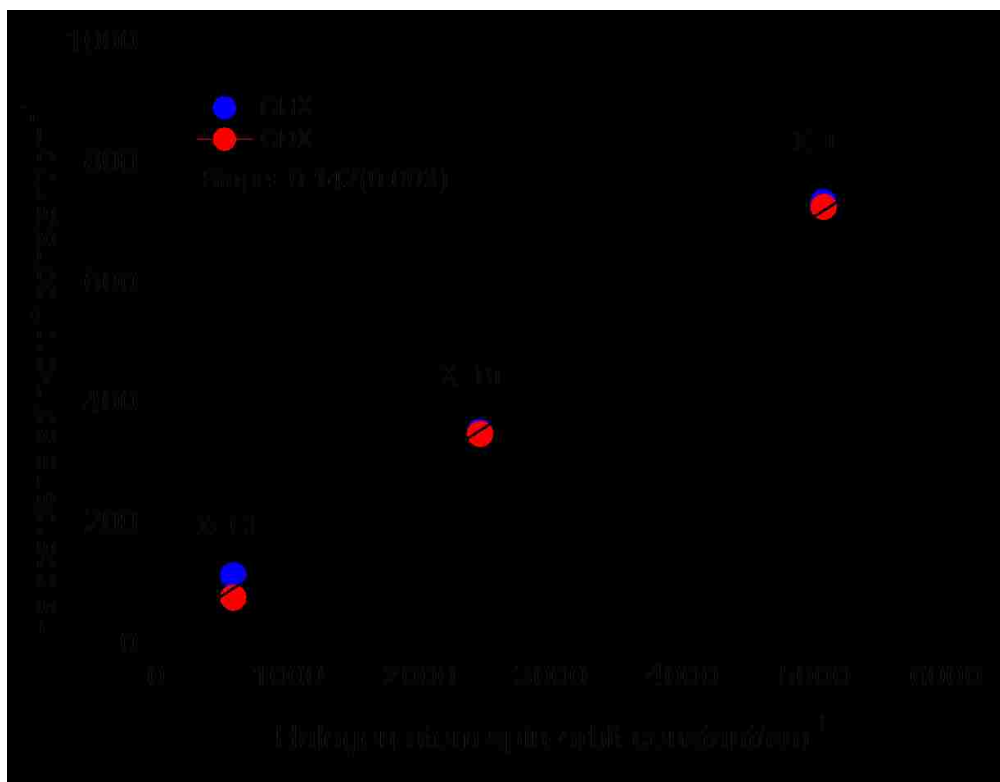


**Figure 55:** Comparison of derived spin-orbit coupling constants with those of the bare halogen atoms using data in Table 23. The black symbols represent CHX and the red points CDX. The blue diamond is the fluorine atomic spin orbit coupling constant from reference <sup>206</sup>.

## SUMMARY

In conclusion, in this work electronic spin-orbit coupling have been studied and reported for 3 mono halocarbenes CHI, CHBr, CHCl and their deuterated isotopomers. Full incorporation of the of Duschinsky mixing was done in calculation of the vibrational overlaps of the singlet and triplet state levels. *Ab initio* calculations, single vibronic emission spectra simulations, matrix diagonalisation routines and least squares fitting routine were used to calculate electronic spin-orbit coupling constants,  $H_{so}^{elec}$ . Singlet and triplet vibrational levels were also obtained and assigned firmly.

This work complemented a series of experimental and theoretical research studies that has been going on. A number of research groups have highlighted the need for a deperturbation analysis on the observed and highly perturbed term energies. The spin orbit coupling between the  $\tilde{X}^1A'$  and  $\tilde{a}^3A''$  state in mono halocarbenes was predicted to increase as the energy gap between the two electronic states gets smaller. The  $H_{so}^{elec}$  was found to be inversely proportional to the  $\Delta E_{ST}$  gap. The derived  $H_{so}^{elec}$  show a good correlation with those of bare halogen atoms and were fit to within an experimental error of  $2\text{cm}^{-1}$ . The atomic spin-orbit coupling is quenched to about 14% in halocarbenes. Theoretical vibrational term energies for both the ground singlet state and triplet state were determined and were in good agreement with other references and previous experimental efforts. Perturbed singlet and triplet vibrational levels which were difficult to assign before were predicted with a small deviation from the observed values and were assigned firmly. Assigning more vibrational levels with a smaller standard deviation was a huge improvement to the series of ongoing investigations on halocarbenes. The observed perturbation of singlet states saved as a strong evidence of the existence of a background triplet state,  $\tilde{a}^3A''$ . The perturbation of singlet vibrational levels by the triplet energy levels was found to be selective and mostly strong for the bending levels.  $\Delta E_{ST}$  gaps were calculated for the carbene species, and it was found to be in good agreement with literature.



## REFERENCES

1. Awdiew, J., et al., *Investigation of Reaction Barriers in Mixed Organic Aggregates by 2-Color Resonant 2-Photon Ionization*. Berichte Der Bunsen-Gesellschaft-Physical Chemistry Chemical Physics, 1990. **94**(11): p. 1353-1357.
2. Brutschy, B., *Reactions in Molecular Clusters Following Photoionization*. Journal of Physical Chemistry, 1990. **94**(24): p. 8637-8647.
3. Brutschy, B., *The structure of microsolvated benzene derivatives and the role of aromatic substituents*. Chemical Reviews, 2000. **100**(11): p. 3891-3920.
4. Brutschy, B., et al., *Nucleophilic-Substitution Reactions in Molecular Clusters Following Photoionization*. Journal of Physical Chemistry, 1991. **95**(13): p. 5041-5050.
5. Ringer, A.L., et al., *The effect of multiple substituents on sandwich and T-Shaped pi-pi interactions*. Chemistry-a European Journal, 2006. **12**(14): p. 3821-3828.
6. Chipot, C., et al., *Benzene dimer: A good model for pi-pi interactions in proteins? A comparison between the benzene and the toluene dimers in the gas phase and in an aqueous solution*. Journal of the American Chemical Society, 1996. **118**(45): p. 11217-11224.
7. Hohenstein, E.G., J.N. Duan, and C.D. Sherrill, *Origin of the Surprising Enhancement of Electrostatic Energies by Electron-Donating Substituents in Substituted Sandwich Benzene Dimers*. Journal of the American Chemical Society, 2011. **133**(34): p. 13244-13247.
8. Jaeger, H.M., et al., *Structures of protonated benzene dimer and intermolecular interaction decomposition via symmetry-adapted perturbation theory*. Computational and Theoretical Chemistry, 2011. **973**(1-3): p. 47-52.
9. Marshall, M.S., L.A. Burns, and C.D. Sherrill, *Basis set convergence of the coupled-cluster correction, delta(CCSD(T))(MP2): Best practices for benchmarking non-covalent interactions and the attendant revision of the S22, NBC10, HBC6, and HSG databases*. Journal of Chemical Physics, 2011. **135**(19).
10. Boatwright, A., et al., *A systematic shift in the electronic spectra of substituted benzene molecules trapped in helium nanodroplets*. Journal of Chemical Physics, 2005. **123**(2).

11. Dimopoulourademann, O., et al., *Isotopically Selective 2-Photon Ionization of Toluene and Fluorobenzene in a Supersonic Beam*. Chemical Physics Letters, 1983. **101**(4-5): p. 485-489.
12. Hunter, C.A., et al., *Aromatic interactions*. Journal of the Chemical Society-Perkin Transactions 2, 2001(5): p. 651-669.
13. Imhof, P. and K. Kleinermanns, *Dispersed fluorescence spectra of chlorobenzene*. Chemical Physics, 2001. **270**(1): p. 227-236.
14. Musgrave, A. and T.G. Wright, *Electronic spectroscopy of small toluene clusters*. Journal of Chemical Physics, 2005. **122**(7).
15. Newton, K.R. and R.B. Bernstein, *Multiphoton Ionization and Fragmentation Pathways of Benzene, Fluorobenzene, Iodobenzene, and Tert-Butylbenzene*. Journal of Physical Chemistry, 1983. **87**(12): p. 2246-2255.
16. Sears, J.S. and C.D. Sherrill, *n-n Interactions in the condensed phase: The benzene dimer*. Abstracts of Papers of the American Chemical Society, 2006. **231**.
17. Sinnokrot, M.O. and C.D. Sherrill, *High-accuracy quantum mechanical studies of pi-pi interactions in benzene dimers*. Journal of Physical Chemistry A, 2006. **110**(37): p. 10656-10668.
18. Kemsley, J., *Halogen Bonding Defined*. Chemical & Engineering News, 2012. **90**(35): p. 36-36.
19. Metrangolo, P., et al., *Halogen bonding in supramolecular chemistry*. Angewandte Chemie-International Edition, 2008. **47**(33): p. 6114-6127.
20. Politzer, P., et al., *An overview of halogen bonding*. Journal of Molecular Modeling, 2007. **13**(2): p. 305-311.
21. Clark, T., et al., *Halogen bonding: the sigma-hole*. Journal of Molecular Modeling, 2007. **13**(2): p. 291-296.
22. Schuster, P. and W. Mikenda, *Hydrogen bond research*. Monatshefte Fur Chemie, 1999. **130**(8): p. 945-946.
23. Zhu, S.Z., et al., *Hydrogen bonding and halogen bonding co-existing in the reaction of heptafluorobenzyl iodide with N,N,N',N'-tetramethylethylene diamine*. Tetrahedron Letters, 2004. **45**(4): p. 777-780.

24. Pierangelo Metrangolo, ‡, Jane S. Murray, \*, §, Tullio Pilati, †, Peter Politzer, \*, §, Giuseppe Resnati, †, ‡, and G. Terraneo †, Fluorine-Centered Halogen Bonding: A Factor in Recognition Phenomena and Reactivity. *Crystal Growth & Design*, 2013.
25. Riley, K.E. and K.M. Merz, Jr., Insights into the strength and origin of halogen bonding: the halobenzene-formaldehyde dimer. *J Phys Chem A*, 2007. **111**(9): p. 1688-94.
26. Metrangolo, P., et al., *Halogen bonding in crystal engineering*. *Halogen Bonding: Fundamentals and Applications*, 2008. **126**: p. 105-136.
27. Ritter, S.K., *Halogen Bonding Begins to Fly*. *Chemical & Engineering News*, 2009. **87**(38): p. 39-42.
28. Rogers, R.D., *Halogen Bonding: Weak Interactions Result in Strong Opinions*. *Crystal Growth & Design*, 2011. **11**(11): p. 4721-4722.
29. Zhu, H.B., et al., *A novel coordination polymer constructed from 1D neutral chains via inter-chain pi-pi stacking and hydrogen bonding*. *Inorganic Chemistry Communications*, 2004. **7**(10): p. 1095-1099.
30. Zhu, S.Z., et al., *Halogen bonding and hydrogen bonding coexist in driving self-assembly process*. *Crystal Growth & Design*, 2004. **4**(1): p. 53-56.
31. Politzer, P., J.S. Murray, and M.C. Concha, *Halogen bonding and the design of new materials: organic bromides, chlorides and perhaps even fluorides as donors*. *Journal of Molecular Modeling*, 2007. **13**(6-7): p. 643-650.
32. Meyer, E.A., R.K. Castellano, and F. Diederich, *Interactions with aromatic rings in chemical and biological recognition*. *Angewandte Chemie-International Edition*, 2003. **42**(11): p. 1210-1250.
33. McGaughey, G.B., M. Gagne, and A.K. Rappe, *pi-stacking interactions - Alive and well in proteins*. *Journal of Biological Chemistry*, 1998. **273**(25): p. 15458-15463.
34. Saenger, W., *Structural Studies on Nucleic-Acids - from Nucleotides to the Double Helix*. *Nucleosides & Nucleotides*, 1990. **9**(3): p. 297-301.
35. Heinemann, U. and W. Saenger, *Ribonuclease-T1 - Specific Protein-Nucleic Acid Interaction and Mechanism of Rna Hydrolysis*. *Biological Chemistry Hoppe-Seyler*, 1985. **366**(9): p. 798-798.

36. Heinemann, U. and W. Saenger, *Specific Protein-Nucleic Acid Recognition in Ribonuclease-T1-2'-Guanylic Acid Complex - an X-Ray Study*. Nature, 1982. **299**(5878): p. 27-31.
37. Tosi, C. and W. Saenger, *The Pseudo-Rotational Interconversion of the Furanose Ring Conformers in Nucleic-Acids*. Chemical Physics Letters, 1982. **90**(4): p. 277-281.
38. Smithrud, D.B. and F. Diederich, *Strength of Molecular Complexation of Apolar Solutes in Water and in Organic-Solvents Is Predictable by Linear Free-Energy Relationships - a General-Model for Solvation Effects on Apolar Binding*. Journal of the American Chemical Society, 1990. **112**(1): p. 339-343.
39. Burley, S.K. and G.A. Petsko, *Aromatic-Aromatic Interaction - a Mechanism of Protein-Structure Stabilization*. Science, 1985. **229**(4708): p. 23-28.
40. Ishida, T., et al., *Structural Studies of the Interaction between Indole-Derivatives and Biologically Important Aromatic-Compounds .20. Specific Ring Stacking Interaction on the Tryptophan 7-Methylguanine System - Comparative Crystallographic Studies of Indole-Derivatives 7-Methylguanine Base, Nucleoside, and Nucleotide Complexes*. Journal of the American Chemical Society, 1988. **110**(7): p. 2286-2294.
41. Brana, M.F., et al., *Intercalators as anticancer drugs*. Current Pharmaceutical Design, 2001. **7**(17): p. 1745-1780.
42. Sinnokrot, M.O., E.F. Valeev, and C.D. Sherrill, *Estimates of the ab initio limit for pi-pi interactions: The benzene dimer*. Journal of the American Chemical Society, 2002. **124**(36): p. 10887-10893.
43. Sherrill, C.D., M.O. Sinnokrot, and E.F. Valeev, *Complete basis set estimates for benzene dimer and other weakly bound systems*. Abstracts of Papers of the American Chemical Society, 2002. **223**: p. U476-U477.
44. Ishikawa, S., et al., *Hole-burning and stimulated Raman-UV double resonance spectroscopies of jet-cooled toluene dimer*. Journal of Physical Chemistry, 1996. **100**(25): p. 10531-10535.
45. Hunter, C.A., J. Singh, and J.M. Thornton, *Pi-Pi-Interactions - the Geometry and Energetics of Phenylalanine Phenylalanine Interactions in Proteins*. Journal of Molecular Biology, 1991. **218**(4): p. 837-846.
46. Schauer, M. and E.R. Bernstein, *Calculations of the Geometry and Binding-Energy of Aromatic Dimers - Benzene, Toluene, and Toluene Benzene*. Journal of Chemical Physics, 1985. **82**(8): p. 3722-3727.

47. Law, K.S., M. Schauer, and E.R. Bernstein, *Dimers of Aromatic-Molecules - (Benzene)<sub>2</sub>, (Toluene)<sub>2</sub>, and Benzene Toluene*. Journal of Chemical Physics, 1984. **81**(11): p. 4871-4882.
48. Nishio, M., *The CH/π hydrogen bond: Implication in chemistry*. Journal of Molecular Structure, 2012. **1018**: p. 2-7.
49. Nishio, M., *The CH/π hydrogen bond in chemistry. Conformation, supramolecules, optical resolution and interactions involving carbohydrates*. Physical Chemistry Chemical Physics, 2011. **13**(31): p. 13873-13900.
50. Umezawa, Y. and M. Nishio, *CH/π hydrogen bonds as evidenced in the substrate specificity of acetylcholine esterase*. Biopolymers, 2005. **79**(5): p. 248-258.
51. Nishio, M., *CH/π hydrogen bonds in organic reactions*. Tetrahedron, 2005. **61**(29): p. 6923-6950.
52. Nakagawa, Y., et al., *Indolactam-V is involved in the CH/π interaction with pro-11 of the PKC delta C1B domain: Application for the structural optimization of the PKC delta ligand*. Journal of the American Chemical Society, 2005. **127**(16): p. 5746-5747.
53. Shi, T.J., et al., *The ionization and dissociation mechanisms of pyridine-ammonia hydrogen bonding complex*. Chemical Physics Letters, 2004. **397**(1-3): p. 160-168.
54. Perutz, M.F., *The Role of Aromatic Rings as Hydrogen-Bond Acceptors in Molecular Recognition*. Philosophical Transactions of the Royal Society a-Mathematical Physical and Engineering Sciences, 1993. **345**(1674): p. 105-112.
55. Tsuzuki, S., et al., *Origin of the attraction and directionality of the NH/π interaction: Comparison with OH/π and CH/π interactions*. Journal of the American Chemical Society, 2000. **122**(46): p. 11450-11458.
56. Tsuzuki, S., et al., *The magnitude of the CH/π interaction between benzene and some model hydrocarbons*. Journal of the American Chemical Society, 2000. **122**(15): p. 3746-3753.
57. Armstrong, K.M., R. Fairman, and R.L. Baldwin, *The (I, I+4) Phe-His Interaction Studied in an Alanine-Based Alpha-Helix*. Journal of Molecular Biology, 1993. **230**(1): p. 284-291.
58. Kryger, G., I. Silman, and J.L. Sussman, *Structure of acetylcholinesterase complexed with E2020 (Aricept (R)): implications for the design of new anti-Alzheimer drugs*. Structure with Folding & Design, 1999. **7**(3): p. 297-307.

59. Parkinson, G., et al., *Aromatic hydrogen bond in sequence-specific protein DNA recognition*. Nature Structural Biology, 1996. **3**(10): p. 837-841.
60. Liu, S.X., et al., *2nd-Sphere Electrostatic Effects in the Active-Site of Glutathione-S-Transferase - Observation of an on-Face Hydrogen-Bond between the Side-Chain of Threonine-13 and the Pi-Cloud of Tyrosine-6 and Its Influence on Catalysis*. Journal of the American Chemical Society, 1993. **115**(17): p. 7910-7911.
61. Tembreull, R., et al., *Applicability of Resonant 2-Photon Ionization in Supersonic Beam Mass-Spectrometry to Halogenated Aromatic-Hydrocarbons*. Analytical Chemistry, 1985. **57**(7): p. 1186-1192.
62. Tembreull, R., et al., *Applicability of Resonant 2 Photon Ionization in Supersonic Beams to Halogenated Aromatic-Hydrocarbons*. Abstracts of Papers of the American Chemical Society, 1985. **190**(Sep): p. 55-ANL.
63. Moe, G. and A.B.F. Duncan, *Intensity of Electronic Transitions of Methane and Carbon Tetrafluoride in the Vacuum Ultraviolet I*. Journal of the American Chemical Society, 1952. **74**(12): p. 3140-3143.
64. Kalsi, P., *Spectroscopy of Organic Compounds*. 2004: p. 11.
65. Campargue, R., *Progress in Overexpanded Supersonic Jets and Skimmed Molecular-Beams in Free-Jet Zones of Silence*. Journal of Physical Chemistry, 1984. **88**(20): p. 4466-4474.
66. Phillips, D., *Jet Spectroscopy and Molecular Dynamics*. 1995. **1**: p. 30-38.
67. Engelking, P.C., *Spectroscopy of Jet-Cooled Ions and Radicals*. Chemical Reviews, 1991. **91**(3): p. 399-414.
68. Nir, E., H.E. Hunziker, and M.S. de Vries, *Fragment-free mass spectrometric analysis with jet cooling VUV photoionisation*. Analytical Chemistry, 1999. **71**(9): p. 1674-1678.
69. Becke, A.D., *Non-Local Density Functional Theories in Quantum-Chemistry - an Overview*. Abstracts of Papers of the American Chemical Society, 1988. **195**: p. 36-Phys.
70. Yanai, T., D.P. Tew, and N.C. Handy, *A new hybrid exchange-correlation functional using the Coulomb-attenuating method (CAM-B3LYP)*. Chemical Physics Letters, 2004. **393**(1-3): p. 51-57.

71. Zhao, Y.T., D.G., *The M06 Suite of Density Functionals for Main Group Thermochemistry, Thermochemical Kinetics, Noncovalent Interactions, Excited States, and Transition Elements: Two New Functionals and Systematic Testing of Four M06-Class Functionals and 12 Other Functionals*. Theor. Chem. Acc., 2008. **120**, 215-241.
72. Runge, E. and E.K.U. Gross, *Density-Functional Theory for Time-Dependent Systems*. Physical Review Letters, 1984. **52**(12): p. 997-1000.
73. Dannenberg, J.J. and N. Kobko, *Role of counterpoise correction for BSSE in the geometry optimization of the transition states*. Abstracts of Papers of the American Chemical Society, 2000. **220**: p. U295-U295.
74. Simon, S., J. Bertran, and M. Sodupe, *Effect of counterpoise correction on the geometries and vibrational frequencies of hydrogen bonded systems*. Journal of Physical Chemistry A, 2001. **105**(17): p. 4359-4364.
75. H. B. Jansen and P. Ros, *Counterpoise Correction*. Chem. Phys. Lett. , 1969. **3**, 140.
76. Sherrill, C.D., *Counterpoise Correction and Basis Set Superposition Error*. Georgia Institute of Technology, 2010.
77. Ponti, A. and M. Mella, *Three-fragment counterpoise correction of potential energy curves for proton-transfer reactions*. Journal of Physical Chemistry A, 2003. **107**(38): p. 7589-7596.
78. Dietz, T.G., et al., *Resonance Enhanced 2-Photon Ionization Studies in a Supersonic Molecular-Beam - Bromobenzene and Iodobenzene*. Journal of Chemical Physics, 1980. **73**(10): p. 4816-4821.
79. Kadi, M. and J. Davidsson, *The photodissociation dynamics of dibromobenzenes and tribromobenzene in the gas phase studied with femtosecond pump-probe spectroscopy*. Chemical Physics Letters, 2003. **378**(1-2): p. 172-177.
80. Koplitz, B.D. and J.K. Mcvey, *Wavelength-Dependent Fragmentation in the Resonance-Enhanced Ionization of Bromobenzene*. Journal of Chemical Physics, 1984. **81**(11): p. 4963-4968.
81. Koplitz, B.D. and J.K. Mcvey, *Mechanism and Power Dependence of the Multiphoton Ionization of Bromobenzene*. Journal of Chemical Physics, 1984. **80**(6): p. 2271-2282.
82. Liu, Y.J., et al., *Photodissociation of bromobenzene, dibromobenzene, and 1,3,5-tribromobenzene*. Journal of Chemical Physics, 2004. **120**(14): p. 6502-6509.

83. Matsumoto, J., C.H. Lin, and T. Imasaka, *Enhancement of the molecular ion peak from halogenated benzenes and phenols using femtosecond laser pulses in conjunction with supersonic beam multiphoton ionization mass spectrometry*. Analytical Chemistry, 1997. **69**(22): p. 4524-4529.
84. Rademann, K., B. Brutschy, and H. Baumgartel, *Electronic Spectroscopy of Fluorobenzene Vanderwaals Molecules by Resonant 2-Photon Ionization*. Chemical Physics, 1983. **80**(1-2): p. 129-145.
85. Squire, D.W., M.P. Barbalas, and R.B. Bernstein, *Comparison of Multiphoton Ionization-Fragmentation Behavior of Benzene, Fluorobenzene, and Toluene*. Journal of Physical Chemistry, 1983. **87**(10): p. 1701-1707.
86. Wright, T.G., S.I. Panov, and T.A. Miller, *Vibrational Spectroscopy of the Chlorobenzene Cation Using Zero Kinetic-Energy Photoelectron-Spectroscopy*. Journal of Chemical Physics, 1995. **102**(12): p. 4793-4803.
87. Lu, W.Y., et al., *Two-photon ionization studies of binary aromatic van der Waals clusters: Benzene ... chlorobenzene and (chlorobenzene)(2)*. Journal of Chemical Physics, 1996. **104**(22): p. 8843-8851.
88. Muzangwa, L., et al., *On pi-stacking, C-H/pi, and halogen bonding interactions in halobenzene clusters: Resonant two-photon ionization studies of chlorobenzene*. Journal of Chemical Physics, 2012. **137**(18).
89. Adams, H., et al., *Substituent effects on aromatic interactions in the solid state*. Chemical Communications, 2001(16): p. 1500-1501.
90. Adams, H., et al., *Quantitative determination of intermolecular interactions with fluorinated aromatic rings*. Chemistry-a European Journal, 2001. **7**(16): p. 3494-3503.
91. Adams, H., et al., *A supramolecular system for quantifying aromatic stacking interactions*. Chemistry-a European Journal, 2001. **7**(22): p. 4863-4877.
92. Carver, F.J., et al., *Quantitative measurements of edge-to-face aromatic interactions by using chemical double-mutant cycles*. Chemistry-a European Journal, 2001. **7**(22): p. 4854-4862.
93. Yeh, J.H., et al., *Resonance two-photon ionization spectroscopy of the aniline dimer*. Journal of Physical Chemistry, 1996. **100**(11): p. 4385-4389.
94. Nakanaga, T., et al., *Infrared depletion spectroscopy of aniline dimer cation and aniline-benzene cation clusters*. Journal of Molecular Structure, 1997. **413**: p. 205-209.



95. Sugawara, K., et al., *Infrared depletion spectroscopy of the aniline dimer*. Journal of Physical Chemistry, 1996. **100**(43): p. 17145-17147.
96. Tang, Y., et al., *Photodissociation dynamics of bromofluorobenzenes using velocity imaging technique*. Journal of Physical Chemistry A, 2008. **112**(7): p. 1421-1429.
97. Qin, C., et al., *The REMPI spectra of o-, m- and p-bromofluorobenzene and the photodissociation of p-bromofluorobenzene*. Journal of Molecular Spectroscopy, 2012. **273**: p. 37-43.
98. Cao, Z.Z., et al., *The intersystem crossing process of p-bromofluorobenzene studied with time-resolved photoelectron imaging*. Journal of Chemical Physics, 2009. **130**(14).
99. Borg, O.A., et al., *Predissociation of chlorobenzene, beyond the pseudo-diatomic model*. Chemical Physics Letters, 2008. **456**(4-6): p. 123-126.
100. Chen, S.F., F.Y. Liu, and Y.J. Liu, *An ab initio investigation of the mechanisms of photodissociation in bromobenzene and iodobenzene*. Journal of Chemical Physics, 2009. **131**(12).
101. Liu, Y.J., P. Persson, and S. Lunell, *Theoretical study of the fast photodissociation channels of the monohalobenzenes*. Journal of Physical Chemistry A, 2004. **108**(12): p. 2339-2345.
102. Huang, C.L., et al., *Photodissociation dynamics of fluorobenzene*. Journal of the American Chemical Society, 2003. **125**(32): p. 9814-9820.
103. Frisch, M.J., *Gaussian 09*, 2009, Gaussian Inc.: Pittsburg, PA.
104. Chai, J.D. and M. Head-Gordon, *Long-range corrected double-hybrid density functionals*. Journal of Chemical Physics, 2009. **131**(17).
105. Peach, M.J.G., et al., *Assessment of a Coulomb-attenuated exchange-correlation energy functional*. Physical Chemistry Chemical Physics, 2006. **8**(5): p. 558-562.
106. Tao, J.M., et al., *Climbing the density functional ladder: Nonempirical meta-generalized gradient approximation designed for molecules and solids*. Physical Review Letters, 2003. **91**(14).
107. Mardirossian, N., J.A. Parkhill, and M. Head-Gordon, *Benchmark results for empirical post-GGA functionals: Difficult exchange problems and independent tests*. Physical Chemistry Chemical Physics, 2011. **13**(43): p. 19325-19337.

108. Diri, K. and A.I. Krylov, *Electronic States of the Benzene Dimer: A Simple Case of Complexity*. Journal of Physical Chemistry A, 2012. **116**(1): p. 653-662.
109. Amicangelo, J.C., *Theoretical study of the benzene excimer using time-dependent density functional theory*. Journal of Physical Chemistry A, 2005. **109**(40): p. 9174-9182.
110. Reid, S.A., et al., *Reactive Pathways in the Chlorobenzene-Ammonia Dimer Cation Radical: New Insights from Experiment and Theory*. Journal of Physical Chemistry A, 2013. **117**(47): p. 12429-12437.
111. Maeyama, T. and N. Mikami, *Nucleophilic-Substitution within the Photoionized Vanderwaals Complex - Generation of  $C_6H_5NH_3^+$  from  $C_6H_5Cl-NH_3$* . Journal of the American Chemical Society, 1988. **110**(21): p. 7238-7239.
112. Eggert, J., et al., *Nucleophilic-Substitution Reactions in Mixed Organic Clusters after Resonant 2-Photon Ionization*. Berichte Der Bunsen-Gesellschaft-Physical Chemistry Chemical Physics, 1990. **94**(11): p. 1282-1287.
113. Brutschy, B., *Chemical-Reactions in Mixed Molecular Clusters, Studied by Resonant 2-Photon Ionization*. Berichte Der Bunsen-Gesellschaft-Physical Chemistry Chemical Physics, 1992. **96**(9): p. 1154-1161.
114. Brutschy, B., C. Janes, and J. Eggert, *Selective Intracluster Ion-Chemistry Studied by Resonant 2-Photon Ionization Spectroscopy*. Berichte Der Bunsen-Gesellschaft-Physical Chemistry Chemical Physics, 1988. **92**(3): p. 435-437.
115. Tachikawa, H. and M. Igarashi, *Dynamics of the ionization processes of benzene- $H_2O$  clusters: A direct ab initio dynamics study*. Journal of Physical Chemistry A, 1998. **102**(45): p. 8648-8656.
116. Barnett, R.N., et al., *Oxidative damage to DNA: Counterion-assisted addition of water to ionized DNA*. Journal of the American Chemical Society, 2006. **128**(33): p. 10795-10800.
117. Miyazaki, M., et al., *Infrared spectroscopy of the benzene- $H_2O$  cluster cation: experimental study on the drastic structural change upon photoionization*. Chemical Physics Letters, 2001. **349**(5-6): p. 431-436.
118. Harada, H., et al., *Molecular cloning, tissue expression, and chromosomal assignment of a novel gene encoding a subunit of the human signal-recognition particle*. Journal of Human Genetics, 2001. **46**(2): p. 70-75.
119. Maeyama, T. and N. Mikami, *Intracluster Ion Molecule Reactions within the Photoionized Vanderwaals Complexes of  $C_6H_5F$  and  $NH_3$  and with  $H_2O$* . Journal of Physical Chemistry, 1991. **95**(19): p. 7197-7204.

120. Maeyama, T. and N. Mikami, *Nucleophilic-Substitution within the Photoionized Vanderwaals Complex C<sub>6</sub>H<sub>5</sub>Cl-NH<sub>3</sub>*. Journal of Physical Chemistry, 1990. **94**(18): p. 6973-6977.
121. Li, S.J., et al., *Supersonic Jet Studies of Benzylamines - Geometry of Their Minimum Energy Conformations*. Tetrahedron Letters, 1991. **32**(32): p. 3945-3948.
122. Fedorov, A.V., et al., *Infrared spectroscopy of H-bonded bridges stretched across the cis-amide group: II. Ammonia and mixed ammonia/water bridges*. Journal of Physical Chemistry A, 2001. **105**(35): p. 8162-8175.
123. Carney, J.R., et al., *Infrared spectroscopy of H-bonded bridges stretched across the cis-amide group: I. Water bridges*. Journal of Physical Chemistry A, 2001. **105**(14): p. 3487-3497.
124. Wu, R.H., et al., *Structure and hydrogen bonding of different isomers of 2-aminopyridine center dot NH<sub>3</sub> studied by IR/R<sub>2</sub>PI spectroscopy*. Journal of Physical Chemistry A, 2004. **108**(16): p. 3338-3343.
125. Vaupel, S., et al., *Characterization of weak NH- $\pi$  intermolecular interactions of ammonia with various substituted  $\pi$ -systems*. Journal of the American Chemical Society, 2006. **128**(16): p. 5416-5426.
126. Mizuse, K., A. Fujii, and N. Mikami, *Infrared and electronic spectroscopy of a model system for the nucleophilic substitution intermediate in the gas phase: The C-N valence bond formation in the benzene-ammonia cluster cation*. Journal of Physical Chemistry A, 2006. **110**(20): p. 6387-6390.
127. Tachikawa, H., *Intramolecular S(N)<sub>2</sub> reaction caused by photoionization of benzene chloride-NH<sub>3</sub> complex: Direct ab initio molecular dynamics study*. Journal of Physical Chemistry A, 2006. **110**(1): p. 153-159.
128. Tonge, N.M., et al., *The weak hydrogen bond in the fluorobenzene-ammonia van der Waals complex: Insights into the effects of electron withdrawing substituents on  $\pi$  versus in-plane bonding*. Journal of Chemical Physics, 2007. **126**(15).
129. McMurry, J., *Fundamentals of Organic Chemistry*. J. Organic Chemistry 2002. **5th ed.**
130. PGOPHER, [www.pgopher.chm.bris.ac.uk](http://www.pgopher.chm.bris.ac.uk) Version 7.0.103.0. 2010.
131. Reid, S.A., et al.,  *$\pi$ -Stacking, C-H/ $\pi$ , and Halogen Bonding Interactions in Bromobenzene and Mixed Bromobenzene-Benzene Clusters*. Journal of Physical Chemistry A, 2013. **117**(50): p. 13556-13563.

132. Davies, H.M.L., T. Hansen, and M.R. Churchill, *Catalytic asymmetric C-H activation of alkanes and tetrahydrofuran*. Journal of the American Chemical Society, 2000. **122**(13): p. 3063-3070.
133. Brahms, D.L.S. and W.P. Dailey, *Fluorinated carbenes*. Chemical Reviews, 1996. **96**(5): p. 1585-1632.
134. Bertrand, *Carbene Chemistry: From Fleeting Intermediates To Powerful Reagents*. 2002.
135. Mukarakate, C., et al., *Stimulated emission pumping spectroscopy of the [(X)over-tilde](1)A' state of CHF*. Journal of Physical Chemistry A, 2008. **112**(3): p. 466-471.
136. Su, M.D., *Role of spin-orbit coupling and symmetry in triplet carbenic addition chemistry*. Journal of Physical Chemistry, 1996. **100**(11): p. 4339-4349.
137. Drake, S.A., J.M. Standard, and R.W. Quandt, *An ab initio investigation of the ground and excited electronic state properties of a series of bromine- and iodine-containing singlet carbenes*. Journal of Physical Chemistry A, 2002. **106**(7): p. 1357-1364.
138. Finlayson, *Atmospheric Chemistry: Fundamentals and Experimental Techniques*. 1986.
139. Moss, *Reactive Intermediate Chemistry*. Wiley-Interscience Hoboken, NJ, 2004.
140. Bacskay, G.B., *Quantum Chemical Characterization of the (X)over-tilde((1)A'), (a)over-tilde((3)A'') and (A)over-tilde((1)A'') States of CHBr and CHI and Computed Heats of Formation for CHI and CI*. Journal of Physical Chemistry A, 2010. **114**(33): p. 8625-8630.
141. Chang, W.Z., H.J. Hsu, and B.C. Chang, *New dispersed fluorescence spectra of HCF and DCBr*. Chemical Physics Letters, 2005. **413**(1-3): p. 25-30.
142. Zdenek, *spin-orbit coupling in biradicals: heavy atom effect in carbenes*. 1998.
143. Fan, H.Y., et al., *On Renner-Teller effect and barriers to linearity and dissociation in HCF(A(1)A'')*. Journal of Physical Chemistry A, 2004. **108**(17): p. 3732-3738.
144. Fan, H.Y., et al., *Polarization quantum beat spectroscopy of HCF((A)over-tilde(1)A'')*. I. F-19 and H-1 hyperfine structure and Zeeman effect. Journal of Chemical Physics, 2004. **121**(18): p. 8869-8873.

145. Gilles, M.K., et al., *Negative-Ion Photoelectron-Spectroscopy of Hcf-, Hccl-, Hcbr-, and Hci- - Photoelectron Angular-Distributions and Neutral Triplet Excitation-Energies*. Journal of Physical Chemistry, 1992. **96**(3): p. 1130-1141.
146. Hajgato, B., et al., *Triplet-singlet energy gaps in iodo-carbenes (I-C-X): Remarkable discrepancy between theory and experiment*. Physical Chemistry Chemical Physics, 2000. **2**(22): p. 5041-5045.
147. Ionescu, E. and S.A. Reid, *A DFT study of the hyperfine coupling constants of triplet carbenes and biradicals*. Journal of Molecular Structure-Theochem, 2005. **725**(1-3): p. 45-53.
148. Ionescu, I., et al., *Polarization quantum beat spectroscopy of HCF((A)over-tilde(1)A(")). II. Renner-Teller and spin-orbit mixing in the simplest singlet carbene*. Journal of Chemical Physics, 2004. **121**(18): p. 8874-8879.
149. Karl, Singlet-Triplet Gaps in Substituted Carbenes CXY (X, Y =H, F, Cl, Br, I, SiH3). J. Am. Chem. Soc. , 1991. **114**: p. 48-51.
150. Komissarov, A., et al., Collision-induced singlet-triplet crossing and recrossing in CH2. Abstracts of Papers of the American Chemical Society, 2004. **228**: p. U272-U272.
151. Russo, N., E. Sicilia, and M. Toscano, Geometries, Singlet-Triplet Separations, Dipole-Moments, Ionization-Potentials, and Vibrational Frequencies in Methylene (CH2) and Halocarbenes (CHF, CF2, CCl2, CBr2, and Cl2). Journal of Chemical Physics, 1992. **97**(7): p. 5031-5036.
152. Tao, C., et al., *Electronic spectroscopy, lifetimes, and barrier to linearity in the, A(1)B(1) <- X(1)A(1) system of dibromocarbene*. Journal of Molecular Spectroscopy, 2007. **241**(2): p. 180-185.
153. Tao, C., et al., *High resolution probe of spin-orbit coupling and the singlet-triplet gap in chlorocarbene*. Journal of Chemical Physics, 2008. **128**(17).
154. Vargas, R., M. Galvan, and A. Vela, *Singlet-triplet gaps and spin potentials*. Journal of Physical Chemistry A, 1998. **102**(18): p. 3134-3140.
155. Wang, J., et al., *Influence of solvent on carbene intersystem crossing rates*. Journal of the American Chemical Society, 2008. **130**(20): p. 6604-6609.
156. Chang, B.C. and T.J. Sears, *High resolution near-infrared electronic spectroscopy of HCBR*. Journal of Chemical Physics, 1996. **105**(6): p. 2135-2140.

157. Deselnicu, M., et al., *Fluorescence excitation and emission spectroscopy of the  $(A)\overline{cap}(1)A'' \leftarrow (X)\overline{cap}(1)A'$  system of CHBr*. Journal of Chemical Physics, 2006. **124**(13).
158. Hall, G.E., T.J. Sears, and H.G. Yu, *Rotationally resolved spectrum of the  $(A)\overline{tilde}(060)-(X)\overline{tilde}(000)$  band of HCB*. Journal of Molecular Spectroscopy, 2006. **235**(1): p. 125-131.
159. Irikura, K.K., W.A. Goddard, and J.L. Beauchamp, *Singlet Triplet Gaps in Substituted Carbenes  $C_{xy}$  ( $X, Y = H, F, Cl, Br, I, SiH_3$ )*. Journal of the American Chemical Society, 1992. **114**(1): p. 48-51.
160. Lin, C.S., Y.E. Chen, and B.C. Chang, *New electronic spectra of the HCCl and DCCl  $(A)\overline{tilde}-(X)\overline{tilde}$  vibronic bands*. Journal of Chemical Physics, 2004. **121**(9): p. 4164-4170.
161. Mckellar, A.R.W., et al., *Spectroscopic Determination of the Singlet-Triplet Splitting in Methylene*. Bulletin Des Societes Chimiques Belges, 1983. **92**(6-7): p. 499-500.
162. Mukarakate, C., et al., *Probing spin-orbit mixing and the singlet-triplet gap in dichloromethylene via K-a-sorted emission spectra*. Physical Chemistry Chemical Physics, 2006. **8**(37): p. 4320-4326.
163. Standard, J.M., et al., *Multireference Configuration Interaction Study of Bromocarbenes*. Journal of Physical Chemistry A, 2011. **115**(7): p. 1243-1249.
164. Tao, C., et al., *Electronic spectroscopy of the  $(A)\overline{tilde}(1)A'' \leftarrow (X)\overline{tilde}1A'$  system of CDF*. Physical Chemistry Chemical Physics, 2006. **8**(6): p. 707-713.
165. Tao, C., et al., *Electronic spectroscopy of the  $(A)\overline{tilde}(1)A''(\prime) \leftrightarrow (X)\overline{tilde}(1)A'$  system of CDBr*. Journal of Chemical Physics, 2006. **125**(9).
166. Tao, C., et al., *First observation of the elusive iodocarbene: ground state multiplicity and singlet-triplet gap of CHI*. Physical Chemistry Chemical Physics, 2008. **10**(40): p. 6090-6092.
167. Tao, C., C. Ebben, and S.A. Reid, *Fluorescence Excitation and Emission Spectroscopy of the  $(X)\overline{tilde}(1)A' \rightarrow (X)\overline{tilde}(1)A''$  System of CHI and CDI*. Journal of Physical Chemistry A, 2009. **113**(47): p. 13407-13412.
168. Tao, C., C. Mukarakate, and S.A. Reid, *Fluorescence excitation and single vibronic level emission spectroscopy of the  $(A)\overline{tilde}(1)A'' \leftarrow (X)\overline{tilde}(1)A'$  system of CHCl*. Journal of Chemical Physics, 2006. **124**(22).

169. Tao, C., C. Mukarakate, and S.A. Reid, *Electronic spectroscopy of the  $A(1)A'' < \rightarrow X(1)A'$  system of CDCl*. Journal of Molecular Spectroscopy, 2007. **241**(2): p. 143-150.
170. Tao, C., et al., *High resolution study of spin-orbit mixing and the singlet-triplet gap in chlorocarbene: Stimulated emission pumping spectroscopy of CH(35)Cl and CD(35)Cl*. Journal of Chemical Physics, 2008. **129**(10).
171. Tao, C., et al., *Observation of the predissociated, quasilinear ( $B$ )over-tilde( $1)A'$  state of CHF by optical-optical double resonance*. Journal of Chemical Physics, 2007. **126**(5).
172. Tao, C., et al., *Optical-optical double resonance spectroscopy of the quasi-linear  $S_2$  state of CHF and CDF. I. Spectroscopic analysis*. Journal of Chemical Physics, 2011. **135**(10).
173. Schwartz, M. and P. Marshall, *An ab initio investigation of halocarbenes*. Journal of Physical Chemistry A, 1999. **103**(39): p. 7900-7906.
174. Kable, S.H., S.A. Reid, and T.J. Sears, *The halocarbenes: model systems for understanding the spectroscopy, dynamics and chemistry of carbenes*. International Reviews in Physical Chemistry, 2009. **28**(3): p. 435-480.
175. Lee, C.L., M.L. Liu, and B.C. Chang, *Electronic spectroscopy of bromomethylenes in a supersonic free jet expansion*. Physical Chemistry , 2003. **5**(18): p. 3859-3863.
176. Turro, *Principles of molecular photochemistry: An introduction*. 2009.
177. Turro, *Modern Molecular Photochemistry*. 1978. **Chapter 6**.
178. Yersin, H., et al., *The triplet state of organo-transition metal compounds. Triplet harvesting and singlet harvesting for efficient OLEDs*. Coordination Chemistry Reviews, 2011. **255**(21-22): p. 2622-2652.
179. Rausch, A.F., H.H.H. Homeier, and H. Yersin, *Organometallic Pt(II) and Ir(III) Triplet Emitters for OLED Applications and the Role of Spin-Orbit Coupling: A Study Based on High-Resolution Optical Spectroscopy*. Photophysics of Organometallics, 2010. **29**: p. 193-235.
180. Abegg, *An ab initio calculation of spin-orbit coupling constants for gaussian lobe and gaussian type wave functions*. Molecular physics, 1975. **30**(2): p. 579-596.
181. Fedorov, D.G. and M. Klobukowski, *Spin-orbit coupling with model core potentials*. Chemical Physics Letters, 2002. **360**(3-4): p. 223-228.

182. Fedorov, D.G. and M.S. Gordon, *Symmetry in spin-orbit coupling. Low-Lying Potential Energy Surfaces*, 2002. **828**: p. 276-297.
183. Nicklass, A., et al., *Convergence of Breit-Pauli spin-orbit matrix elements with basis set size and configuration interaction space: The halogen atoms F, Cl, and Br*. Journal of Chemical Physics, 2000. **112**(13): p. 5624-5632.
184. Berning, A., et al., *Spin-orbit matrix elements for internally contracted multireference configuration interaction wavefunctions*. Molecular Physics, 2000. **98**(21): p. 1823-1833.
185. Marian, C.M. and U. Wahlgren, *A new mean-field and ECP-based spin-orbit method. Applications to Pt and PtH*. Chemical Physics Letters, 1996. **251**(5-6): p. 357-364.
186. Hess, B.A., et al., *A mean-field spin-orbit method applicable to correlated wavefunctions*. Chemical Physics Letters, 1996. **251**(5-6): p. 365-371.
187. Trivedi, H.P. and W.G. Richards, *Abinitio Calculation of Spin-Orbit-Coupling Constant in Diatomic-Molecules*. Journal of Chemical Physics, 1980. **72**(5): p. 3438-3439.
188. Mitrushekov, A.O. and P. Palmieri, *A new configuration interaction algorithm for electron-spin-dependent properties*. Molecular Physics, 1997. **92**(3): p. 511-522.
189. Marian, C.M., et al., *Abinitio Ci Calculation of O-2+ Predissociation Phenomena Induced by a Spin Orbit Coupling Mechanism*. Molecular Physics, 1982. **46**(4): p. 779-810.
190. Carter, E.A. and W.A. Goddard, *Correlation-Consistent Singlet Triplet Gaps in Substituted Carbenes*. Journal of Chemical Physics, 1988. **88**(3): p. 1752-1763.
191. Shen, J., T. Fang, and S.H. Li, *Singlet-triplet gaps in substituted carbenes predicted from block-correlated coupled cluster method*. Science in China Series B-Chemistry, 2008. **51**(12): p. 1197-1202.
192. Xu, S.L., K.A. Beran, and M.D. Harmony, *Production of Halomethylenes in Free-Jet Expansions from a Hot Nozzle - Identification and Characterization of Hcbr and Dcbr by Laser-Induced Fluorescence Excitation Spectroscopy*. Journal of Physical Chemistry, 1994. **98**(11): p. 2742-2743.
193. Yu, H.G., et al., *Experimental and theoretical studies of the near-infrared spectrum of bromomethylene*. Journal of Chemical Physics, 2001. **115**(12): p. 5433-5444.



194. Yu, H.G., T.J. Sears, and J.T. Muckerman, *Potential energy surfaces and vibrational energy levels of DCCL and HCCL in three low-lying states*. Molecular Physics, 2006. **104**(1): p. 47-53.
195. Tarczay, G., et al., *Accurate ab initio determination of spectroscopic and thermochemical properties of mono- and dichlorocarbenes*. Physical Chemistry Chemical Physics, 2005. **7**(15): p. 2881-2893.
196. Mueller, P.H., et al., *Carbene Singlet-Triplet Gaps - Linear Correlations with Substituent -Pi- Donation*. Journal of the American Chemical Society, 1981. **103**(17): p. 5049-5052.
197. Peterson, K.A., et al., *On the spectroscopic and thermochemical properties of ClO, BrO, IO, and their anions*. Journal of Physical Chemistry A, 2006. **110**(51): p. 13877-13883.
198. F.Duschinsky, *Acta Phisicochim USSR*. Acta Phisicochim USSR 1937. **7**(551).
199. Zhang, *Theory and Application of Quantum Molecular Dynamics*. 1999.
200. Thompson, *Modern Methods for Multidimensional Dynamics Computations in Chemistry*. 1998.
201. Harvey, J.N., *Understanding the kinetics of spin-forbidden chemical reactions*. Physical Chemistry Chemical Physics, 2007. **9**(3): p. 331-343.
202. Etinski, M., *The role of Duschinsky rotation in intersystem crossing: a case study of uracil*. Journal of the Serbian Chemical Society, 2011. **76**(12): p. 1649-1660.
203. Peng, Q., et al., *Toward quantitative prediction of molecular fluorescence quantum efficiency: Role of Duschinsky rotation*. Journal of the American Chemical Society, 2007. **129**(30): p. 9333-9339.
204. Hazra, A. and M. Nooijen, *Comparison of various Franck-Condon and vibronic coupling approaches for simulating electronic spectra: The case of the lowest photoelectron band of ethylene*. Physical Chemistry Chemical Physics, 2005. **7**(8): p. 1759-1771.
205. Liebman, Am. Chem. Soc, 1979. **101**(7172).
206. Taylor, *Handbook of photochemistry*. 2006. **third edition**: p. 619.